
IN VIVO MOLECULAR IMAGING AND ASSESSMENT OF TUMOR MICRO-ENVIRONMENT BY ULTRASOUND AND PHOTOACOUSTICS

CHENG LIU

Ph.D

The Hong Kong Polytechnic University

2018

The Hong Kong Polytechnic University

Department of Biomedical Engineering

In Vivo Molecular Imaging and Assessment of Tumor Micro-environment by Ultrasound and Photoacoustics

Cheng LIU

A thesis submitted in partial fulfillment of the requirements for the degree of Doctor of Philosophy

May 2017

CERTIFICATE OF ORIGINALITY

I hereby declare that this thesis is my own work and that, to the best of my knowledge and belief, it reproduces no material previously published or written, nor material that has been accepted for the award of any other degree or diploma, except where due acknowledgement has been made in the text.

Cheng LIU

May 2017

DEDICATION

This thesis is dedicated to my family

ABSTRACT

Tumor angiogenesis and tumor microenvironment are two critical hallmarks for tumorigenesis. Tumor angiogenesis, the production of new vasculature from existing mature vessels, contributes a lot to tumorigenesis. Angiogenesis, however, is not a single step activity, but regulated by quite a number of growth factors, either as promoter or inhibitor. Endoglin (CD105), as one pro-angiogenic biomarker, has been found to be highly expressed on proliferating neo-vasculatures at the early stage of angiogenesis. However, little is known on the *in vivo* expression levels of endoglin (CD105) during the progression of glioblastoma.

Molecular ultrasound imaging, which employs functionalized microbubbles (MBs) as contrast agent, is potentially able to assess tumor angiogenesis non-invasively and quantitatively. Owing to their micron size (1~4 μm in diameter) of microbubbles, molecular ultrasound imaging is highly suitable for imaging angiogenic molecular markers on blood vessels. In this thesis, molecular ultrasound imaging with the aid of CD105-targeted microbubbles (MBs) was utilized to quantify the endoglin expression levels of glioblastoma. The results showed that CD105-targeted molecular ultrasound imaging was able to provide non-invasive and high-resolution imaging and assessment of glioblastoma angiogenesis in real time.

The understanding of protease activity requires the assessment of proteolytic activity in the tumor microenvironment rather than simply evaluation of the expression levels of proteases because the expression of any individual protease alone can not represent the proteolytic activity. It is necessary to better understand the roles and functions of a particular protease. Regarding this, we have taken protease MMP-2 as an example.

Molecular photoacoustic imaging, with the aid of properly designed contrast agent, is potential to contribute to the non-invasive imaging and assessment of protease activity i*n vivo.* This molecular imaging strategy is potential to provide not only deep penetration and high spatial resolution, but also specific patho-physiological information in molecular level in real-time. Furthermore, photoacoustic imaging (PAI) is emerging as a new powerful tool to offer unique chromophore identification information in tumor microenvironment (TME) which is unique for non-invasive imaging and assessment of the proteolytic activity *in vivo*. In this thesis, we systematically investigated the application of gold nanocage-based cleavable nanoprobe to image the proteolytic activity *in vivo*, by utilizing photoacoustic imaging technique. The potential of this strategy to image the distribution of the tumor protease activity was validated *in vitro*, in cultured cells, and in a subcutaneous xenograft tumor model *in vivo*. The results provided valuable evidences for further development of such novel molecular photoacoustic imaging strategy for investigation of tumor protease activity *in vivo*.

ACKNOWLEDGMENTS

I would like to express my sincere thanks to my chief supervisor, associate professor Dr. Lei SUN for his continuous guidance, supervision, invaluable comments. Thanks for his patience, encouragement and the effort he made on me. I will be forever grateful everything he has done.

To all the subjects who were involved in my Ph.D journey, I would like to thank them for their support to my study. Without their active participation, this study would not be accomplished.

Last but not least, I would like to give my heartfelt thanks to my dearest family for their selfless love and understanding of what I have been pursuing all these years.

TABLE OF CONTENTS

CERTIFICATE OF ORIGINALITY.....II
DEDICATION.....III
ABSTRACT.....IV
ACKNOWLEDGMENTS.....VI
TABLE OF CONTENTS.....I
INDEX OF ABBREVIATIONS.....V
CHAPTER 1 INTRODUCTION.....7
  1.1 Prevalence of cancer.....7
  1.2 Hallmarks of cancer.....8
    1.2.1 Progression of cancer hallmarks.....9
    1.2.2 Sustaining proliferative signaling.....10
    1.2.3 Evading growth suppressors.....11
    1.2.4 Resisting cell death.....11
    1.2.5 Enabling replicative immortality.....11
    1.2.6 Activating invasion and metastasis.....12
    1.2.7 Angiogenesis incidence.....13
  1.3 Endothelial cell.....14
  1.4 Tumor microenvironment.....14
CHAPTER 2 LITERATURE REVIEW.....16
  2.1 Introduction.....16
  2.2 Advantages of molecular imaging.....19
  2.3 Overview of conventional molecular imaging modalities.....20
    2.3.1 Computed tomography (CT).....22
    2.3.2 Magnetic resonance imaging (MRI).....23
    2.3.3 Positron emission tomography (PET) and single photon emission computed tomography (SPECT).....24
    2.3.4 Ultrasound (US).....25
    2.3.5 Optical imaging-fluorescence and bioluminescence.....26
    2.3.6 Photoacoustic imaging (PAI).....27
    2.3.7 Contrast agents for molecular imaging.....29

2.4 Applications of molecular imaging in oncology.. 29
CHAPTER 3 MOLECULAR ULTRASOUND IMAGING IN TUMOR NEOVASCULATURE ASSESSMENT.. 31
3.1 Research background.. 31
3.1.1 Molecular ultrasound imaging.. 32
3.1.2 Microbubble contrast agent.. 33
3.2 Research objective and hypothesis.. 34
3.3 Synthesis and characterization of targeted microbubbles.. 35
3.5 Cell-based flow chamber test of targeted microbubbles.. 37
3.6 *In vivo* animal experiment.. 39
3.6.1 Introduction.. 39
3.6.2 Subcutaneous tumor model.. 40
3.6.3 *In vivo* molecular ultrasound Imaging experiments.. 40
3.6.4 Data processing and statistical analysis.. 42
3.7 Results.. 44
3.7.1 Parallel flow chamber test of CD105-targeted MBs *in vitro*.. 44
3.7.2 *In vivo* assessment of CD105 expression levels.. 46
3.8 Discussion and conclusions.. 49
CHAPTER 4 MOLECULAR PHOTOACOUSTIC IMAGING IN TUMOR ENZYME ACTIVITY ASSESSMENT.. 52
4.1 Introduction.. 52
4.2 Dynamic proteolytic activity of MMPs.. 53
4.3 Overview of imaging strategies for MMPs activity.. 54
4.4 Abilities of molecular photoacoustic imaging.. 55
4.4.1 Label-free photoacoustic imaging.. 56
4.4.2 Gold nanocages (GNCs) as PAI contrast agent.. 58
4.5 Research gap.. 59
4.5.1 Activatable PAI contrast agent.. 60
4.5.2 Design of GNC-based activatable photoacoustic contrast agent.. 61
4.5.3 Ability of the GNC-based activatable photoacoustic contrast agent.. 62
4.6 Synthesis and characterization of activatable PAI contrast agent.. 63
4.6.1 Preparation of activatable probe.. 63
4.6.2 Dynamic light scattering (DLS) profiles of nanoparticles.. 65
4.6.3 Molar concentration of nanoparticles.. 65
4.6.4 Determination of average number of gold atoms per GNC.. 66

4.6.5 Determination of molar concentrations of GNCs........66
4.7 Determination of the molar extinction/absorption coefficient of the GNCs........67
4.7.1 The molar extinction coefficient (u_{ext})........67
4.7.2 The molar absorption coefficient (u_a)........68
4.8 Photoacoustic spectra characterization........69
4.8.1 The multispectral PAI experiment........70
4.9 Detection of protease activity in solution........71
4.10 Typical cell-based test of enzyme activity........72
4.10.1 Cell culture........72
4.10.2 Detection of protease activity in live cells........72
4.10.3 Toxicity of the GPD probe........73
4.11 Photoacoustic imaging *in vivo*........74
4.11.1 PA spectral signature characterization........74
4.11.2 Xenograft tumor models........74
4.11.3 *In vivo* photoacoustic (PA) imaging........75
4.11.4 *Ex vivo* cryosectioning and epi-fluorescence imaging........76
4.12 Results........76
4.12.1 Synthesis and characterization of probe........76
4.12.2 TEM morphology and size distribution........80
4.12.3 Photoacoustic properties........83
4.12.4 Detection of protease activity in solution........85
4.12.5 Detection of protease activity in live cells........88
4.12.6 *In vivo* PAI of protease activity........90
4.13 Discussion and conclusions........96
CHAPTER 5 CONCLUSIONS AND FUTURE WORK........99
FIGURE REFERENCES........102
REFERENCES........109

INDEX OF ABBREVIATIONS

tumor micro-environment (TME)

extracellular matrix (ECM)

single photon emission computed tomography (SPECT)

positron emission tomography (PET)

computed tomography (CT)

diffusive optical imaging (DOT)

near-infrared (NIR)

magnetic resonance imaging (MRI)

fluorescence resonance energy transfer (FRET)

bioluminescence resonance energy transfer (BRET)

ultrasound (US)

microvessel density (MVD)

vascular endothelial growth factor (VEGF)

radio-frequency (RF)

endoglin (CD105)

microbubbles (MBs)

differential targeted enhancement (dTE)

photoacoustic imaging (PAI)

immunohistochemistry (IHC)

nanoparticles (NPs)

gold nanocages (GNCs)

localized surface plasmon resonance (LSPR)

enhanced permeability and retention (EPR) dynamic light scattering (DLS)

inductively coupled plasma optical emission spectrometry (ICP-OES)

molar extinction coefficient (u_{ext})

molar absorption coefficient (u_{a})

CHAPTER 1 INTRODUCTION

1.1 Prevalence of cancer

As one of the leading cause of deaths in the world, cancer is the type of disease which is difficult to be completely cured because of its uncontrolled progression and metastasis [1]. Cancer incidence is found to be relevant to a lot of factors, such as environment, living habits. And more importantly, cancer is proven to be highly correlated with human genetic mutations, expression of hormones, and immune system, all of which may result in cancer [2]. Clinically, the management of cancer is typically constituted of surgical therapy, chemo-therapy, radiation therapy, hormone therapy, immune therapy, and targeted therapy. According to latest report from the International Agency for Research on Cancer (IARC), there were more than 14 million new incidences of cancer world-widely every year in the past five years. And the cancer-related deaths were more than 8 million per year in the past five years world-widely. The estimation of the new cases of cancer and cancer-related deaths will increase to more than 21 million and 13 million in 2030, respectively, mainly due to the population growth and aging. The most common cancer types are shown in **Figure 1.1** [1].

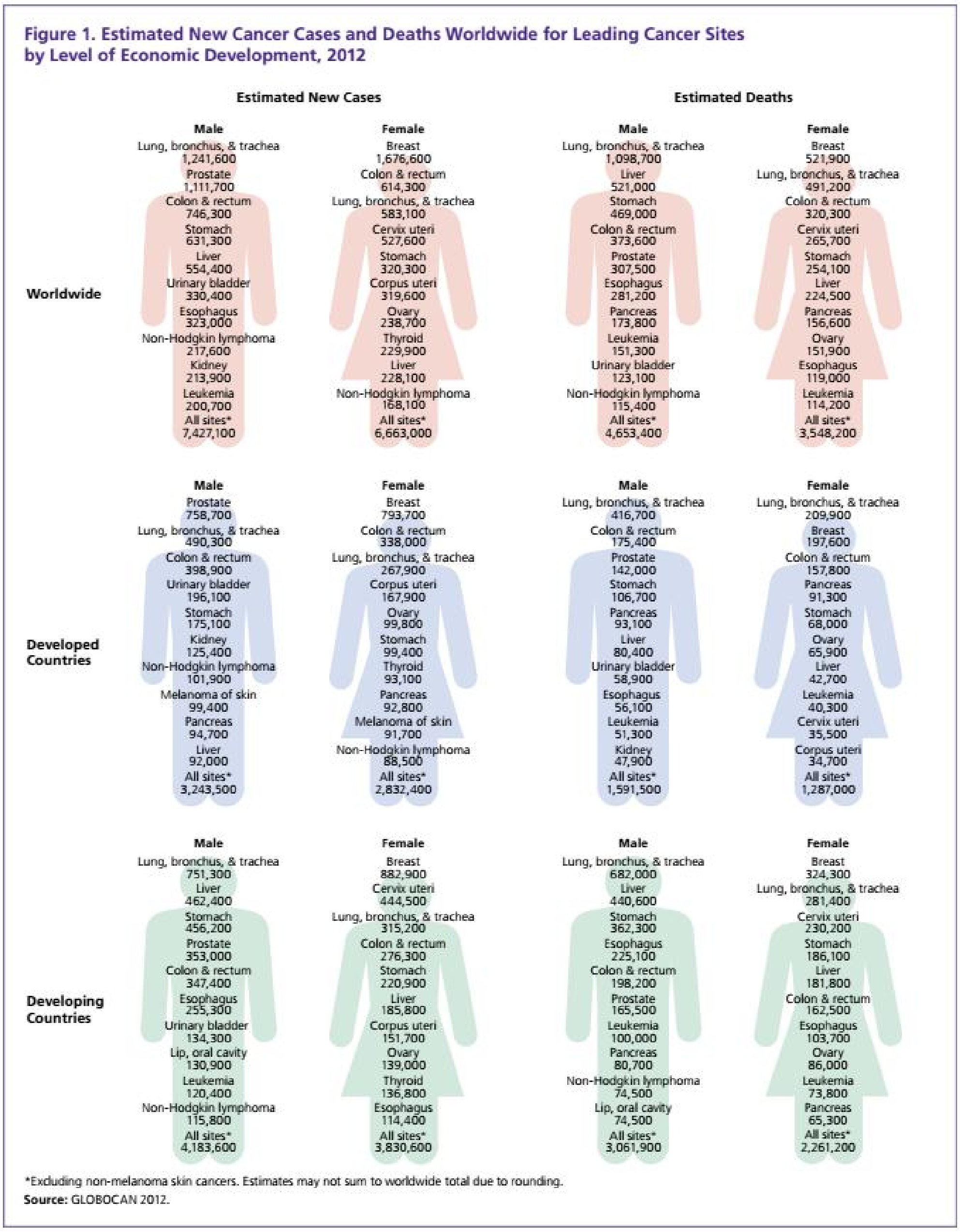

Figure 1.1. The most common cancer types in the world. (Adapted from [1])

1.2 Hallmarks of cancer

The understanding of the complexity of cancer has been proposed by pioneers in the field of cancer research, which are generally organized into six hallmarks. The six hallmarks of cancer all together have formed a comprehensive description of the characteristics of cancer [3]. Any human normal tissue cells may be possible to develop into neoplastic cells with the activation of characteristics of hallmarks of cancer. And, the tumor pathogenic progression is usually accomplished in a multi-step initialization process which allows the acquisition of the nature of malignancy.

Note-worthily, tumors cells are much more complicated than a group of highly proliferating cancerous cells. Multiple cell types including cancer cells and normal cells can contribute to the progression of cancer. Normal cells are found to form tumor-associated stroma and contribute largely to tumorigenesis; Thus, the contribution and progression of the stroma represent some hallmark characteristics of cancer. During the past decades, the understanding of cancer has developed from simply focusing on the cancer cells themselves to the surrounding healthy cells, so called ‘‘tumor microenvironment’’ [4].

1.2.1 Progression of cancer hallmarks

All the hallmarks of cancer have provided a comprehensive understanding of the nature of cancer, while every single distinct hallmark of cancer is highly associated with and complementary to the others, as shown in **Figure 1.2** [3, 5].

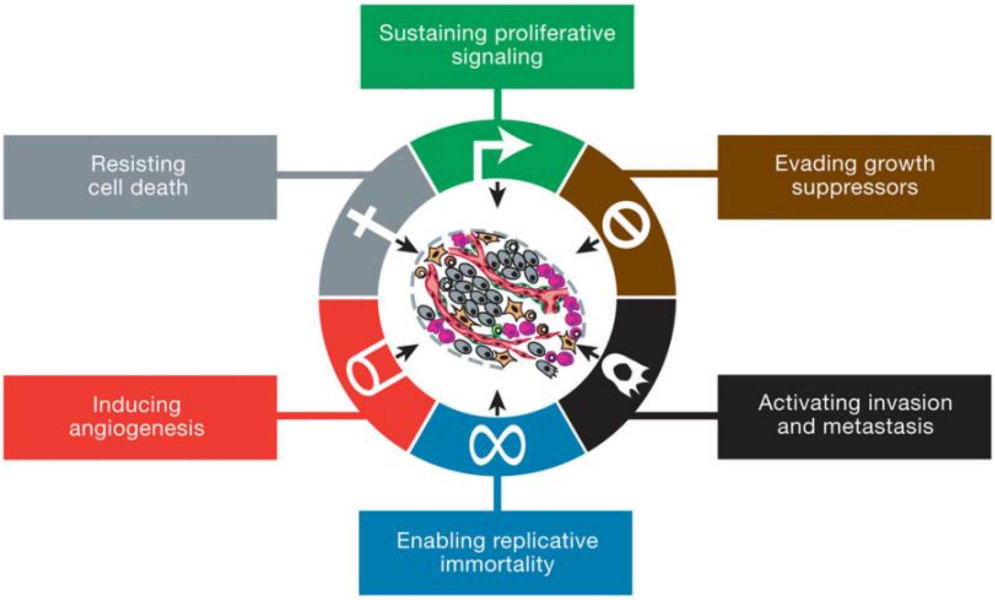

Figure 1.2. Six hallmarks of cancer [3, 5]. (Adapted from [3])

1.2.2 Sustaining proliferative signaling

Normal tissue cells are well regulated by the generation and secretion of pro-growth signals that control their progression *via* the growth cell cycle, which generates a homeostatic status in a variety of cells, structure and function of normal tissues. Unlike normal cells, cancer cells, by changing the regulations of the signals, could become uncontrolled status. The cancerous signals could result in high expression of growth factors, changes in cell cycle, increasing cell numbers and etc. The signals are also found to influence other cell-related issues, such as survival and metabolism. Those proliferative signals are complicated and yet to be fully understood [6].

1.2.3 Evading growth suppressors

In contrast to the ability to express and sustain growth-promoting signals, cancer cells also gain the ability to program negative regulation signals; it has been shown that some of the growth-suppressing signals are regulated by activities in gene level. A number of growth suppressors have been found to work in complicated ways to suppress the tumor progression and invasion in different types of cancers; In addition, underlying gene level mechanisms have also been unveiled, such as the programming for cell proliferation and apoptosis [7].

1.2.4 Resisting cell death

The programmed apoptosis could work as an inherent barrier for the progression of cancer cells, which has been a well accepted concept for cell death for decades [8]. It is valuable to understand the underlying mechanisms for signal circuitry that could trigger the apoptosis programming in different patho-physiologic conditions such as the tumorigenesis or exposure to the anti-cancer drug. In addition, it is shown that elevated pro-oncological signaling could result in a imbalanced signaling condition which is relevant to apoptosis. However, there are other evidence that induced apoptosis and enhanced resistance to therapy in highly aggressive cancer cells [8, 9].

1.2.5 Enabling replicative immortality

Previously, it was well accepted that cancer cells might need enhanced replicative ability so as to progress from cells to tumor tissues, which is an outstanding characteristic compared with most normal tissue cells. Normal tissue cells could only go through growth-and-division progress in a quite limited cycles. Such limitation is shown to be relevant to two distinct characteristics--senescence and crisis, which stand as barriers for uncontrolled proliferation. Therefore, repeated cycles of cell culture may result in initiation of senescence firstly; and followed by, going to the phase of crisis, for some cells. This procedure is so called “immortalization”, which is possessed by most established cell lines. They own the potential to go through cell culture and proliferation without going through the phases of senescence or crisis either [10].

1.2.6 Activating invasion and metastasis

Up to now, most of the mechanisms underlying the cancer invasion and metastasis are unknown. While, it is found that cancerous cells from primary tumor tissues may progress *via* vasculature and reach higher grades of malignancy, as a result, found in blood pool, nearby and distant organs [11]. The alterations of the cancer cells usually reflect both in morphology as well as interaction with normal cells and surrounding extracellular matrix (ECM) in tumor microenvironment. One of the most well-known alternations in cancerous cells is relevant to E-cadherin, which plays as a critical molecule associated with tumor cell adhesion. E-cadherin may help the formation of adherens junctions with nearby epithelial cells and keep the quiescent status of the cells. Elevated expression levels of E-cadherin are shown to act as inhibition for metastasis. On the other hand, reduced expression of E-cadherin is unveiled to increase invasion and proliferation. Down regulation and inactivation of E-cadherin in various types of human malignancies have been shown to valid its role as key suppressor of metastasis[12, 13].

1.2.7 Angiogenesis incidence

Similar to normal tissue cells, the growth of tumor cells need nutrients and oxygen, and to remove the wastes and carbon dioxide from metabolism activities. The so called “angiogenesis” process which mainly produces blood vessels could solve the problem. The production of the vasculature involves the generation of new endothelium and formation into vasculogenesis tubes and the angiogenesis sprouting of neovasculature from existing blood vessels. For normal tissues, the production of vasculature becomes quiescent after adult. Only in the cases like healing and reproduction, angiogenesis may be activated, and only for that period of time. However, for the tumor cells, the angiogenic status could last and always be “turned on”, which results in continual sprouting of neovasculatures to contribute the tumor progression [14]. The neovasculatures in malignant tumor tissues are typically heterogeneous. Some of the outstanding features in morphology and function are reported, such as distorted blood flow, enlarged vessels, excessive and aberrant vessel branching, leaky vessel wall, abnormal expression levels of pro-angiogenic biomarkers on endothelial cells [15, 16].

1.3 Endothelial cell

Typical heterogeneous features of cancer mostly exist within stromal constituents which are high associated with tumor vasculature (endothelial cells). The underlying mechanisms for endothelial cells have been well studied in the past decades. Such as the pro-angiogenic switch to form neovasculature. Besides those morphological alternations, a variety of associated signaling pathways were discovered besides the well-known signals such as VEGF. Those newly discovered signaling pathways have shown high relevance with the development of both tumor cells and vasculature [17, 18]. Besides, the alterations in gene expressions associated with the neovasculature formation and those biomarkers on endothelial cells in tumor region, normal tissue region has been another study focus in the past decade [19, 20].

1.4 Tumor microenvironment

The latest understanding of cancer biology has twisted from the tumor cells to a more comprehensive system including tumor cells, nearby environment. From the comprehensive understanding point of view, some of the complicated cancer phenotype can be better understood by taking into account the the cancerous cells and the ‘‘tumor microenvironment’ which contribute to the whole progression process [21]. The tumor microenvironment is such an emerging area that can be studied in multiple aspects considering alternations in gene level, molecular level, functional level, signaling pathway level and macroscopic morphology level. The overall picture in the tumor microenvironment may depict more underlying mechanisms of the cancer-related questions. The mentioned hallmarks of cancer have formed complementary components of most cancer types. In the future, significant discoveries by leveraging the development of new technologies may further advance our understanding of cancer biology [22].

CHAPTER 2 LITERATURE REVIEW

2.1 Introduction

Molecular imaging is playing an important role to facilitate the understanding of the complicated biochemical phenomena by non-invasive visualization of the diseases. It is designed to visualize biological-chemical-pathological processes of interest in real time non-invasively by acquisition of the information in molecular level rather than morphological and functional levels alone [23, 24]. Generally speaking, a typical molecular imaging strategy is constituted of imaging instrumentation, in combination with specialized imaging contrast agents for characterization of tissues or biomarkers, as shown in **Figure 2.1**. The contrast information derived from molecular imaging strategies may play significant roles in monitoring phenomena, detecting suspicious pathology, and more importantly, providing evidences of underlying mechanisms of disease *in vivo*. By now, the area of molecular imaging has attracted much attention of the fundamental and preclinical researchers, physicians due to its unique potentials in diagnosis, therapy and drug development. Note-worthily, there is an emerging area, so called "novel biology" by levering the novel molecular imaging tools, which focuses on understanding the underlying physio-pathological process/reaction in nanoscale *in vivo* within intact tissue/organ, such as molecule regulators and biomarkers in tumor cells and/or tumor microenvironment [25].

Retrospectively, there are strong ties between molecular imaging and nuclear medicine [26]. Since 1950s, nuclear medicine has been contributing to the non-invasive imaging strategies of human diseases by using advanced imaging instrumentation in combination with radio-nuclides contrast agent. Initially, the development of single photon emission computed tomography (SPECT) and other modalities including positron emission tomography (PET), leveraged by specialized radiolabeled probes for various biomarkers, have brought the field of nuclear imaging from conceptual phase to actual clinical translation phase [27, 28]. Since the past decades, the utilization of various targeted contrast agents into living organs for *in vivo* detecting of pathophysiological biomarkers of interests has been widely accepted rather than radioactive contrast agents alone. Different imaging modalities using different imaging contrast principles, such as diffusive optical imaging (DOT) [29], ultrasound (US) [30], magnetic resonance imaging (MRI) [31], Raman [32], photoacoustic/photothermal imaging (PAI/PTI) [33] and computed tomography (CT) [34], are increasingly emerging due to the rapid development of technology.

Unlike any classic disciplines, molecular imaging is a multidisciplinary field in nature, which cover areas, such as biology, physics, bio-chemistry, pathology, mathematics, engineering, pharmacology, chemistry, physiology, immunology, genetics, and radiology. Generally speaking, the ultimate goal of any molecular imaging strategies is to make those valuable *in vitro* assays strategies realized by *in vivo* strategies.

Although *in vitro* assays have long been recognized as benchmark for various testing due to their inevitable contributions to the detection of underlying mechanisms of different diseases, there are still some limitations [35]:

1) The analysis results from *in vitro* assays could not acquire the entire processes of interest longitudinally, which make it not suitable for depicting the comprehensive picture of patho-physiological processes;

2) The alterations in the microenvironment of the samples, such as removing cells, tissues, from the intact biological environment or preparing samples with exogenous chemicals , may make the results not representative of the actual patho-physiological scenarios;

3) The excised animal tissues would make the *in vitro* tests not suitable for longitudinal assessment of processes of interest; Further, euthanasia of animals would result in increased costs and ethic issues.

Regarding these main limitation of *in vitro* assays, the molecular imaging can provide valuable complementary tools which are suitable for visualizing and elucidating biochemical processes of interest, non-invasively and longitudinally. The bridging of conventional *in vitro* assays and molecular imaging *in vivo* together would provide complementary information for different applications in the future.

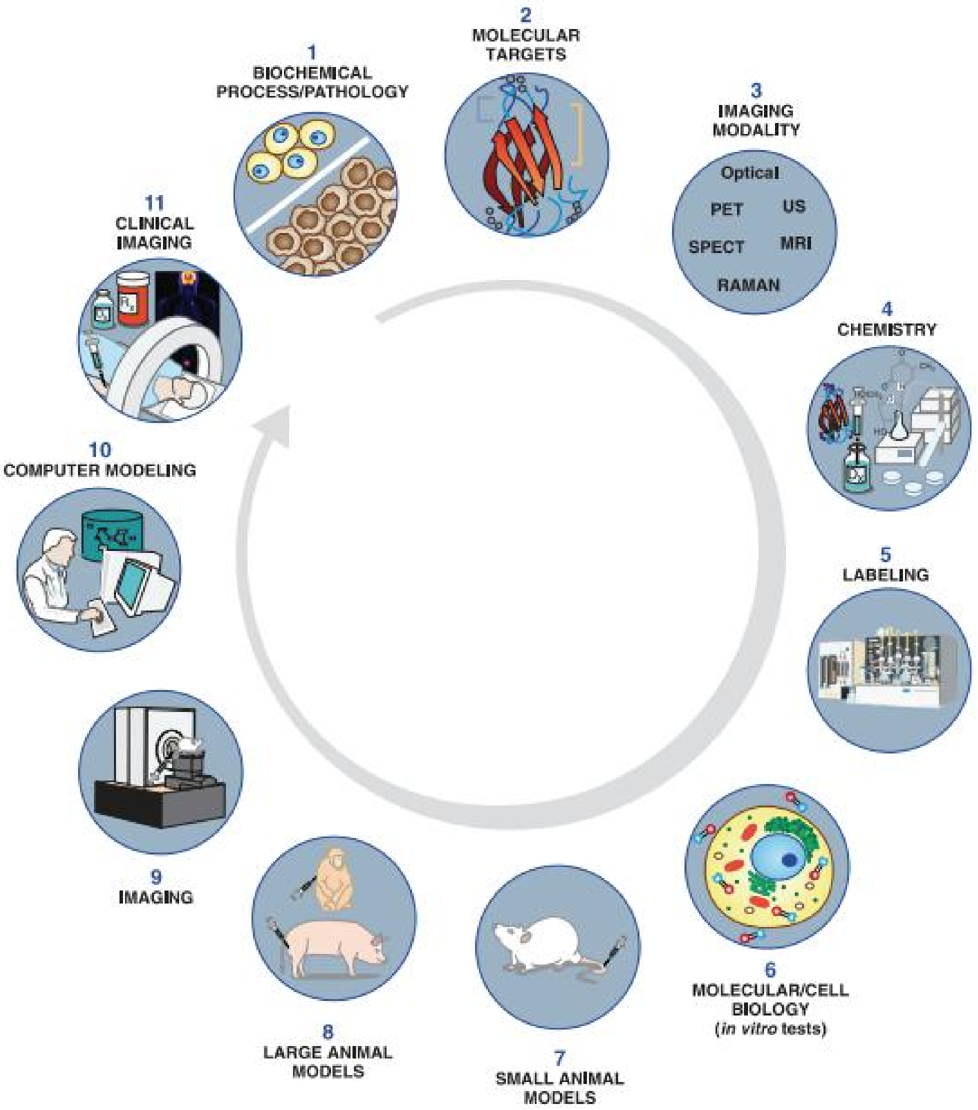

Figure 2.1. The typical development of a molecular imaging strategy. (Adapted from [26])

2.2 Advantages of molecular imaging

In contrast to conventional *in vitro* assays, the strategies of molecular imaging own some inherent advantages, including:

1) It allows non-invasive monitoring of patho-physiological process in its natural state with minimal interference to the animal's biological system. Since conventional *in vitro* assays typically require samples to be prepared outside of their native environment.

2) It allows the observation of the patho-physiological processes of interest in real time, which make the monitoring of dynamic biological processes realizable. The real-time output is of great value for both research and pre-clinical considerations.

3) It enables the record of dynamic signaling pathways in intact nature, while *in vitro* assays could only give static picture.

4) The temporal information is valuable for drug delivery research, such as kinetics and dynamics, because it help reduce the time cost that is used to assess the therapeutic effect, such as drug safety issue.

5) It is possible to conduct repeated studies in one individual animal. Therefore, it would result in reducing number of animals and individual animal could work as its own control group as the time goes on.

6) Advances in imaging modalities would provide temporally and spatially resolved contrast for studying dynamic physiological processes *in vivo*.

2.3 Overview of conventional molecular imaging modalities

Despite of the inevitable advantages, there are also some limitations for molecular imaging. Up to now, conventional *in vitro* assays and *in vivo* molecular imaging need to work together in a complementary way for solving the question better.

For any particular applications, as shown in **Figure 2.2**. There are quite a lot of issues that need to be considered, such as:

1) Spatial resolution requirement
2) Sensitivity requirement. (The lower detection limit of contrast agent utilized)
3) Temporal resolution requirement if it is a dynamic process of interest
4) Whole body imaging or organ imaging
5) Depth of penetration of the target area
6) Quantitative evaluation requirement
7) Longitudinal study requirement
8) Whether multi-modality is necessary

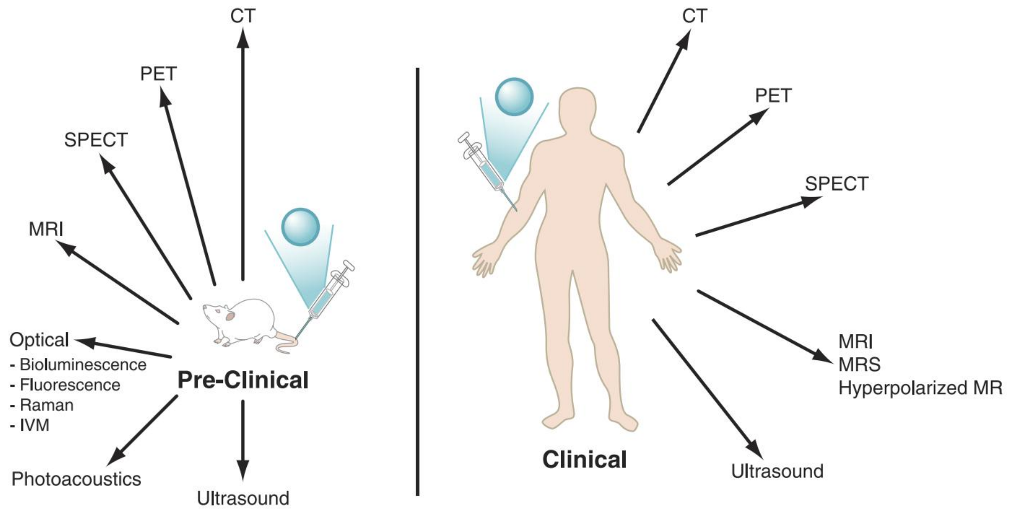

Figure 2.2. Comprehensive preclinical and clinical molecular imaging modalities. (Adapted from [26])

2.3.1 Computed tomography (CT)

Unlike conventional planar X-ray exams, Computed Tomography (CT) could provide tomographic imaging with multiple sections and thus construct in 3D anatomic volume. The advantages of CT include but not limited to fast acquisition time, high spatial resolution, economic, clinically available, deep penetration for whole-body imaging [36].

The main challenging issue for CT molecular imaging is the inadequacy in sensitivity for CT imaging contrast agents. Therefore, high dosage of imaging gent is required in order to gain adequate X-ray contrast change in region of interest. On one hand, emerging studies for CT-based molecular imaging are increasing. It was reported that iodinated nanoparticles could be applied for the MDCT visualization of macrophage infiltration in cellular level based on a rabbit atherosclerotic plaques model [37]. On the other hand, preliminary work by now has used positive targeting gold nanoparticles to enhance the imaging of cancer at cellular level and molecular level [38, 39]. Nevertheless, the achievement in the preliminary studies of CT-based molecular imaging is not perfect, and the area of CT molecular imaging is developing fast and its application potential is still worth expecting. Generally speaking, CT is quite a significant imaging tool for basic research, preclinical and clinical use. Although the potential of CT molecular imaging is not fully exploited yet, it is inevitable an valuable imaging tool. Currently, multi-modal imaging tools, which combines CT with PET, SPECT, MRI, and optical imaging, take its advantage in providing high-resolution structure imaging, while giving the bio-chem-physiological information in molecular level with other complementary modalities [40].

2.3.2 Magnetic resonance imaging (MRI)

Magnetic resonance imaging (MRI), is a rather comprehensive imaging tool that utilizes the magnet and radio-frequency (RF) signals for visualizing the morphology and/or function alternations *in vivo*, especially soft tissue [41]. The major advantages of MRI include but not limits to: 1) no ionizing radiation; 2) whole body imaging depth of penetration; 3) high spatial resolution; 4) especially good contrast for soft tissue; 5) simultaneous acquisition of physiological or metabolic data, with combined molecular level contrast information in leveraging with appropriate imaging agents [42].

The main disadvantage of MRI molecular imaging is its inadequate sensitivity. This extremely low sensitivity would result in long acquisition period of time and increased amounts of contrast agents compared with PET or SPECT (many log orders higher) [43]. This high dosage might bring about biological alterations due to pharmacological effects and toxicity issues. Regarding the dosage issue, MRI molecular imaging might be more suited for biomarkers within the vasculature because extravascular targets usually do not require high dosage of imaging agents. Generally speaking, up to date, although MRI molecular imaging does not provide adequate sensitivity, its high spatial resolution for soft tissue has made significant contribution for diagnostics and potential for fundamental research. The ability of acquiring information in molecular level from molecule biomarkers, single cells, organ/tissue may be further explored with the development of emerging probes and technologies [44].

2.3.3 Positron emission tomography (PET) and single photon emission computed tomography (SPECT)

PET and SPECT are the most-widely used molecular imaging modalities that employ radio-nuclide contrast agents with high sensitivity within intact biological system. Uniquely, PET and SPECT, both are limitless in depth of imaging penetration, thus are suitable for whole-body imaging. In most circumstances, molecular level changes happen much earlier than anatomical change in disease regions. Unlike MRI, both of them only require very low dosage of imaging contrast agents (nano to milli-gram level). In this regard, PET and SPECT are good at detecting pathophysiological alternations compared with other modalities that are good at morphology imaging, such as CT and MRI. However, the key disadvantage of PET/SPECT is the lack of structure reference information. This is why multimodal imaging tools have been developed, such as PET/CT, PET/MRI. The multimodality imaging strategy, which combines two or more imaging modalities, could compensate their inherent weaknesses and leverage their individual advantages. Another obvious disadvantage of PET and SPECT is the ionizing radiation safety issue. Recently, PET and SPECT have already been applied in clinical applications for evaluating a variety of physiological processes [45, 46].

2.3.4 Ultrasound (US)

Ultrasound imaging is a popular imaging tool that utilizes unique acoustic-tissue interface behavior of sound waves at high frequency as it passes through biological organ or tissue of interest. Ultrasound is widely used due to its uniqueness that can be used for applications both in diagnosis and therapy [47]. Conventional ultrasound, has been well accepted as an imaging modality specialized for morphological imaging. While, ultrasound contrast agents are typically microbubbles filled with gas and coated with biopolymers or lipids. The diameter of microbubbles (MBs) are in a few micrometers range. Mechanically, the microbubbles are competent in increasing the contrast-to-noise ratio, especially suitable for vasculature-related applications. The amplitude of the reflective signals from these microbubbles can be several orders higher than normal blood, mechanically due to the resonance in the ultrasound frequency range [48]. When conjugating with certain targeting moieties including antibodies or peptides and etc. on the surface of microbubbles, these microbubbles could be applied to specifically target biomarkers of interest that are highly expressed on the surface of blood vessels, and thus enabling ultrasound molecular imaging for vasculature related applications *in vivo* [49, 50].

Advantages of ultrasound include, but not limited to: economic cost, availability, portability, high temporal resolution, ionizing radiation free and high sensitivity. However, US is not competent in imaging structures containing bone or air, because ultrasound waves could not transmit bone or air. Note-worthily, microbubbles are in micrometer size which has limited its applications to image intravasculature biomarkers [51, 52]. Among all the contrast-agent-centered imaging modalities, US molecular imaging is a recently emerging one in the preclinical translation phase, whose clinical potential might be fully exploited in the next decade.

2.3.5 Optical imaging-fluorescence and bioluminescence

Since two decades ago, fluorescence microscopy has greatly contributed to all the fields related with cell. A fluorescence microscopy study, usually needs the use of fluorescent reporters, or fluorescent-labeled biomarkers, and can be applied to visualize the activities of live cells or other excised tissue samples *ex vivo* in molecular level in real time. By leveraging the strength of fluorescent microscopy, quite a number of processes of interest have been directly captured, such as cell membrane protein interactions and gene delivery in live intact cells [53, 54]. Besides fluorescent microscopy for live cell imaging, macroscopic imaging tools for small animals have also emerged. These macroscopic optical imaging modalities could provide non-invasive whole body scan of animals with imaging depth of penetration from several millimeters to centimeters range. Two widely used optical techniques for small animals are fluorescence imaging and bioluminescence imaging.

The limitations of fluorescence imaging include: inadequate imaging penetration (around 1 cm) and the safety issue of contrast agents. Note-worthily, autofluorescence from tissues inherently may ultimately reduce the sensitivity of the fluorescence imaging technique. Generally speaking, molecular fluorescence imaging is a competent technique with advantages, such as economic and good contrast to noise ratio. Besides, fluorescence optical imaging allows multiplexed imaging. Furthermore, fluorescence molecular imaging is quite suitable for imaging targets in superficial depth of penetration, such as endoscopic fluorescence imaging [55].

Unlike fluorescence imaging, bioluminescence imaging is good at higher sensitivity as a result of the amplification effect from enzymatic activation and low background noise because of a lack of natural bioluminescent chromophores. Similar to fluorescence imaging, bioluminescence imaging is also weak in depth of penetration. In contrast, bioluminescence imaging is mainly limited by acquiring light emitted from subject, however, fluorescence imaging is affected by both light illumination into and acquisition from a subject. Generally speaking, bioluminescence imaging is a low-cost tool with unique application ability in fundamental bio-chemical subject. With its flexibility in combining different luciferases/substrates, it is a quite useful tool for research [56].

2.3.6 Photoacoustic imaging (PAI)

Since first report by Alexander Graham Bell in late 19th century, the photoacoustic effect nowadays can be used for various biomedical applications [57]. Simply speaking, the photoacoustic effect is the generation of acoustic waves due to the light absorption. Currently, photoacoustic imaging (PAI) is attracting much attention to further contribute to the exploration of physio-pathological processes of interest for either healthy or diseased biological subjects *in vivo* as a non-invasive tool [58].

For most early-stage diseases, there is no endogenous photoacoustic contrast, as a result of which it limits the sensitivity and specificity of PAI as a label free imaging tool. By introducing exogenous contrast agents, the sensitivity of molecular PAI can be improved greatly because of the superior ability of contrast agents in the absorption of light and photothermal conversion efficacy. Another advantage of molecular PAI is that there are a large number of available compounds that could be used as contrast agent candidates of PAI, such as fluorescent dyes, carbon-based compounds and various metallic nanoparticles. [59]

The main advantages of molecular PAI include scalable imaging penetration from millimeter to centimeter range, which is much better than other conventional optical imaging tools [60]. In addition, the spatial resolution of PAI is not greatly decreased with the increase in imaging depth of penetration. It is unique due to leveraging the advantages of both optical and acoustic imaging. Note-worthily, the key advantages of molecular PAI include: low dosage of contrast agents (pico- to micro-grams). On the other hand, the main disadvantages of molecular photoacoustic imaging include its inadequate depth of penetration in comparison with other whole body imaging modalities. Also, similar to ultrasound, it is not suitable for imaging bone or air-related tissues. The translation of PAI to clinical application is still in the start-up phase with only a few pioneers focusing on the launch of PAI specialized for breast application. Thus, molecular PAI is such a novel molecular imaging tool regarding there are no clinical PAI applications by now. Generally, PAI alone, owns great potential in fundamental, preclinical and clinical applications; while molecular PAI, holding great potential with the aid of emerging photoacoustic contrast agents [61].

2.3.7 Contrast agents for molecular imaging

Generally speaking, contrast agents are usually constituted of targeted composite and a imaging contrast composite. The function of any contrast agent is to react and send out unique contrast signals when interacting with biomarkers of interest in a specific patho-physiological process. An ideal molecular imaging contrast agent should own the following features, such as high ratio of specific targeting of interest compared to non-specific targeting, high sensitivity for detection of interest, acceptable pharmaco-kinetic performance, stability in animal (non-specific biological activity should not affect the performance of the contrast agent much), low toxicity to animals, potential to be translated into clinical applications, low cost, contrast amplification ratio, and etc. [62]

2.4 Applications of molecular imaging in oncology

Cancer is no-doubtly a worldwide healthcare problem that affects any countries in the world, no matter developing or developed countries. Although there are tremendous efforts made to the reducing cancer every year, it is still the leading cause of mortality world-widely. It covers more than 13% of all new deaths in 2008, as recently reported from WHO. And it is estimated that the severe situation will continue in the coming years and will be tripled by the end of 2030 [1-3].

The field of cancer research has developed greatly in the past decades. Significant achievements have been made such as novel strategies for diagnosis and therapy. And the understanding of caner progression has also progressed in various levels including gene level, signaling level, functional level and morphological level

[63]. Nevertheless, there are still numerous challenging questions ahead. Clinically, cancers need to be diagnosed and confirmed by gold standard exams--biopsy and together with complementary morphological and functional imaging exams such as US, PET, SPECT, CT and MRI. In most clinical cases, the roles of imaging tools are limited to provide morphology and function information of the diseases in advanced stage or be used as a guidance for other practical operations.

Molecular imaging modalities with the aid of emerging contrast agents can be applied to cancer-related applications. The target of contrast agents could be any biomarkers of the previously introduced hallmark processes, such as angiogenesis and tumor microenvironment [64]. Previous molecular imaging studies employing contrast agents have covered various applications such as angiogenesis [65] functional hypoxia [66], cell proliferation [67], tumor apoptosis [68], tumor metabolic status [66], invasion and metastasis [69].

CHAPTER 3 MOLECULAR ULTRASOUND IMAGING IN TUMOR NEOVASCULATURE ASSESSMENT

3.1 Research background

Tumor angiogenesis, which is the productions of neovasculature from existing vessels or mature vessels, is essential to tumorous pathological processes and plays a significant role in the different progression stages of tumor [70, 71]. Typically, after reaching a certain size, tumor cells enter the exponential growth phase, during which the re-alignment and distributions of endothelial cells leads to neovasculatures and network generation around and within the tumor. The newly formed vasculature provides oxygen and nutrients to the cells for rapid growth [72].

Angiogenesis is a complicated process with multi-steps, that are associated by a series of pro-angiogenic growth factors (e.g VEGF, PDGF, Endoglin) and proteolytic enzymes (e.g., MMPs, metalloprotease domain, and plasmin) [73]. These pro-angiogenic growth factors can work as targets of molecular imaging for quantitative assessment of tumor progression. Among the pro-angiogenic growth factors, endoglin (CD105) has been shown to be remarkably up-regulated on proliferating neovasculature walls of the newly-formed blood vessels [74-76]. Pathologists have been using endoglin (CD105) as an independent target in the immunohistochemical staining test for quantitative assessment of the aggressiveness for most solid tumors [77]. It is found that endoglin is highly correlated with patients' length of survival and treatment strategy [78]. Therefore, endoglin has drawn a lot of attention as an appropriate marker for different molecular imaging modalities. Several preliminary reports have indicated the potential of endoglin as a suitable biomarker of endothelial cell proliferation in tumor diagnosis, prognosis and therapy [79-81]. However, little preliminary work was reported the expression levels of endoglin during the progression of glioblastoma non-invasively with temporal and structural information. The understanding of the temporal and spatial expression levels of endoglin *in vivo* could contribute to both new anti-cancer drug development and personalized management for glioblastoma in the future.

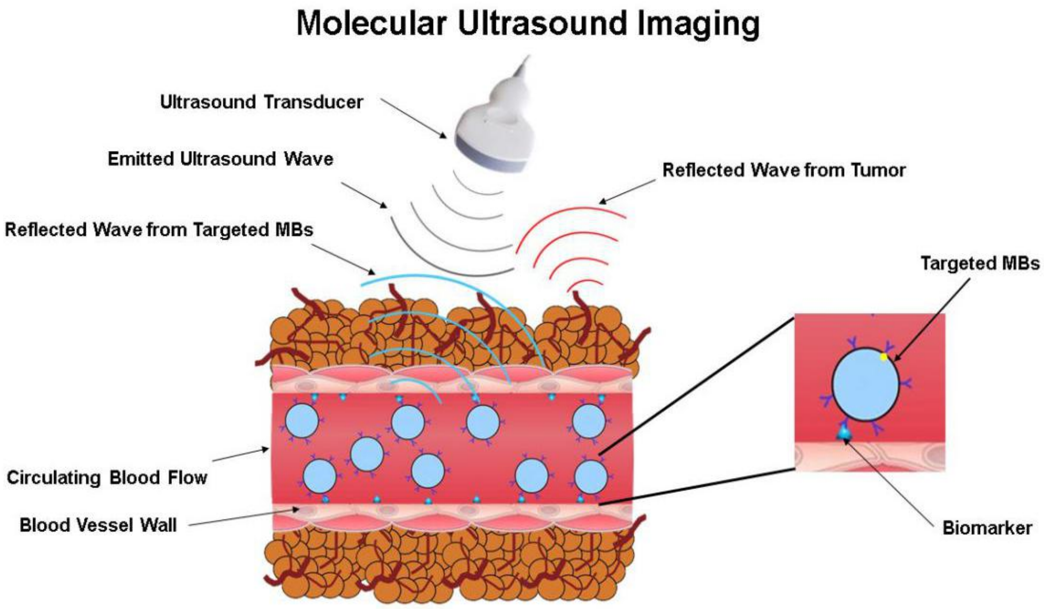

Figure 3.1. Molecular ultrasound imaging for neovasculature assessment.

3.1.1 Molecular ultrasound imaging

Molecular ultrasound imaging, which employs functionalized ultrasound contrast agent, is potentially able to assess tumor angiogenesis non-invasively and quantitatively [82]. Recently, ultrasound contrast agents are based on microbubbles

(MBs), which are liquid shell emulsions filled with gas, such as perfluorocarbon, sulfur hexafluoride and nitrogen). The shell of microbubbles are usually composed of materials which good biocompatibility, such as lipids and polymers. The structure of microbubbles (MBs) makes it unique in very high echogenic response when exposed in ultrasound mechanical waves. On one hand, this mechanical echogenic response would bring about high contrast-to-background ratio. On the other hand, the size of microbubbles usually in 1~4 μm in diameter could limit them from going to extravascular regions. Overall, molecular ultrasound imaging with the aid of MBs is quite potential for detecting biomarkers that are overexpressed on the vessel wall [83].

3.1.2 Microbubble contrast agent

Microbubbles (MBs), as ultrasound contrast agent, are usually functionalized by utilizing targeting ligands to molecular markers of interest (e.g., antibodies or peptides) [84]. The avidin-biotin binding mechanism was first developed to target monoclonal antibodies against mouse pro-angiogenic growth factor VEGF to MBs and approved to own the binding specificity in static flow condition [85, 86]. After that, a series of preclinical work has validated the use of targeted-MBs for assessment of tumor angiogenesis in animal disease model [87, 88]. It was found that microbubbles targeting to angiogenic markers could accumulate more in tumor cells than non-targeted microbubbles, which significantly increased the ultrasound signal strength [89]. Recent studies have demonstrated the ability of targeted microbubbles binding to cultured tumor cells on distinguishing tumors with different biomarker expression levels .

The efficiency of targeted MBs to the vasculature depends on multiple factors, such as the progression condition of tumor vasculature, physical pressures that push the circulating MBs to the vascular endothelium, the binding affinity of the ligand to the targets of interest and the expression levels of the target of interest on vascular endothelium [90]. Thus, one possible solution is to improve microbubbles stability by increasing the efficiency of binding [91]. Several research studies have shown improved stability using different production protocols [92-95]. Another potential consideration is to increase microbubbles circulation time in order to provide sufficient time for more microbubbles to bind to targeted biomarker, which could generate higher targeted molecular ultrasound signal and increase the sensitivity [96].

Technical advancement for higher targeted MBs efficiency and investigation of endoglin (CD105) during the glioblastoma progression is important for improving the current imaging strategies with an aim to visualize and quantify the tumor angiogenesis. Since contrast agents used for ultrasound imaging could only circulate within the vascular lumen due to their micrometer size diameter, molecular ultrasound imaging is a potential imaging strategy which is suitable for detection of the expression conditions of endoglin (CD105) on the neovasculature wall of glioblastoma.

3.2 Research objective and hypothesis

The aim of this study is to develop CD105-targeted microbubbles (MBs) and evaluate the performance of molecular ultrasound imaging for non-invasive imaging and assessment of the glioblastoma angiogenesis. We hypothesize that:

1) Microbubbles (MBs) could be functionalized to achieve specific endoglin binding efficacy and could be implemented to quantitatively assess endoglin expression levels;
2) The expression levels of endoglin change as the progression of glioblastoma;
3) The ultrasound signal intensity acquired from the CD105-targeted microbubbles correlates with the expression levels of endoglin temporarily.

We propose to use molecular ultrasound imaging and CD105-targeted microbubbles (MBs) to assess the endoglin expression levels of glioblastoma angiogenesis. As illustrated in **Figure 3.1**, CD105-targeted microbubble is consisted of a gas core that is surrounded by a lipid shell. When decorated with functional ligands, these MBs may actively bind to highly expressed endoglin in tumor angiogenesis. The ultrasound signal intensity and harmonic components from MBs are substantially higher and richer than the signal from surrounding tumor tissue. Therefore, CD105-targeted MBs that accumulate in the neo-vasculature can be identified and visualized with high sensitivity. We believe that CD105-targeted molecular ultrasound is potential to provide non-invasive and high-resolution information on glioblastoma angiogenesis.

3.3 Synthesis and characterization of targeted microbubbles

The CD105-targeted MBs and control MBs would be prepared according to a streptavidin-biotin binding protocol [97]. Perfluorocarbon-containing, lipid-shelled MBs containing streptavidin moities in the lipid shell would be reconstituted in 1 mL sterile saline (0.9% sodium chloride) according to the protocol. The mean and standard deviation of the microbubbles' diameter will be assessed by an optical particle counter with a 0.5 mm diameter detection limit (Accusizer 780; Particle Sizing Systems, Santa Barbara, CA, USA). Two types of targeted MBs would be produced by using streptavidin-biotin binding chemistry: (a) CD105-targeted MBs, targeting to mouse endoglin, (b) control non-targeted MBs, targeting with an isotype-matched control immunoglobulin G antibody. For targeting the respective MBs, 5 µg of the following antibodies would be incubated with 5×10^7 MBs for 10 minutes at room temperature: (a) biotinylated rabbit anti-mouse endoglin monoclonal antibodies, (b) biotinylated rabbit control immunoglobulin G antibodies.

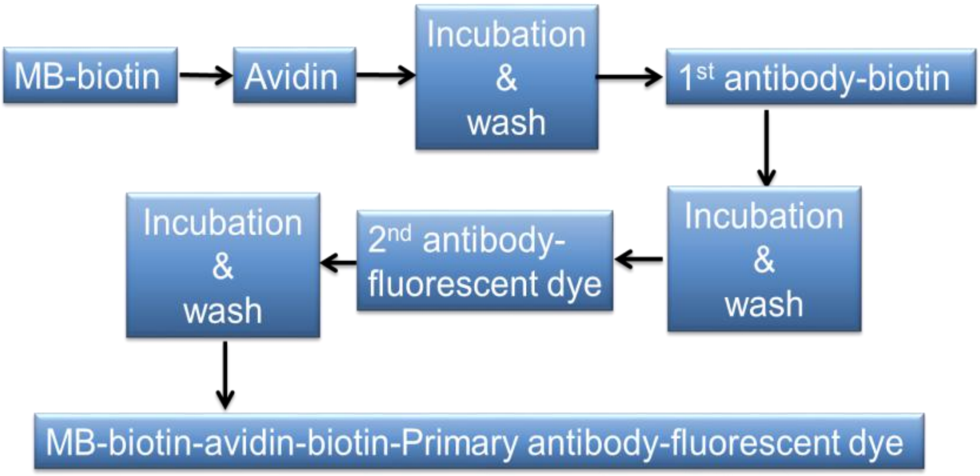

Figure 3.2. Two types of MBs were prepared: 1) CD105-targeted MBs as MBs-biotin-avadin-biotin-anti-CD105-FITC; 2) control non-targeted MBs as MBs-biotin-avadin-biotin-IgG. The 2nd antibody-fluorescent dye (FITC) was used to confirm the affinity of the primary antibody on the shell of MBs. Immunoglobulin G antibodies (IgG) was used as the control antibodies for non-targeted MBs.

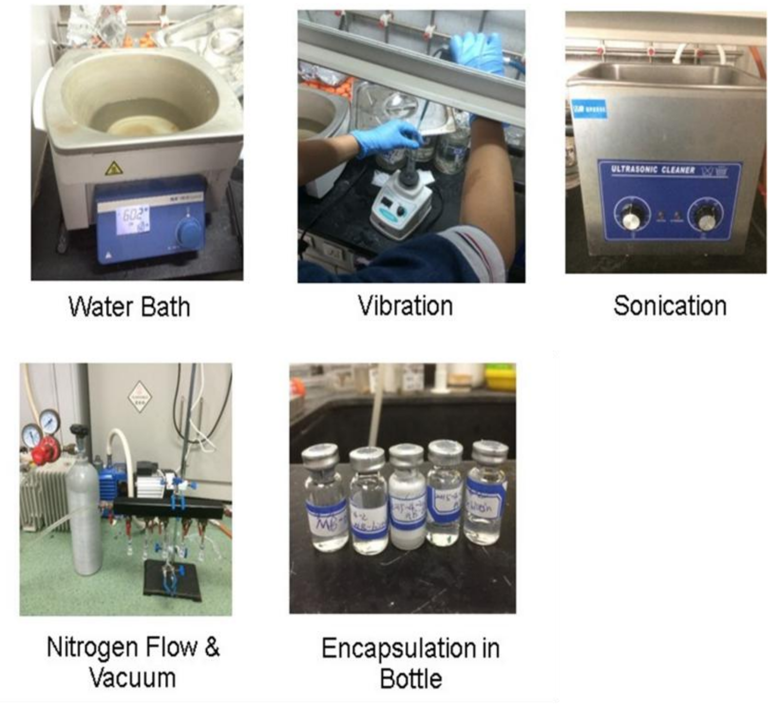

Water Bath

Vibration

Sonication

Nitrogen Flow & Vacuum

Encapsulation in Bottle

Figure 3.3. Procedures of preparation of non-targeted MBs.

3.5 Cell-based flow chamber test of targeted microbubbles

To assess the binding specificity of the CD105-targeted MBs to the biomarker CD105, parallel flow chamber test was performed, according to a reported protocol [49].

Two types of cell lines, mouse endothelial cell line MS1 and mouse breast cancer cell line 4TI were selected as the CD105 high and low expression cell lines, respectively. Both MS1 and 4T1 cell lines were purchased from the National Infrastructure of Cell Line Resource (Chinese Academy of Science, Shanghai, China). For MS1 cells, the culture medium was ATCC-formulated Dulbecco's modified Eagle Medium (ATCC) with 5% fetal bovine serum and 1% penicillin-streptomycin. For 4T1 cells, they were cultured in ATCC-formulated RPMI-1640 medium with 10%

fetal bovine serum and 1% penicillin-streptomycin. Both cell lines were cultured in sterilized environment with 5% CO_2 humidified condition and 37°C air atmosphere.

Two million MS1 cells and two million 4T1 cells were coated on different cell culture dishes, respectively. The dishes would then be tested on a parallel flow chamber, as shown in **Figure 3.4**. The solutions would be passed over the two types of cells in parallel flow chamber in the following order: (a) phosphate-buffered saline (PBS), (b) 5×10^7 of CD105-targeted MBs and control MBs in PBS, and (c) a final rinse with PBS. The cell culture dishes would then be wet-mounted with a coverslip for immediate imaging with a bright-field microscope. Triplicate runs were performed for each cell line and MBs type, and six randomly selected optical fields of view per slide would be used for subsequent quantification of the number of bound MBs per cell. In order to further confirm the binding specificity of CD105-targeted MBs, another two groups of cells (e.g., MS1 and 4T1) were incubated with anti-mouse CD105 monoclonal antibodies to block the CD105 receptor in prior, and followed by the parallel flow chamber test. All blocking experiments were performed in triplicate.

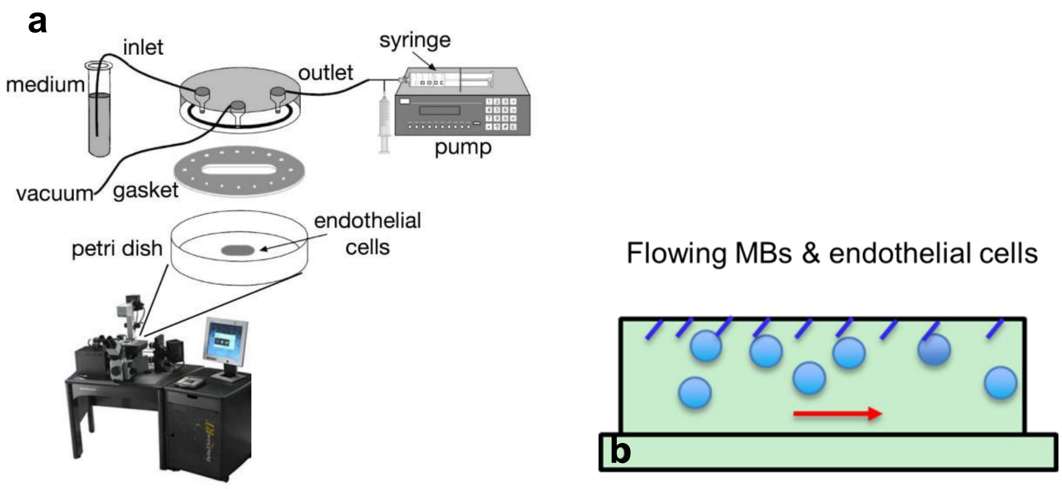

Figure 3.4. (a) Parallel flow chamber test set up; (b) flowing MBs targeting to endothelial cells. The cells were coated on the bottom of petri dish, while the MBs would flow through the chamber as the red arrow shows. Two types of cell lines (MS1, 4T1) were used as positive an negative CD105 expressing cell lines. CD105-targeted MBs and non-targeted MBs would be used to test the attachment specificity to the positive and negative cell lines in the absence and presence of blocking antibodies.

3.6 *In vivo* animal experiment

3.6.1 Introduction

All procedures using laboratory animals were approved by the Department of Health, The Government of the Hong Kong Special Administrative Region and the Hong Kong Polytechnic University Animal Subjects Ethics Sub-committee. Tumors were established by subcutaneous injection of human glioblastoma cells suspension into the right hind limb of 6–8 week-old female nude mice. A total of 9 pieces of tumors were produced and used in this study. Tumor volumes of each mouse were measured and recorded daily with B-mode ultrasound imaging. And then according to the tumor volume, the mice were divided into 3 groups: 50-150 mm^3 as small group, 151-250mm^3 as medium group, larger than 250 mm^3 as large group. All tumors were scanned using Vevo2100 high-frequency ultrasound system (FUJIFILM VisualSonics, Toronto, Canada) with an LZ-250 linear array transducer (center frequency 21 MHz, 256 elements, lateral and axial resolution of 165 and ~75 µm, respectively, maximum imaging depth of 20 mm).

3.6.2 Subcutaneous tumor model

The Hong Kong department of health endorsed all procedures using female nude mice in our experiment. All the 6-8 weeks old female nude mice were purchased from CUHK. Tumors are implanted in the subcutaneous right hind limb of 6-8 weeks old female nude mice by injecting 5×10^6 U-87 MG cells. Before injection, every 5×10^6 cells should be mixed with 50 μL matrigel (BD Biosciences, San Jose, Calif). To value the tumor volumes, B-mode US were used daily (volume=pie/6 × length × $(\text{width})^2$). And then according to the tumor volume, the mice were divided into 3 groups: 50-150 mm^3 as small group, 151-250 mm^3 as medium group, larger than 250 mm^3 as large group.

3.6.3 *In vivo* molecular ultrasound Imaging experiments

All mice would be kept under anesthesia with 2% isoflurane in room air during experiment, and all experiment settings would be kept the same. Molecular ultrasound imaging scan was performed in the fundamental B-mode ultrasound imaging using Vevo2100 high-frequency ultrasound system (FUJIFILM VisualSonics, Toronto, Canada) with an LZ-250 linear array transducer. The central planes of those tumors would be aligned by the guidance of the B-mode ultrasound imaging. In all mice, data acquisitions were performed by injecting two types of MBs in the following order: 1) control MBs and 2) CD105-targeted MBs, into the same animal during the same imaging session with a interval time of 40 mins, as shown in **Figure 3.5**. All mice were injected *via* the tail vein in random order with non-targeted control MBs first and CD105-targeted MBs after an interval time of 40 mins. After injection of the MBs, an ultrasound imaging sequence using an ultrasound burst and replenish technique would be performed: 3 mins after the MBs injection, both B-mode ultrasound imaging and non-linear contrast ultrasound imaging frames would be acquired and overlaid over a 10 seconds period. This would be followed by a destruction burst (10 MHz; mechanical index, approximately 0.235) for about 6 seconds to destroy all MBs in the region of interest. After the burst, 250 frames would be acquired again to capture the replenishment procedure of the floating-in MBs, as shown in **Figure 3.6**. Regions of interest capturing the entire tumors would be drawn by one experienced reader. The imaging signal from CD105-targeted MBs would be calculated by averaging pre-destruction and post-destruction imaging signals and subtracting the post-destruction signal average from the pre-destruction signal average. The resulting video intensity would be considered to represent MBs attached to the endothelial biomarker CD105. Images representing the attached MBs would be displayed as an overlay on the B-mode ultrasound anatomic images. Thereafter, the molecular ultrasound imaging results would be correlated with the result of *ex vivo* immunohistochemistry analysis (e.g., CD31 and CD105).

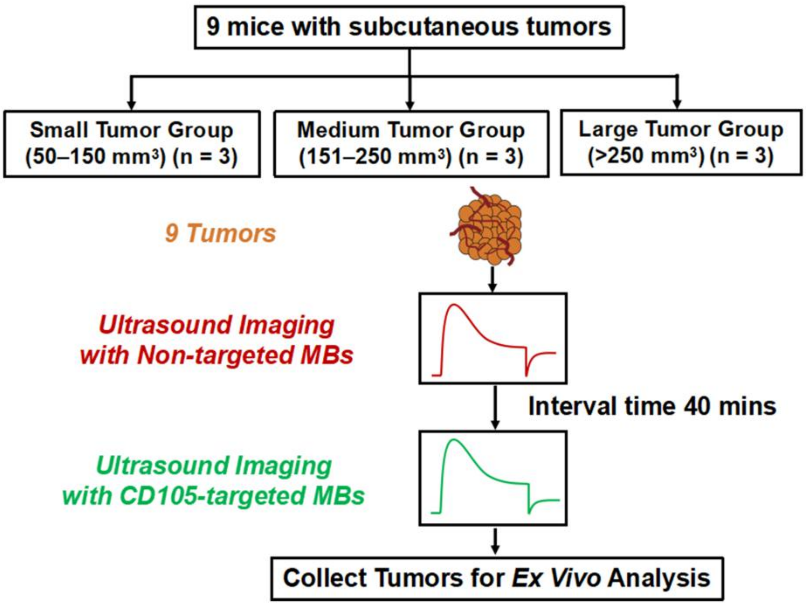

Figure 3.5. Experiment design of *in vivo* experiment. Subcutaneous glioblastoma tumor xenograft was established for assessment of CD105 expression levels by molecular ultrasound imaging. Non-targeted MBs were injected and measured as the control, and CD105-targeted MBs were injected with 40 mins interval after the injection of non-targeted MBs. The imaging signal from CD105-targeted MBs would be calculated by averaging pre-destruction and post-destruction imaging signals and subtracting the post-destruction signal average from the pre-destruction signal average.

3.6.4 Data processing and statistical analysis

The date would be analyzed and output as means ± standard deviations. For the parallel flow chamber test, a paired Wilcoxon test would be applied to compared the attachment number of CD105-targeted MBs with control non-targeted MBs, which passed over the two cell lines (MS1 and 4T1). The different attachment numbers before and after the blocking with antibody would be assessed with a paired Wilcoxon test. Also, a spearman rank correlation (ρ values) would be used to test the correlation between the CD105 expression levels of the two types of cell lines assessed by flow cytometry and the attachment numbers of MBs in the parallel flow chamber test. Spearman rank correlation would be applied to correlate the *in vivo* CD105-targeted ultrasound signal results with *ex vivo* immunofluorescence results in three tumor size groups. $P < .05$ would be considered to be a statistically significantly difference.

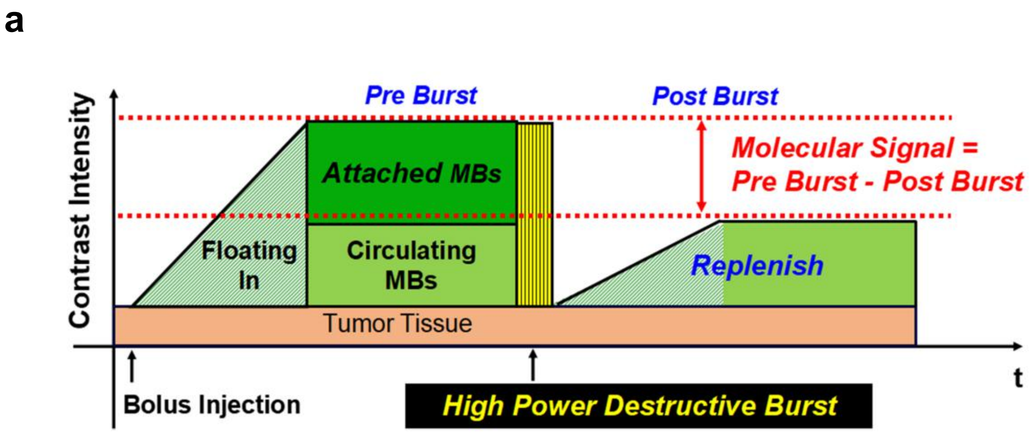

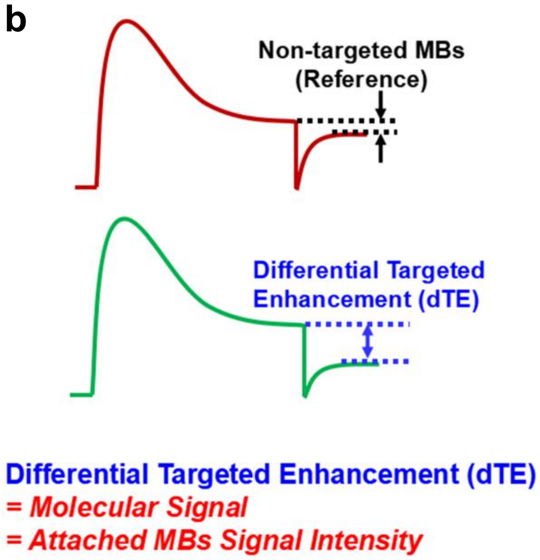

Figure 3.6. Principal of quantitative assessment of molecular ultrasound signals. (a) Burst and replenishment technique for quantitative assessment of the attached MBs on vessel wall. (b) Differential Targeted Enhancement (dTE) would be used to indicate the molecular signal which is contributed by attached MBs. Non-targeted MBs were used as a reference for CD105-targeted MBs.

3.7 Results

3.7.1 Parallel flow chamber test of CD105-targeted MBs *in vitro*

The morphology and size distribution of CD105-targeted MBs are shown in **Figure 3.7**. The fluorescence microscope imaging confirmed that the anti-mouse CD105 monoclonal antibodies were successfully bond to the shell of the MBs.

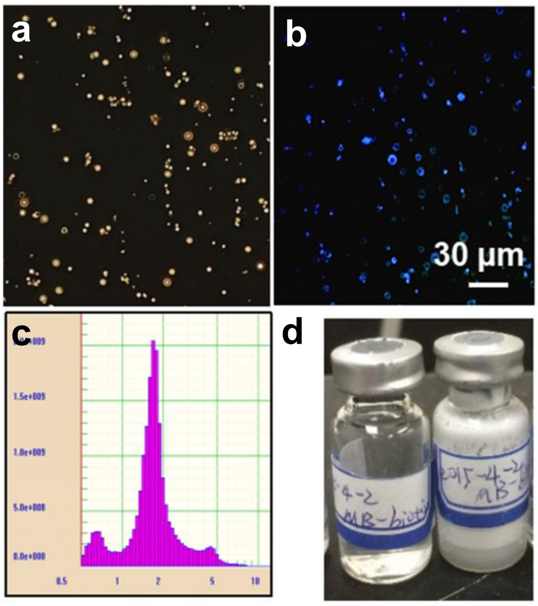

Figure 3.7. *In vitro* characterization of CD105-targeted MBs (MBs-biotin-avadin-biotin-anti-CD105-FITC). (a) dark field microscope image; (b) fluorescence

microscope imaging; (c) size distribution of MBs, mean diameter in 2-3 μm; (d) photograph of prepared MBs kept in vials.

Attachment numbers of CD105-targeted microbubbles were significantly (*P* = .005) higher to MS1 cells (CD105 +) than to 4T1 cells (CD105 -), as shown in **Figure 3.8**. And, the attachment numbers of non-targeted MBs to MS1 cells was significantly (*P* = .025) lower in comparison with CD105-targeted microbubbles, as shown in **Figure 3.8**. Furthermore, MS1 cells with blocking treatment showed a significant (*P* = .015) decrease in the attachment numbers of CD105-targeted MBs, as shown in **Figure 3.8**, which could confirm the attachment specificity of the CD105-targeted MBs to the specific biomarker in the parallel flow chamber tests. Further, the analysis between the attachment numbers of CD105-targeted microbubbles and *in vitro* expression levels of CD105 on cells (e.g., MS1 and 4T1) as assessed by flow cytometry test showed a significant positive correlation ($\rho = 0.76$, $P < .032$).

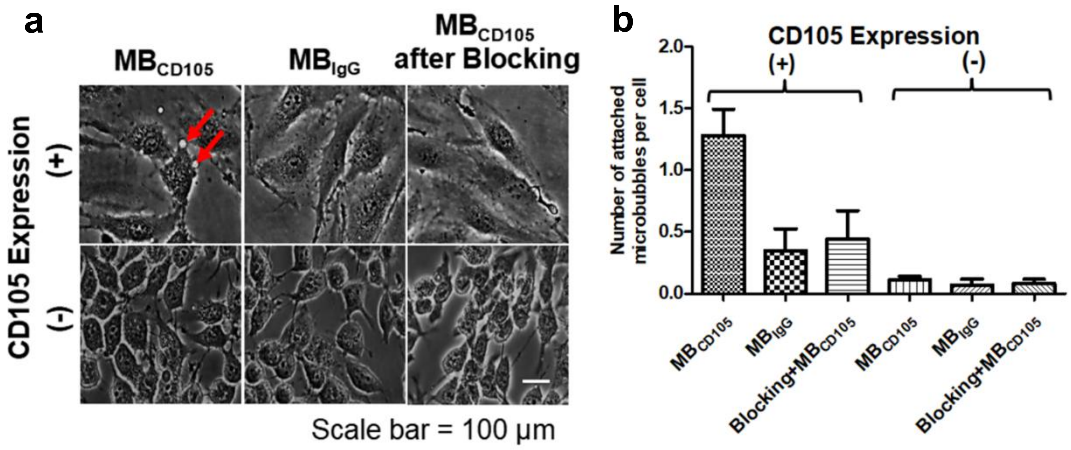

Figure 3.8. Parallel flow chamber test results. (a) Dark field microscope images of parallel flow chamber test. Two types of cell lines were used: endothelial cell MS1

with CD105 positive expression, and 4T1 cells with CD105 negative expression. CD105-targeted MBs and non-targeted MBs were used as control, while anti-CD105 monoclonal antibody was used as blocking control in CD105 positive expressing cells. Red arrow indicates the location of attached MBs. The round small spots under bright-field microscopy were MBs that were in contact with the membrane of cells without free floating movement. (b) Quantitative attachment results of parallel flow chamber test. Attachment number of MBs per cell. Attachment number of controlled MBs to MS1 cells (CD105 +) was significantly (*P* = .025) lower in comparison with CD105-targeted microbubbles; MS1 cells (CD105 positive) with blocking treatment showed significant (*P* = .015) decrease in the attachment numbers of CD105-targeted MBs, which could confirm the attachment specificity of the CD105-targeted MBs to the specific biomarker in the parallel flow chamber tests.

3.7.2 *In vivo* assessment of CD105 expression levels

The results showed positive correlation between the *in vivo* molecular US signal and *ex vivo* expression levels of CD105 as assessed with immunofluorescence test ($\rho = 0.86$, $P < .001$), as shown in **Figure 3.11**. Additionally, the immunofluorescence test confirmed that the expressions of both CD105 and CD31 were colocalized on the endothelial cells, as shown in **Figure 3.11**, which demonstrated that the *in vivo* molecular US signal specifically came from those attached CD105-targetd MBs to the pro-angiogenic biomarker CD105 which was expressed on the endothelial cells in the tumor tissue. In glioblastoma subcutaneous xenograft model, the expression levels of endoglin (CD105) in small and medium size tumors were significantly higher (*P*

< .032) in comparison with CD31. In large size tumors, expression level of endoglin (CD105) was significantly lower (*P* < .023) than CD31, as shown in **Figure 3.11**.

- *In vivo* experiment set up: MBs injection via tail vein for multiple imaging at different time
- B/W contrast: ultrasound image
- Green contrast: non-linear ultrasound image

Figure 3.9 *In vivo* molecular ultrasound animal tumor model experiment set-up

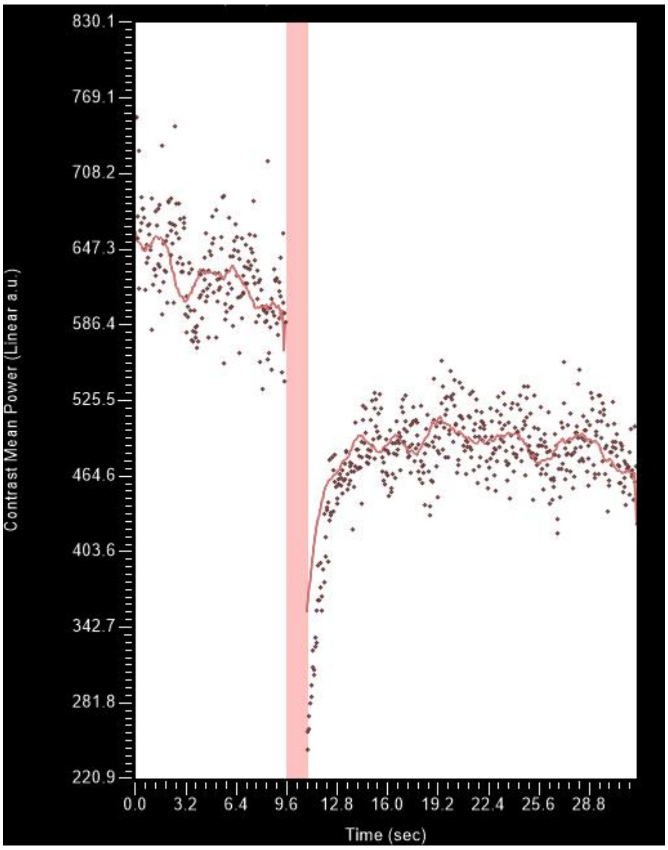

Figure 3.10 Destruction and replenishment curve of injected MBs in tumor area in subcutaneous tumor model. After the high energy burst, the MBs were destroyed and

quickly replenished to the tumor area via the vasculature. The gap between the curve before and after the burst could represent the contribution from targeted MBs on the endothelial wall of blood vessels which was due to the binding to CD105

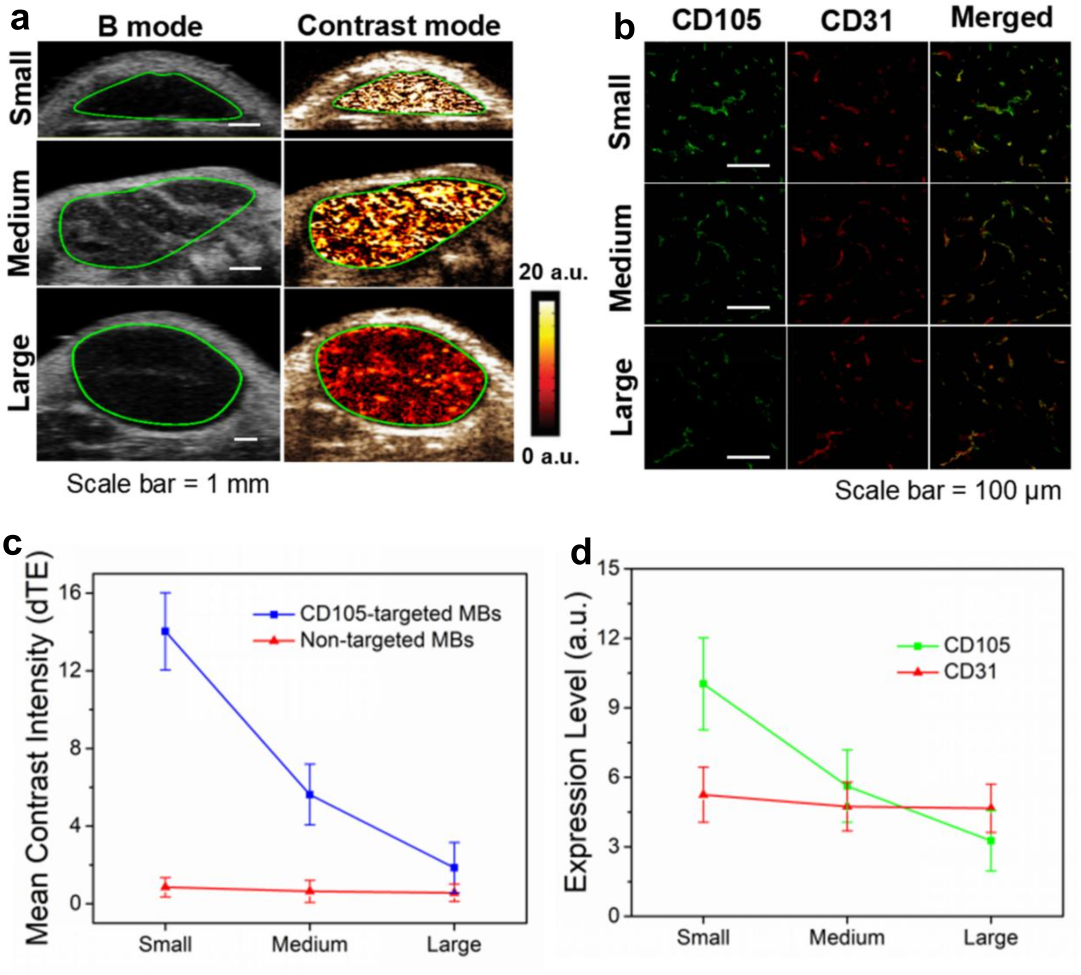

Figure 3.11. *In vivo* assessment of CD105 expression levels in subcutaneous glioblastoma tumor xenograft in small, medium and large size. (a) Dual-mode imaging (B mode & contrast mode) of tumors with CD105-targeted MBs, scale bar = 1 mm; (b) *ex vivo* immunohistochemistry (IHC) test (CD105 and CD31) of tumor tissues. CD105 was confirmed to be expressed on endothelial cells. (c) Differential Targeted Enhancement (dTE) measured in small, medium and large glioblastoma tumor groups by using CD105-targeted MB and non-targeted MBs. (d) quantification

of the expression levels of CD105 & CD31 in tumor tissues by *ex vivo* immunohistochemistry (IHC) in small, medium and large glioblastoma tumor groups. Statistical results indicated that the expression levels of endoglin (CD105) in small and medium size tumors were significantly higher ($P < .032$) in comparison with CD31. And, in large size tumors, expression level of endoglin (CD105) was significantly lower ($P < .023$) than CD31.

3.8 Discussion and conclusions

In this study, the expression level of CD105, which is a unique biomarker representing the neovasculature's growth, was evaluated by molecular ultrasound imaging *in vivo.* The *in vivo* image contrast from the targeted MBs has shown that the expression level of CD105 decreased when the tumor progressed to larger size which was correlated with the histology result (co-staining CD105/CD31) *ex vivo.* The *in vitro* binding test showed that the targeted MBs could target to specific biomarker (CD105) on the positive cell surface. In this study, two types of cell lines (MS1 and 4T1) were selected as the CD105 ± expression cells for the assessment of the expression levels of CD105 in parallel flow chamber condition. The flow chamber *in vitro* test was used as a mimic situation for the *in vivo* blood flow environment, which could be used to test the binding affinity of the targeted MB *in vitro.* The flow chamber test showed that the binding affinity and specificity were adequate for *in vivo* applications. And, the binding efficiency of avadin-biotin conjugate was tested using the FITC fluorescence dye under the visualization of fluorescence microscope. Overall, the molecular ultrasound imaging as a preclinical research tool, was used to evaluate the expression levels of neovasculature-related endoglin (CD105) *in vivo* on animal glioblastoma subcutaneous xenograft model. The statistical results *in vivo* with the *in vitro* binding test together have validated this strategy as a non-invasive method to monitor the progression of neovasculature of glioblastoma *in vivo*.

The assessment of tumor angiogenesis is one popular application of molecular ultrasound imaging. Among all the pro-angiogenic growth factors, vascular endothelial growth factor (VEGF) is the best studied factor and has gained much expectation for clinical translation. Besides VEGF, endoglin (CD105) acts as an alternative pro-angiogenic growth factor. In clinic, endoglin (CD105) based immunohistochemistry test is accepted as a standard test to assess the tumor angiogenesis by quantifying the microvessel density (MVD) for many types of solid tumors [51, 52]. It has been approved that endoglin (CD105) could be selectively expressed on highly proliferating endothelial cells rather than the normal and mature endothelial cells. However, the studies of molecular imaging that are relevant to the alternative pro-angiogenic growth factor endoglin (CD105) are still in the developing phase according to the literature [74].

The non-invasive molecuar imaging and assessment of endoglin (CD105) is potential to act as an alternative strategy for monitoring tumor angiogenesis. Therefore, the motivation of this work was to develop and assess the CD105-targeted molecular ultrasound imaging strategy for glioblastoma neovasculature. The CD105-targeted ultrasound contrast agent (microbubbles) was investigated in solution, *in vitro* parallel flow chamber, and *in vivo* tumor model. Note-worthily, the micrometer size microbubbles would be limited within blood lumen, which are quite suitable for applications to intravasculature biomarker. Those MBs in micrometer size could only circulate in the blood stream for a few minutes. Compared with other types of contrast agents, the clearance process of MBs is quite unique. The gas could be cleared out from the human body through gas exchange by expiration in lung. It was demonstrated in clinic that it only took 6 minutes to clear out 99.9% of C_3F_8 from patients by utilizing one commercial available type of MBs by post intravascular (I.V) injection. [99] Those MBs residues (e.g., MBs shell compound and few MBs) could be cleared out by phagocytosis process. MBs have been recognized as one safe contrast agent for US imaging [100-102].

Targeted microbubbles, when decorated with functional ligands, may actively bind to highly expressed endoglin (CD105) in tumor neovasculature. Because the ultrasound signal intensity and harmonic components from microbubbles are substantially higher and richer than the signals from surrounding tissue, the targeted MBs that are accumulated in the neo-vasculature can be identified and visualized with molecular ultrasound imaging with high sensitivity.

The targeted-MBs circulate and target to biomarkers within the vasculature relying on the blood flow. In real situations, the concentrations of MBs in the bulk blood flow are much higher than the immediate vessel wall proximity. In other words, most of the MBs would pass through the bulk flow without contact with the target vessel wall. However, the targeted-MBs could only target to molecular biomarkers on vessel wall *via* direct contact and interaction. Therefore, most of the targeted-MBs that do not have direct interact with the target vessel wall would not reach the binding target at all. This situation would cause reduced retention time of MBs within vasculature and increase the cost of MBs. To solve the problem, one possible solution is to increase the dose of MBs to increase the contact chance of MBs with the target vessel wall, while it would also increase the cost of MBs and potential side-effect to patients. Another possible solution is the expose the MBs in an acoustic field so that the MBs could be concentrated at the desired vessel wall by acoustic radiation force. This radiation force method is potential to improve the targeting efficiency at the region of interest and also reduce the potential cost of MBs [103]. In the future, the molecular ultrasound imaging with targeted-MBs is potential to be translated to a variety of applications. Those applications could be realized *via* targeting to the relevant biomarkers on blood vessels by utilizing targeted-MBs. Potential applications include tumor angiogenesis, inflammatory diseases, clot and ischemia event, all of which are highly relevant to up-regulated vascular molecular biomarkers [104-107].

Among all the contrast agent centered imaging modalities, molecular ultrasound imaging is the recently emerging one in preclinical translation phase, whose clinical potential might be fully exploited in the next decade. Endoglin (CD105), as an alternative angiogenic factor on the luminal surface of glioblastoma neovasculature, is suitable as binding target of ultrasound contrast agent microbubbles. Molecular US imaging with the aid of targeted MBs is suitable for assessing the neovasculature progression of glioblastoma at early stage by visualization of the pro-angiogenic biomarker endoglin (CD105), which is expressed on the surface of neovasculature wall. This study is a proof of concept strategy which may develop towards pre-clinical translation in the future.

CHAPTER 4 MOLECULAR PHOTOACOUSTIC IMAGING IN TUMOR ENZYME ACTIVITY ASSESSMENT

4.1 Introduction

Tumor is a huge burden of health cost globally. Malignant tumors appear to own the ability to recruit normal tissue cells that contribute to the tumorigenesis process by creating the termed tumor microenvironment (TME). Recent understanding has shifted from the view of tumor-cell centered to all cancer-related development, so called “tumor ecosystem”. For circumstances, the micro-environment of malignant tumors could be adapted to help cancer cells to progress and metastasis, which is now being considered as one important hallmark of cancer. It has been shown that, in the development of cancer, cancer cells and their micro-environment related composites are as important as cancer itself in the evolution and metastasis of cancer. It has been well recognized that various proteases are playing significant roles in the tumor micro-environment (TME) [108].

Among all the proteases, MMPs are such a class of zinc-dependent proteinases. MMPs have been implicated as an important regulator in cancer research since 40 years ago. The point that the MMPs can degrade extracellular matrix (ECM) physical barriers leads to cancer cell invasion and metastasis has been the mainstream understanding in MMPs research [109]. In the past decades, the important discovery that MMPs inhibitor could suppress the metastasis of malignant tumors was progressed to clinical trials of anti-cancer therapy that made use of a variety of MMP inhibitors as targets. Yet, these trails all failed to increase the prognosis [110]. In recent years, the advancement of technology has revolutionized our initial thoughts of the roles of MMPs. For example, MMPs have been found to act as the regulator of a number of signal pathways that control cell growth, apoptosis, inflammation and migration. These insightful findings are potentially to be translated to novel approaches for cancer theranostics [111].

The complexity of the functions of MMPs as a class of proteases comes from a variety of factors in tumor microenvironment (TME). The proteolytic activity of MMPs can be described in different levels, such as genetic regulation, localization, activator, and also inhibitors. The compartmentalization or localization of MMPs often indicates the specific proteolytic activity sites by increasing the local expression concentration. Another critical step for MMPs activity is the conversion of zymogen into active proteolytic form. Generally speaking, MMPs are considered to act as contributor in cancer progression. Elevated expression levels of MMPs have been found in tumor cells themselves and tumor-related cells, such as inflammatory cells, endothelial cells, fibroblasts. Furthermore, the functions of MMPs may differ for cancer at different stages and any individual MMPs may play different roles in different cancer types [111].

4.2 Dynamic proteolytic activity of MMPs

Thus, the understanding of the class of MMPs or even individual MMPs requires the assessment of dynamic proteolytic activity in the TME rather than simply evaluation of the expression levels of proteases, activators and inhibitors because the expression of any individual protease, activator or inhibitor alone can not represent the proteolytic activity. The bio-physical spatio-temporal information (locations and the function time) of MMPs proteolytic activity are fundamental to the understanding of patho-physiological roles of the class of MMPs in TME. Thus, it is necessary to understand the roles and functions of MMPs in details. The most ideal way to address these issue is to develop methods that allow spatio-temporal resolved imaging of proteolytic activity within live cells and animal tissues *in vivo*. The development in last decades mainly focused on the techniques, probes and protocols for imaging and localizing proteolysis in live cells. A lot of important progression has been made by applying those strategies to investigate the dynamic activity of tumor enzymatic process in cancer cells individually or cancer cells plus surrounding TME. By employing known probes-substrate or protease inhibitors for selective targeting, researchers can differentiate the types of protease by their activity nature. However, it is still challenging to know when and where the enzymes function in the TME in animal deep tissue *in vivo*. Emerging noninvasive molecular imaging strategies have started to solve the problem by utilizing a variety of MMP-sensitive probes. It is noteworthy that it is much possible to have additional findings for the underlying mechanism of MMPs when changing studies to more real environment *in vivo*, regarding the failure of anti-cancer therapy in clinical trials [112].

4.3 Overview of imaging strategies for MMPs activity

Until recently, main strategies for imaging MMPs activity are based on the MMP-activatable fluorescence off/on approach, which could result in changing in the probe's optical properties after enzyme cleavage. It was reported that the NIR optical probes could be used to image proteolytic activity of tumor and other biological system in cells and in live animals. These fluorescence resonance energy transfer (FRET) probes are mainly constituted of an MMP cleavable peptide with fluorescent dyes in self-quenching [113-115]. The cleavage of the conjugated peptide would result in the release of fluorescent dye and significantly increased fluorescence. Other than using a fluorescent dye itself as a quencher, a variety of other nanoparticles and dyes have been served as quenchers-donors to generate MMPs-activatable fluorescence probes to improve the performance of the strategies. In addition to FRET, the bioluminescence resonance energy transfer (BRET) [116, 117], MRI [118-120], radiolabeled imaging such as PET/SPECT [121-123] have also been used to design probes to image the proteolytic activity *in vivo*. Fundamentally, all of these enzyme activatable strategies have used substrates, once reacted with a specific enzyme target, could generate signal changes that could be acquired with different imaging modalities. Although the current molecular imaging strategies for dynamic proteolytic activity in TME *in vivo* could not address the challenging task fully, researchers from interdisciplinary areas have made valuable efforts to overcome the hurdles by leveraging emerging imaging techniques with novel probe designs for image contrast, imaging depth of penetration, spatial and temporal resolution, and clinical translation possibility.

4.4 Abilities of molecular photoacoustic imaging

Photoacoustic imaging (PAI) is an emerging modality that attracts much attention of both researchers and clinical physicians because of its unique characteristics. This modality leverages the inherent advantages of optics and acoustics by making use of short-pulsed light radiation to illuminate chromophore and detects acoustic waves generated by photo-thermal conversion and expansion. Thus, PAI is able to provide non-invasive image contrast from absorbed optical energy density by detecting the broadband sound waves at megahertz frequencies. Thereafter, PAI can easily break through the optical diffusion limitation because the ultrasound waves can diffuse with much less scattering in tissue than optical waves. By operating in the near-infrared (NIR) biological window range (680-950 nm), PAI has shown a scalable depth of penetration in several centimeters with a resolution less than one hundred microns for superficial depth of view (<1 cm). Furthermore, latest spectroscopic PAI technique based on multi-wavelength illumination is capable of identifying the optical wavelength-dependent feature (signature) of photoacoustic chromophores by spectroscopic unmixing which is a unique chromophore characterization tool [124, 125].

4.4.1 Label-free photoacoustic imaging

The label-free PAI provides rich contrast information based on light absorption by endogenous chromophores mainly including hemoglobin, lipid, melanin, bilirubin and water. Those endogenous chromophores, as the strongest endogenous photoacoustic contrast suppliers in most biological tissues, can be discriminated and the rich functional information related to those endogenous chromophores could be simultaneously examined in real time, such as hemodynamic physiology, oxygen partial pressure and oxygen saturation, tumor angiogenesis and hypoxia. Nevertheless, most patho-physiological processes of interest are invisible or provide low specific contrast due to the lack of endogenous chromophores. It is of great significance to design novel contrast agents for various biomedical applications to fully exploit the potential of PAI. To date, there are a large variety of exogenous compounds that could be developed into contrast agents of molecular PAI. These exogenous compounds can be visualized and identified in a similar spectroscopic method by resolving the distribution and concentration with specific spectral signatures. However, it is noteworthy that the unmixing of relative strong endogenous background signal (mainly from blood) is an issue when applying exogenous contrast agent in molecualr PAI applications [126]. To this end, to design an ideal PAI contrast agent, two physical parameters are key considerations for compound selection, which are extinction coefficient and absorption spectra with specific peak. Nanoparticles (NPs), as one of the most popular class of composites for molecular PAI, is due to the advantages in flexibility of their chem-physical and biochemical properties. More importantly, nanoparticles usually have high molar extinction coefficients compared to other contrast agent compounds options such as small-molecule dyes [127-129]. NPs may be synthesized with different materials into a variety of shapes and sizes (usually tens to hundreds nano meter range) and can be tuned with different surface properties, reactivity and optical characteristics. The large surface area of NPs brings them the ability to be good drug loader or targeting binding possibilities. However, due to their larger size, the applications of NPs are also limited by their poorer biocompatibility due to longer time periods in the reticuloendothelial system.

4.4.2 Gold nanocages (GNCs) as PAI contrast agent

In comparison with solid gold nanoparticles (GNPs), the gold nanocages (GNCs) with the hollow interiors and porous walls are ideal for biomedical applications such as drug loading and drug delivery because of interior structure for high loading efficacy. Further, this nanostructure could prevent unwanted release in normal tissue area. Note-worthily, GNCs are good candidates for tumor related theranostic applications because 1) the shape of GNCs can be conveniently tuned. For example, the size, porous surface and shell thickness (thinner shells lead to a red shift) could be optimized for different applications to improve the properties of biocompatibility, bio-distribution, optical absorption characteristics and imaging penetration; 2) The flat surface of GNCs could be used as good substrate for controlled functionalization and bioconjugation to other ligand, which would enrich the GNCs' application potentials; 3) Also, GNCs (< 50 nm) can be produced by convenient method in large quantities with high accuracy [130].

Superiorly, the inert nature of Au nanoparticle guarantees GNCs as candidates with good bio-compatibility and bio-stability in the real biological environment *in vivo,* such as blood pool and liver. As plasmonic nanoparticles, GNCs and the localized surface plasmon resonance (LSPR) peak can be precisely tuned to be in the biological window which covers near-infrared (NIR) region of 680-1200 nm. This unique NIR biological window makes GNCs appropriate for biological applications [130]. Because in the transparent biological NIR window, optical waves can penetrate more deeply into soft tissues with much less optical attenuation, which would facilitate the *in vivo* optical illuminated imaging (e.g photoacoustic imaging) and related theranostics applications. Pioneers in this field by employing conventional and easy methods for tuning the optical spectral characteristics and peak wavelength position have exploited the potential of GNCs as a promising platform of PAI contrast agent for a variety of biomedical applications, such as cerebral cortex, deep located sentinel lymph nodes mapping, active-targeting melanoma detection [131-133]. These preliminary reports have outlined the the promising future of GNCs platform to be applied in the field of molecular PAI in the future.

4.5 Research gap

Taken together these unique features, PAI with the aid of properly designed contrast agents is potential to contribute to the imaging of proteolytic activity *in vivo*. And, it is potential to further provide information with high sensitivity and spatial resolution in real-time. Furthermore, multi-spectral PAI is emerging as a new powerful tool to offer unique chromophore sites identification in TME which is a need for spatio-temporal imaging of proteolytic activity *in viv*o. Up to now, PAI contrast agents mostly rely on passive enhanced accumulation at tumor area *via* enhanced permeability and retention (EPR) effect or simple active targeting between recognition ligand and overexpressed biomarkers. Thus, those so called “always on” probe based on accumulation could not provide high contrast to noise ratios and unable to meet the requirement for imaging the dynamic activity of proteolytic enzyme.

4.5.1 Activatable PAI contrast agent

In comparison with targeted PA imaging agents with the signal always on, activatable PA imaging agents can only be activated by specific biomolecular recognition or interaction, which leads to improved imaging sensitivity and specificity with higher signal-to-noise ratios. Upon activation, the PA probes typically alter their absorption status through retention, clearance, degradation, or enhancement of nonradiative relaxation. That is to transfer the enzyme activity into measurable and quantifiable signal rather than measuring the local concentration of enzyme expression. Thus, activatable PA imaging contrast agent could provide activity-dependent/concentration-independent contrast information. Finally, molecular PAI could provide correlation information between signals and patho-physiological processes of interest in real time.

The existing activatable probes generally rely on fluorescence as signal readout, which has the shadow tissue penetration issue and thus limits its *in vivo* applications. Although reports relevant to PAI contrast agents are increasing greatly, the activatable PA probes have been less developed so far, maybe due to their relative critical requirement for design and application. Some pioneer research groups have developed several activatable PA probes based on specific enzymatic cleavage to target substrate including MMPs, furin, and hyaluronidase (HAase). Such enzymatic cleavage was used to separate chromophores or initiate further self-assembly so as to afford changes in PA signals with deep tissue penetration 152-154]. 20-24, 25

Because the PA signals are mainly determined by the absorption-related heat generation, nearly all physically materials with optical absorption capabilities in the near-infrared (NIR) window could possibly be used for PAI contrast agents compounds theoretically. For the same reason, the sensitivity of PAI is usually lower than the fluorescent probes. Thus, developing PAI activatable contrast agent by selecting compounds with high photothermal conversion efficiency is preferred because it would help lower the dosage of activatable PA probes by increasing their sensitivity, potentially mitigating the toxicity issue.

4.5.2 Design of GNC-based activatable photoacoustic contrast agent

Although activatable PAI contrast agent is still in the concept-of-proof phase, we would like to utilize the mechanism (peptide-specific cleavage strategy) that makes use of a cleavable peptide-substrate that is specific to MMP-2 in our probe design. The gold nanocages (GNCs) compound is to be tuned to have absorption peak at around 800 nm for deep penetration imaging and less optical attenuation. The modification flexibility of GNCs platform makes it suitable for activatable probe design. By easy chemical conjugation of small molecule fluorescent dye with distinctly different absorption peak, the photoacoustic spectra signature of GNC-based contrast agent is feasible to have two distinct absorption peaks in the NIR range. Furthermore, the high optical extinction coefficient and photothermal conversion efficacy of GNCs make the GNC-based activatable probe ideal in TME environment *in vivo* because this feature helps suppress the blood PA signal from the angiogenesis in tumor area. By tuning the conjugation amount of small molecule fluorescent dye on the surface of GNCs, it is easy to control the relative PA contributions of large molecule GNCs and small molecule dye, which would bring valuable feature to the spectral signature of activatable PAI probe. Once cleaved, the resulting dynamic changes in the spectral signature of activatable PAI probe could be used to predict the spatio distribution (distribution sites) of dynamic proteolytic activity in real time (temporal-resolved) and derived as ratiometric factor to quantify the dynamic cleavage proteolytic process *in vivo*.

4.5.3 Ability of the GNC-based activatable photoacoustic contrast agent

The localized surface plasmon resonance (LSPR) peak of the GNCs would be designed to be 800 nm while the peak of small-molecule dye was selected to be 680 nm which would be conjugated on the surface of the GNCs *via* cleavable peptide. The cleavage reaction would change the wavelength-dependent photoacoustic spectra signature of the photoacoustic contrast agent due to the quick washout of the small molecule dye. In the proteolytic activity cleavage sites, the washout speed of the large molecule GNCs (~30-50 nm) and small-molecule dye (~1 nm) would be quite different which would result in unique photoacoustic contrast signal ratiometric change *in vivo*. The ratiometric quantification would be an indirect readout of proteolytic activity levels with location and time information. In the meantime, the distribution of uncleaved activatable probe, cleaved activatable probe and dye molecules would be possibly unmixed by spectroscopic PAI, which could also be used for assessing the proteolytic activity in a spatio-temporal resolved way.

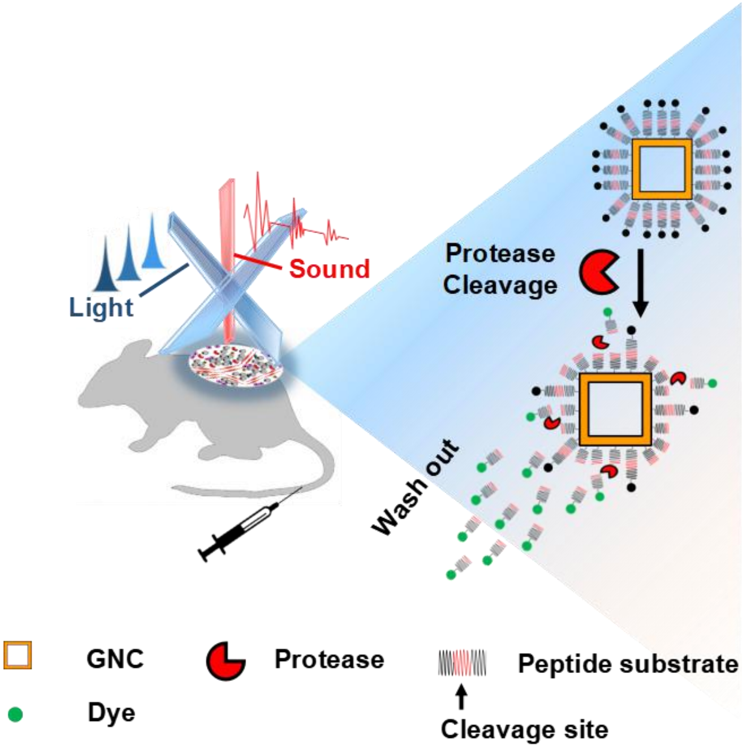

Figure 4.1. Design of activatable GNC-based nanoprobe for molecular photoacoustic imaging of enzyme *in vivo.*

4.6 Synthesis and characterization of activatable PAI contrast agent

4.6.1 Preparation of activatable probe

The gold nanocages (GNCs) were prepared by the reduction of $HAuCl_4$ on a silver nanoparticle framework according to a previously reported method [134]. Briefly, the silver nanoparticles were first synthesized by stirring a silver nitrate solution (0.1 M, 50 mL) with sodium citrate (0.5 M, 1.5 mL) and sodium borohydride solutions (0.1 M, 1.5 mL) at room temperature. Larger silver nanoparticles were grown from these stock solutions with additional hydroxylamine hydrochloride. The reducing reaction was initiated by the addition of hydroxylamine hydrochloride solution (0.2 M, 1.5 mL) and stirred for 10 min. Afterwards, silver nitrate solution (0.1 M, 1 mL) was added, and the mixture was stirred overnight. The prepared silver solution (50 mL) was heated to 100°C, and $HAuCl_4$ (25 mM, 800 μL) was added dropwise. The resulting suspension was stirred vigorously for 30 min. All chemicals were obtained from Sigma-Aldrich (Sigma-Aldrich Chemical, St. Louis, MO, USA) unless otherwise stated.

The GNCs were functionalized by the addition of the heterobifunctional linker Thiol-PEG-NH_2 (MW ≈ 2,000 g/mol, Laysan Bio, Arab, AL, USA) at 6 mg per 30 mL of GNC solution. The peptide substrate NH_2-GKG*PL**GV**R*GC-NH_2 (> 95% purity, Bankpeptide Biological Technology, Hefei, China), which possesses a cleavage site between Gly and Val (as indicated by bold italics) [135], was first dissolved in DMSO (10 mg/mL, 200 μL), followed by the addition of N-(3-dimethylaminopro-pylN'-ethylcarbodiimide) hydrochloride (EDC) (2 mg) and N-hydroxysulfosuccinimide (sulfo-NHS) (3 mg) at room temperature with continuous mixing to activate the carboxylic group in the peptide. Then, GNC-PEG-NH_2 was added into the solution to react overnight at room temperature. Excess peptide molecules were removed by ultracentrifugation (Avanti J-25; Beckman Coulter., Fullerton, CA, USA) at 4000 rpm, and the GNC-peptide was purified with Milli-Q water (Millipore, Bedford, MA, USA). Finally, the Alexa Fluor 680 NHS ester (Thermo Fisher Scientific, San Jose, CA, USA) in DMF (1 mg/mL) was coupled to the GNC-peptide through the reactive NHS ester group. After one hour of reaction, the unreacted Dye680 was collected by ultracentrifugation, and the amount of conjugated Dye680 at the surface of the GNCs was determined using a UV-Vis spectrophotometer (Cary 8454; Agilent, Singapore).

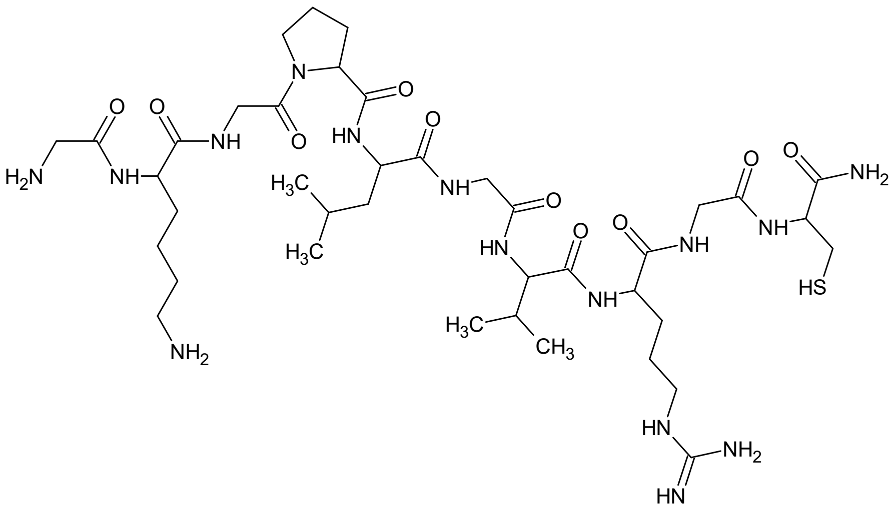

Figure 4.2. Chemical structure of the MMP-2 enzymatic peptide substrate(NH$_2$-GKG*PL**GV**R*GC-NH$_2$) (> 95% purity, Bankpeptide Biological Technology, Hefei, China), which possesses a cleavage site between Gly and Val, as indicated by bold italics.

4.6.2 Dynamic light scattering (DLS) profiles of nanoparticles

The hydrodynamic sizes of the GNCs and the GPD probe were measured by dynamic light scattering (DLS) using a Nano Zetasizer (Malvern Instruments, Malvern, Worcestershire, UK) with a 90° scattering angle at 25°C. The data were analyzed with Zetasizer software 6.32 (Malvern Instruments, Malvern, Worcestershire, UK). The results showed that the GNCs and GPD probe were stable in PBS.

4.6.3 Molar concentration of nanoparticles

Inductively coupled plasma optical emission spectrometry (ICP-OES) (Agilent 700 Series; Agilent Technologies, Santa Clara, CA, USA) was used to determine the concentration of the nanoparticles. The GNCs and the GPD probe were digested by aqua regia (a mixture of nitric acid and hydrochloric acid at an optimal molar ratio of 1:3) and diluted with 1% HNO_3. Solutions at 1 ppm, 2 ppm, 5 ppm, 10 ppm, and 20 ppm in 1% HNO_3 were used as internal standards. Every data point was expressed as the mean (± SD) of triplicate measurements.

4.6.4 Determination of average number of gold atoms per GNC

The average outer (D_1) and inner (D_2) diameters of the GNCs were measured to be 31.7 nm and 20.5 nm, respectively, by TEM. Under the assumption that those GNCs have a spherical shape and a uniform face centered cubic (fcc) structure, the average number of gold atoms per GNC (N) can be calculated by **Equation (4.1)**, where ρ is the density of fcc gold (19.3 g/cm^3), N_A is Avogadro's constant, and M is the atomic weight of gold (197 g/mol):

$$N = \frac{\pi}{6}\frac{\rho N_A (D_1^3 - D_2^3)}{M} \qquad \textbf{(4.1)}$$

4.6.5 Determination of molar concentrations of GNCs

The molar concentrations of gold atoms in the as-prepared GPD probe and GNC-PEG-NH_2 were measured by ICP-OES. The molar concentration of the as-prepared GPD probe and GNC-PEG-NH_2 was calculated by dividing the total number of gold atoms (N_{total}) by the average number of gold atoms per GNC (N) according to **Equation (4.2)**, where V is the volume of the solution, and N_A is Avogadro's constant.

The concentrations of each diluted solution may be calculated from this initial concentration according to their relative concentrations as described below:

$$C = \frac{N_{total}}{NVN_A} \qquad \textbf{(4.2)}$$

4.7 Determination of the molar extinction/absorption coefficient of the GNCs

The ratio of the absorption cross section (C_a) to the extinction cross section (C_{ext}) was experimentally measured according to a previously reported method to determine the effectiveness of the nanoparticle at converting incident light into heat.[41]

$$ratio = {}^{c_a}\!/_{c_{ext}}$$

4.7.1 The molar extinction coefficient (u_{ext}) and extinction cross sections (C_{ext}) of GNCs were determined according to the Lambert–Beer law as described by **Equation (4.3)**.

$$Attenuation = \log({}^{I_0}\!/_{I}) = \mu_{ext} lc \qquad \textbf{(4.3)}$$

where

$$\mu_{ext} = N_A C_{ext}$$

The GNC solution was diluted to different concentrations, and the absorption spectrum of each diluted sample was measured using a UV-Vis spectrophotometer

(Cary 8454; Agilent, Singapore). The UV-Vis absorbance measurement at 800 nm of each diluted sample was plotted against the molar concentration of the solution, as shown in **Figure 4.3**. A good linear fit of the experimental data was found for the GNCs.

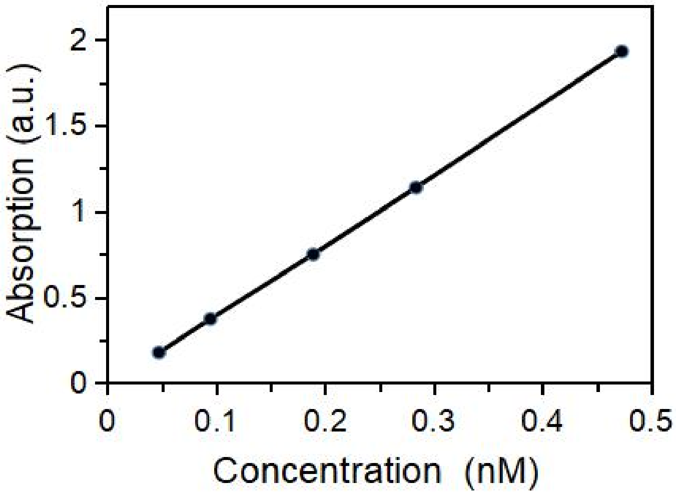

Figure 4.3. The linear relationship between the optical absorption amplitude and the concentration of GNCs at the absorption peak wavelength (λ_{ab} = 800 nm).

4.7.2 The molar absorption coefficient (u_a)

The PA effect is theoretically based on the photothermal conversion efficiency of chromophores, as shown in **Equation (4.4)**. PA_0 is the initial PA pressure due to laser excitation, Γ is the Grüneisen parameter, and F is the optical fluence. Thus, the PA signal is expected to be intrinsically proportional to the molar absorption coefficient (u_a) of chromophores within a certain concentration range.

$$PA_0 = \Gamma \mu_a F \qquad \textbf{(4.4)}$$

where

$$\mu_a = N_A C_a$$

The molar absorption coefficient (u_a) of GNCs could be derived by benchmarking against a chromophore (e.g., fluorescent dye Alexa Fluor 680) with a known molar absorption coefficient. The experimental measurement was performed using a Vevo2100 LAZR System (FUJIFILM VisualSonics, Toronto, Canada) with a LZ-250 linear array transducer (center frequency 21 MHz, 256 elements) to acquire the PA signal, as shown in **Figure 4.4**.

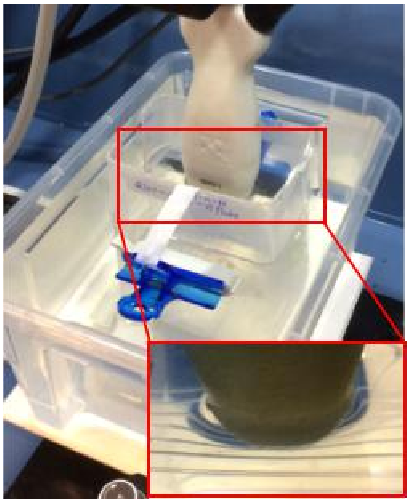

Figure 4.4. The experimental setup for multispectral PAI of nanoparticles in PE tubes using a Vevo2100 LAZR System.

4.8 Photoacoustic spectra characterization

Before using PA imaging to detect the MMP-2 *in vivo*, the PA signals of free nano-materials will be tested using Vevo 2100 LAZR photoacoustic imaging system (VisualSonics Inc., Toronto, Canada) before and after enzyme cleavage in solutions.

We will choose the peaked absorbance wavelength (790 nm) for ICG imaging and 800 nm for GNC imaging. We expect that the GPI complex will show strong PA signals at both 790 nm and 800 nm before enzyme cleavage. However, after cleavage and purification, the PA signal at 790 nm is expected to significantly decrease, while that at 800 nm will have little change.

4.8.1 The multispectral PAI experiment

The principle of the multispectral PAI technique is shown in **Figure 4.5**. PA images at multiple wavelengths are used to unmix specific chromophore composites, relying on distinct PA spectra signatures. Multispectral PAI can distinguish the cleaved GPD probe from uncleaved GPD probe and relatively unvarying tissue background, by acquiring PA images at multiple wavelengths and estimate the PA chromophore composition contributions based on per-pixel.

$$\mu_c^i(\lambda) = \varepsilon_c(\lambda)c_c^i + \varepsilon_u(\lambda)c_u^i + B(\lambda) \qquad \textbf{(4.5)}$$

Where $\mu_c^i(\lambda)$ is the wavelength-dependent optical absorption coefficient within pixel ***i*** that was acquired by multispectral PAI, $\varepsilon_c(\lambda)$, $\varepsilon_u(\lambda)$, c_c^i , c_u^i are the extinction coefficient of cleaved GPD probe, uncleaved GPD probe and their distribution within the pixel. $B(\lambda)$ is the photoacoustic signal contribution from the background chromophores. The accumulation and distribution of of cleaved GPD probe and uncleaved GPD probe could be estimated by applying linear regression to **Equation (4.5)** at selected multiple wavelengths. In complicated living tissue background, main background PA signal is contributed by blood (HbO_2 and Hb). In the *in vivo* subcutaneous tumor model, the assumption of the multispectral PAI algorithm is that the optical wavelength-dependence of the laser fluence due to the absorption spectra of tumor tissue background can be neglected [136].

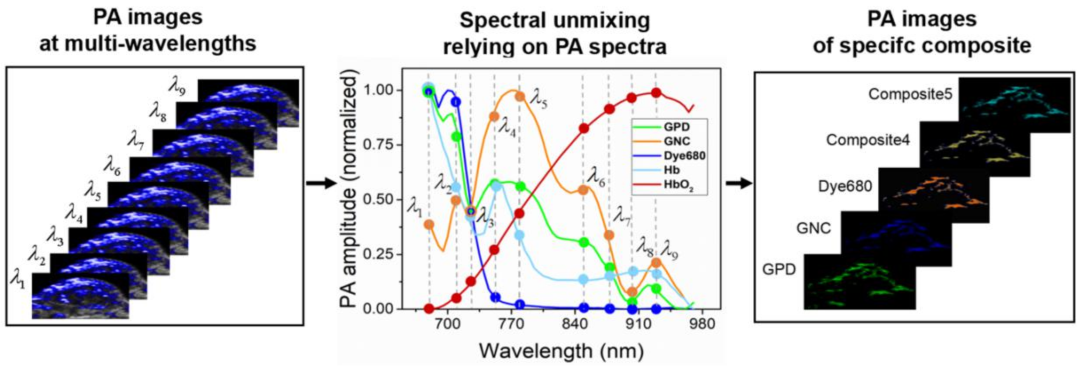

Figure 4.5. PA images at multiple wavelengths are used to unmix specific chromophore composites by relying on distinct PA spectral signatures.

4.9 Detection of protease activity in solution

Protease MMP-2 catalytic domain (ENZO Life Sciences, Ann Arbor, USA) (0.05 mg/mL, 20 μL) in 2 μL of TCNB buffer solution (50 mM Tris, 10 mM $CaCl_2$, 150 mM NaCl, 0.05% Brij 35) (pH 7.5) was incubated for 15 min at 37°C before incubation with the GPD probe. The GPD probe (0.45 nM, 200 μL) was incubated with the prepared MMP-2 catalytic domain (0.05 mg/mL, 20 μL) in the absence or presence of a potent broad spectrum MMP inhibitor GM6001 (Abcam, Cambridge, UK) (10 mM, 2 μL) that could inhibit the activities of many MMPs including MMP-2, at 37°C for three hrs. The cleaved dye containing the peptide fragment was removed by ultrafiltration. Three trials were conducted in parallel. The UV-Vis absorption spectra of the residual solution were recorded.

4.10 Typical cell-based test of enzyme activity

4.10.1 Cell culture

The U-87 MG human glioblastoma cell line and MS1 mouse endothelial cell line were purchased from the National Infrastructure of Cell Line Resource (Chinese Academy of Science, Shanghai, China). U-87 MG cells were cultured in Eagle's Minimum Essential Medium (GIBCO, Grand Island, NY, USA) supplemented with 10% fetal bovine serum (Invitrogen, Carlsbad, CA, USA) and 1% penicillin-streptomycin (Invitrogen, Carlsbad, CA, USA) at 37°C in a humidified atmosphere of 5% CO_2. MS1 cells were cultured in Dulbecco's Modified Eagle's Medium (DMEM) (GIBCO, Grand Island, NY, USA) supplemented with 5% fetal bovine serum and 1% penicillin-streptomycin at 37°C in a humidified atmosphere of 5% CO_2.

4.10.2 Detection of protease activity in live cells

U-87 MG cells with high MMP-2 expression and MS1 cells with low MMP-2 expression were seeded separately on a 35 mm confocal dish (MatTek, Ashland, USA) at a density of 5×10^4 cells per dish and allowed to grow until 70% confluent. For the inhibitor groups of both cell lines, the medium was removed, and then serum-free medium with 10 μM MMP-2 inhibitor GM6001 (Abcam, Cambridge, UK) was added to the cell dishes and incubated for 1 hr. Then, the GPD probe was added at a concentration of 0.45 nM and further incubated at 37°C for 3 hr. For the experimental groups of both cell lines, after being washed 3 times with PBS, the cells were incubated with the same concentration of GPD probe in serum-free medium for 3 hrs. Afterwards, the culture medium was removed, and the cells were washed 3 times with

PBS. The cells were then counter-stained with Hoechst 33342 (Molecular Probes, Eugene, OR, USA) at a concentration of 0.25 μg/mL to stain the cell nucleus. Intracellular fluorescence images were captured using a confocal laser scanning microscope (Leica TCS SP8; Leica Microsystems, Wetzlar, Germany) with a 63 × objective (Ex. 650 nm/Em. 690-740 nm).

4.10.3 Toxicity of the GPD probe

The cell cytotoxicity of the GPD probe was measured using the 3-(4,5-dimethylthiazol-2-yl)-2,5-diphenyltetrazolium bromide (MTT) proliferation assay. U-87 MG cells were seeded in 96-well plates to a total volume of 150 μL per well and a cell density of 5×10^3 at 37°C in 5% CO_2 and incubated for 24 hr. Different concentrations of the GPD probe were added to each well with five duplicates for each concentration. After 24 hr of incubation, the suspensions were removed, and the cells were washed three times with PBS. The MTT solution (Sigma-Aldrich Chemical, St. Louis, MO, USA) (0.5 mg/mL, 100 μL) in PBS was added to each well, and the mixtures were incubated at 37°C for 4 hr. After incubation, the remaining MTT solution was removed, and 100 mL of a 1:1 DMSO/EtOH mixture was added to each well to dissolve the resulting crystals. The absorption of the mixture was measured at 490 nm using a SpectraMax M3 multi-mode microplate reader (Molecular Devices, Sunnyvale, CA, USA).

4.11 Photoacoustic imaging *in vivo*

4.11.1 PA spectral signature characterization

The PA spectral signatures of nanoparticles were obtained using the Vevo2100 LAZR system (FUJIFILM VisualSonics, Toronto, Canada) with an LZ-250 linear array transducer (center frequency 21 MHz, 256 elements, lateral and axial resolution of 165 and ~75 μm, respectively, maximum imaging depth of 20 mm) to detect transverse coregistered ultrasound and multispectral PA images, and a tunable Nd:YAG laser system (OPOTEK, Carlsbad, CA, 680-970 nm, 20 Hz repetition rate, 5 ns pulse width, 50 mJ pulse peak energy) was used to trigger the PA system, exciting the tissue with optical pulses to generate PA signals. Tunable laser light was delivered downward from both long sides of the transducer surface and focused at ~10 mm from the transducer surface. The transducer surface was maintained at 10 mm from the Intramedic polyethylene-50 tube (Becton Dickinson, Sparks, MD, USA) containing nanoparticles immersed in DI water.

4.11.2 Xenograft tumor models

All procedures using laboratory animals were approved by the Department of Health, The Government of the Hong Kong Special Administrative Region and the Hong Kong Polytechnic University Animal Subjects Ethics Sub-committee. Tumors were established by the subcutaneous injection of 5 × 10^6 human glioblastoma U-87 MG cells dissolved in Matrigel (1:1) (BD Biosciences, San Jose, CA, USA) into the right hind limb of 6–8 week-old female nude mice (Centralized Animal Facilities, The

Chinese University of Hong Kong, Hong Kong). The mice were used for the experiment when the tumor size reached ~100 mm^3.

4.11.3 *In vivo* photoacoustic (PA) imaging

For intratumoral administration, nude mice bearing U-87 MG tumors were intratumorally injected with GPD probe (0.2 nM, 100 µL) and imaged at different time points after injection by a Vevo2100 LAZR system at the two representative wavelengths (680 nm and 770 nm). For quantitative calculation, the region of interest (ROI) was drawn over the tumor area, and the average PA signals were measured. The protease activity *in vivo* was quantified using the ratio of PA signal increases at 680 nm and 770 nm:

$$\Delta PA_{680}/\Delta PA_{770} = (PA_{680\,postinjection} - PA_{680\,preinjection})/(PA_{770\,postinjection} - PA_{770\,preinjection})$$

For intravascular administration, nude mice bearing U-87 MG tumors were photoacoustically imaged using a Vevo2100 LAZR system after tail vein injection of the GPD probe (0.9 nM, 200 µL) at different time points using multispectral PAI.

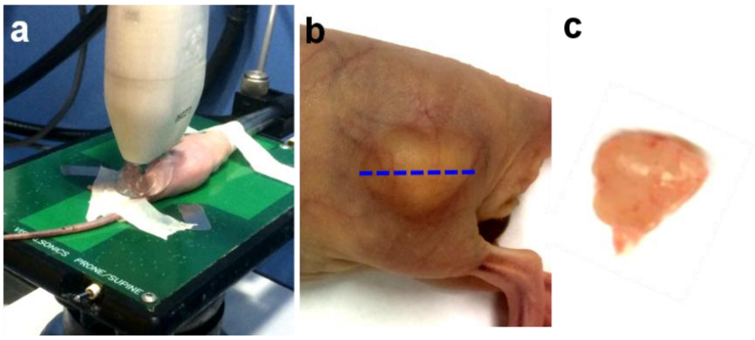

Figure 4.6. *In vivo* multispectral PAI was conducted on a xenograft tumor model using a Vevo2100 LAZR System. (a) *In vivo* PA imaging experiment setup; (b) PA imaging cross section plane of the subcutaneous tumor on nude mouse; (c) freshly excised tumor specimen.

4.11.4 *Ex vivo* cryosectioning and epi-fluorescence imaging

Immediately after the *in vivo* PAI experiment on the xenograft tumor model, the agar-embedded tumor specimen was stored in freezing medium. The tumor specimens in syringes were snap-frozen at -80°C. After freezing, cryosections through the entire sample were made at 50 μm intervals along the coronal plane to represent the *in vivo* sectional imaging results. Every 1 mm, the thickness of the section was reduced to 8 μm to obtain sections suitable for additional histological analysis. Several cryosectioning slices were captured on glass slides. Finally, MMP-2 staining and cell nucleus staining were performed and observed under a Leica DM 2500 upright microscope (Leica Microsystems, Wetzlar, Germany), and pictures taken and automatically digitized using the Pannoramic MIDI (3D HISTECH, Budapest, Hungary), and then they were analyzed using the Pannoramic Viewer software (3D HISTECH, Budapest, Hungary).

4.12 Results

4.12.1 Synthesis and characterization of probe

Figure 4.7. shows the schematic design of the activatable PA probe consisting of two chromophores (i.e., GNCs and fluorescent dye molecules) conjugated *via* an enzymatic peptide substrate specifically cleavable by MMP-2. The resonance absorption peak of GNCs was tuned to 800 nm in the NIR biological window to achieve a greater imaging depth of penetration. The fluorescent dye Alexa Fluor 680 (Dye680) was selected for coupling with the GNCs considering the following properties: 1) its optical absorption peak is distant from that of the GNCs, and 2) it has exceptional resistance to photobleaching. To prepare the probe, GNCs were obtained through a galvanic replacement reaction between silver nanoparticles and a $HAuCl_4$ solution [134]. Next, to improve the stability and biocompatibility of the GNCs and facilitate further conjugation with Dye680, the GNCs were PEGylated *via* conjugation with $SH\text{-}PEG\text{-}NH_2$. The Dye680 molecules were then covalently linked to the surface of the PEGylated GNCs by an MMP-2 specific enzymatic peptide substrate. The obtained GNC-peptide-Dye680 (GPD) probe was purified by centrifugation and washed with Milli-Q water.

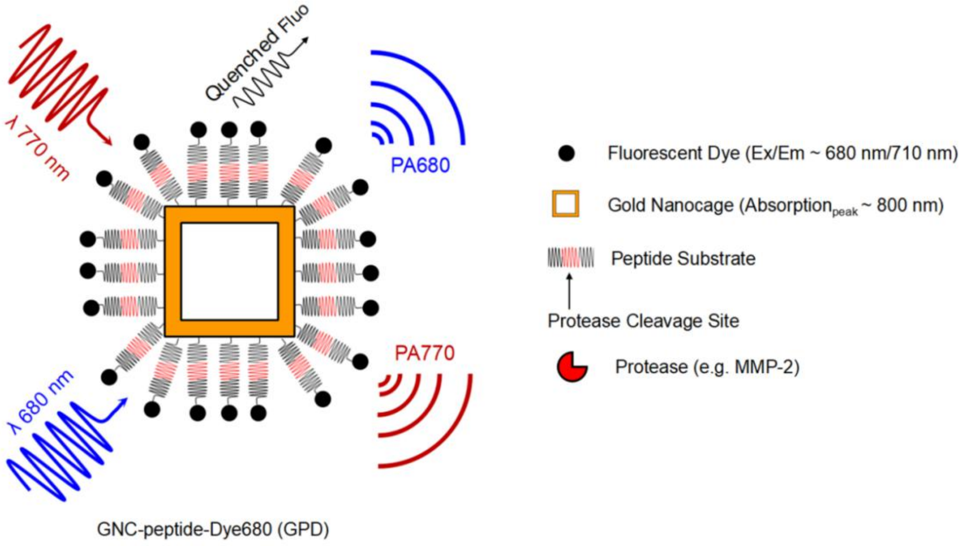

Figure 4.7. Schematic design of the activatable GPD probe . Before activation, the GPD probe was expected to produce a strong PA signal with contributions from the GNCs with an LSPR absorption peak at ~800 nm and from the fluorescent dye Alexa Fluor 680 with an absorption peak at ~680 nm, conjugated by a specific peptide substrate (cleavable by MMP-2). The as-prepared GPD probe showed two characteristic PA spectrum peaks at 680 nm and 770 nm, which were close to the optical absorption spectrum peaks. The PA signal changes at 680 nm and 770 nm in multispectral PAI were selected to represent the chromophore composite changes within the GPD probe. In addition, the fluorescence quenching effect between the GNCs and the Dye680 molecules was used to test the synthesis of the GPD probe.

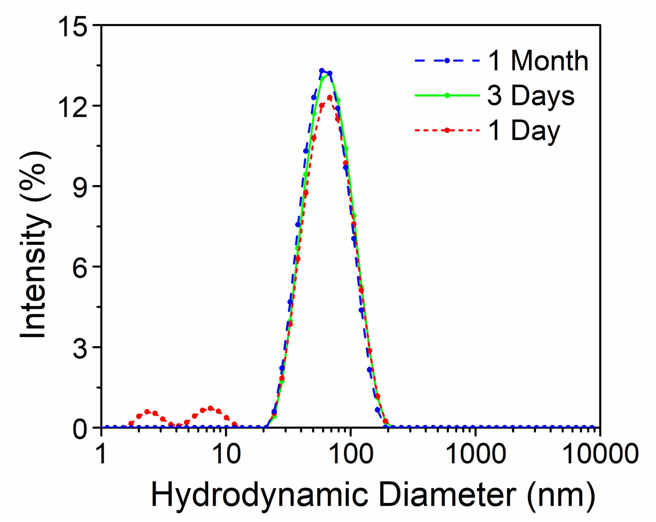

Figure 4.8. Dynamic light scattering size distribution of GNCs.

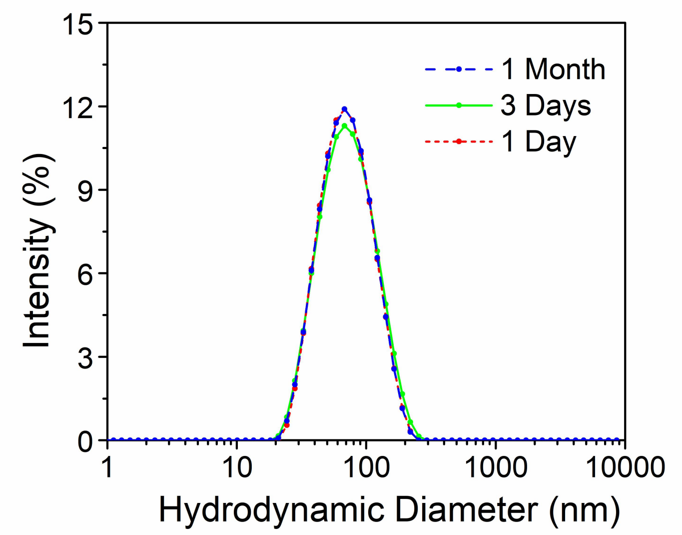

Figure 4.9. Dynamic light scattering size distribution of GPD probe.

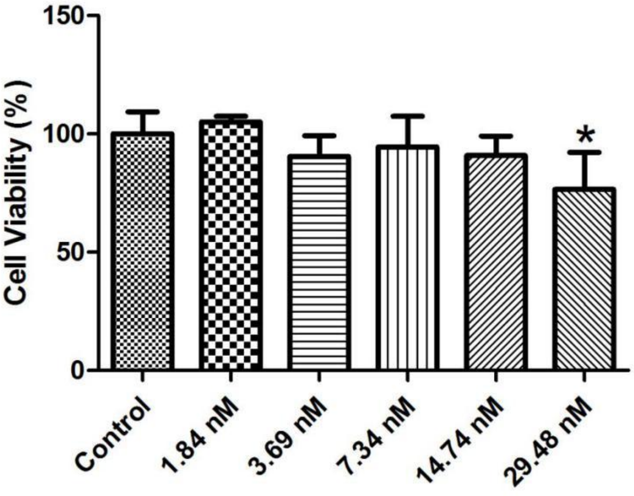

Figure 4.10. Cell cytotoxicity of GPD probe to U-87 MG cells ($n = 5$, $^*p < 0.05$). No significant cytotoxicity to U-87 MG cells after incubation with the GPD probe for 24 hr at 37°C.

4.12.2 TEM morphology and size distribution

Next, the morphology and size of the GPD probe were characterized by transmission electron microscopy (TEM), as shown in **Figure 11.(a1)**. The TEM image indicated the presence of a 2D lattice fringe, and the spacing was determined to be 2.3 Å, as shown in **Figure 11.(a2)**, which corresponded well to the [111] lattice plane of gold [134]. **Figure 11.(b1)-(b2)** shows the size distribution of the outer and inner diameters of the GPD probe, which have means of 31.7 ± 2.6 nm and 20.5 ± 4.8 nm, respectively. The optical absorption spectra of the pure GPD probe, pure GNCs and pure Dye680 were then obtained and are shown in **Figure 11.(c)**. The as-prepared GPD probe showed two characteristic absorption peaks at 680 nm and 800 nm, which corresponded well to those of pure GNCs and Dye680 molecules. The two characteristic absorption peaks also indicated no detectable aggregation in the as-prepared GPD probe. The strong absorption peak of the GPD probe at 680 nm confirmed the successful attachment of Dye680 molecules to GNCs. The payload of Dye680 to GNCs was estimated to be 8 μM of Dye680 per milliliter of GPD probe. Considering the face-centered cubic structure of atoms in gold nanoparticles and nanocages, the molar concentration of the GPD probe was approximately 0.905 nM, while the grafting number of Dye680 molecules conjugated on each particle was approximately 8800. The fluorescence emission spectrum of the GPD probe is shown in **Figure 11.(d)**. The peak at 710 nm in the emission spectra of the GPD probe was due to the fluorescence emitted from Dye680, supporting the successful attachment of Dye680 molecules to GNCs. The fluorescence emission intensity of the GPD probe was significantly lower than that of pure Dye680 at the same concentration. This decrease reflected a quenching effect due to nanosurface energy transfer (NSET) between the conjugated GNCs and Dye680 molecules [137].

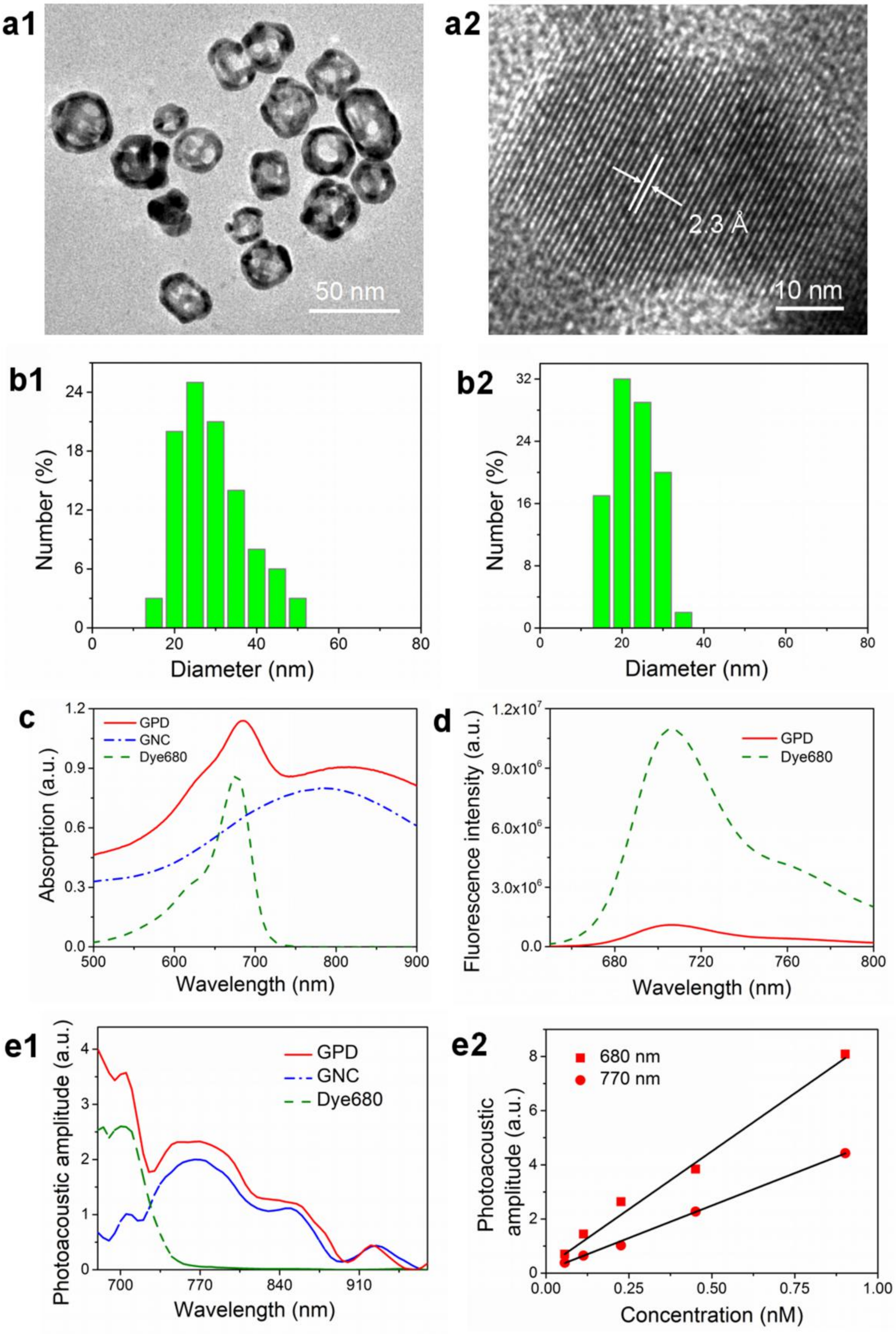

Figure 4.11. Preparation and characterization of the as-prepared GPD probe. (a1) TEM image of GPD probe (scale bar = 50 nm) and (a2) high-resolution TEM image (scale bar = 10 nm). Size distribution of the GPD probe: (b1) outer diameter and (b2)

inner diameter of GPD probe. (c) UV-Vis absorption spectra of GPD probe, GNCs and Dye680. (d) Fluorescence emission spectra of GPD probe and Dye680 (λ_{ex} 710 nm) (at the same concentration as the Dye680 molecules attached to the GPD probe). (e1) PA spectral signatures of GPD probe, GNCs and Dye680; (e2) the linear relationship between the PA amplitude and the concentration of the GPD probe at the two representative wavelengths of multispectral PAI.

4.12.3 Photoacoustic properties

Furthermore, the PA properties of the as-prepared GNCs were characterized, including the molar extinction cross section coefficient, the molar absorption cross section coefficient and the energy conversion efficiency (ratio of the absorption to the extinction cross section coefficient). The molar extinction coefficient of the GNCs at the absorption peak wavelength (800 nm) was calculated to be 4.12×10^9 $\mathrm{M^{-1}cm^{-1}}$, which was much higher than that of hemoglobin (1×10^3 $\mathrm{M^{-1}cm^{-1}}$). In addition, the molar absorption coefficient of the GNCs was measured to be 3.89×10^9 $\mathrm{M^{-1}cm^{-1}}$. Thus, the energy conversion efficiency was 0.94. This high energy conversion efficiency indicated that the GNCs were much more effective in absorbing than scattering the incident light. Since PAI is an absorption-based imaging modality, the high molar absorption cross section coefficient and high energy conversion efficiency demonstrated that the as-prepared GNCs could be an excellent platform for the development of PA probes. **Figure 11.(e1)** plots the PA intensity as a function of wavelength for the pure GPD probe, pure GNCs and pure Dye680. Each particle has a distinct PA spectral signature. For *in vivo* applications, the PA signals from the GPD probe are usually mixed with signals from other sources (e.g., hemoglobin) and background noise. Due to the differences in the intrinsic PA spectral signatures, it is feasible to use multispectral PAI to unmix the signals from different composites [136]. The as-prepared GPD probe showed two characteristic PA spectral peaks at 680 nm and 770 nm, which were close to the wavelengths of the optical absorption spectral peaks. Consequently, the multispectral PA signal changes at these two wavelengths were selected to represent the composite changes within the GPD probe (i.e., GNCs and dye molecules). In addition, the PA amplitude of the GPD probe at these two representative wavelengths was linearly related to the concentration in the testing range, as shown in **Figure 11.(e2)**.

The PA spectral signatures were acquired by a Vevo2100 LAZR System in solution. Images at multiple wavelengths (680 nm, 710 nm, 720 nm, 755 nm, 770 nm, 845 nm, 880 nm, 900 nm, 920 nm) were combined with the spectral unmixing software Multiplexer (FUJIFILM VisualSonics, Toronto, Canada) to differentiate specific chromophore composites. Validation testing was conducted by using this strategy to unmix pure chromophores (e.g., fresh chicken blood, GPD probe, GNC, Dye680 and DI water) in PE tubes, as shown in **Figure 12**.

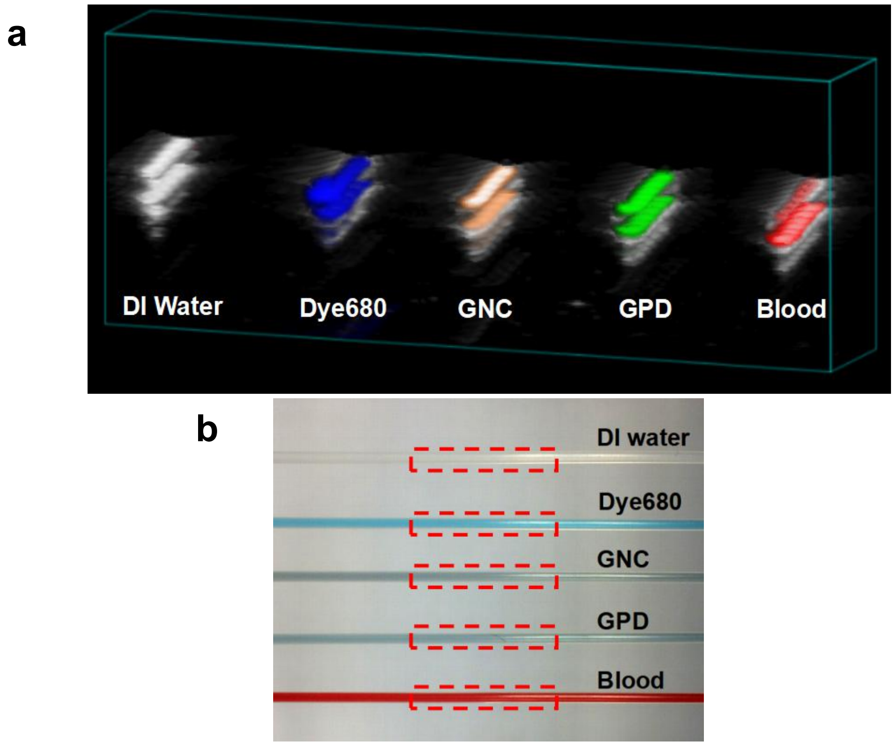

Figure 4.12. The validation of the multispectral PAI technique in solution. (a) multispectral PA imaging (3D volumetric scanning) was tested to differentiate PA chromophore composites in PE tubes (e.g., fresh chicken blood, GPD probe, GNC, Dye680 and DI water). (b) Real photos of PE tubes containing different pure PA chromophores (e.g., fresh chicken blood, GPD probe, GNC, Dye680 and DI water).

4.12.4 Detection of protease activity in solution

The specific enzymatic cleavage of the GPD probe was tested in solution by optical absorption testing, fluorescence emission testing, zeta potential testing and multispectral PAI testing at two representative wavelengths. The experiment was conducted with three parallel groups: 1) GPD probe incubated with protease MMP-2; 2) GPD probe incubated with protease MMP-2 and inhibitor; and 3) pure GPD probe as a control. **Figure 13.(a)** shows the proposed activation mechanism of the GPD probe. **Figure 13.(b)** shows a clear decrease in optical absorption at 680 nm for the GPD probe upon incubation with protease and washing by centrifuge, which suggested that the protease induced peptide cleavage and the release of Dye680 molecules. In contrast, no obvious change was observed in the presence of protease inhibitor, indicating that enzymatic cleavage was inhibited by the inhibitor. The fluorescence emission spectra of the three groups are shown in **Figure 13.(c)**. There was a clear increase in fluorescence from the GPD probe upon incubation with protease due to the recovery of the quenched fluorescence signal from the released Dye680 molecules. In contrast, in the presence of protease inhibitor, no change in fluorescence amplitude could be detected. In addition, the zeta potentials of nanoparticles, including GNCs, PEGylated GNCs (GNC-PEG-NH_2), substrate-conjugated GNCs (GNC-PEG-peptide), GPD probe (GNC-PEG-peptide-Dye680) and GPD probe incubated with protease, were obtained as shown in **Figure 13.(d)**. The zeta potential of PEGylated GNCs (+23.3 mV) was significantly higher than that of GNCs due to the positively charged amine group. After conjugation with the peptide substrate, a higher positive zeta potential (+37.3 mV) was obtained due to the remaining N-terminus from the peptide substrate and the unconjugated amine group from PEG. The zeta potential then decreased to (+14.2 mV) after conjugation with Dye680. Interestingly, a dramatic decrease occurred upon protease incubation. Lastly, nanoparticle-containing tubes were imaged by multispectral PAI at the representative wavelengths, as shown in **Figure 13.(e)**. Compared with the pure GPD probe, there an obvious decrease in the PA signal at 680 nm occurred upon incubation with MMP-2 and washing by centrifuge. In contrast, in the presence of MMP inhibitor, no obvious PA signal change was observed. To summarize, the optical absorption test, fluorescence emission test, zeta potential test and multispectral PAI test all confirmed the specific detection of protease MMP-2 by the GPD probe in solution.

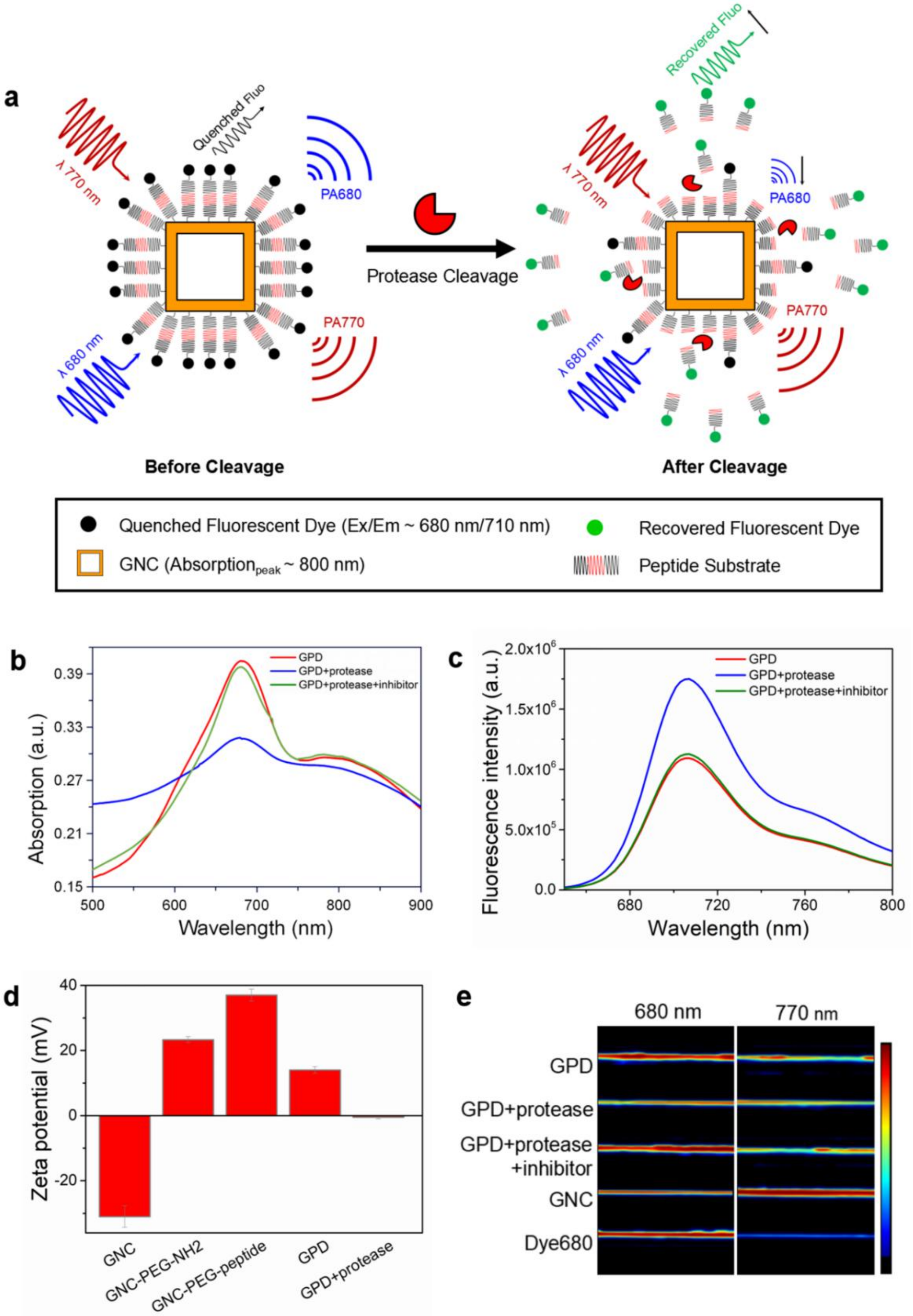

Figure 4.13. Detection of protease activity in solution. (a) Proposed probe activation mechanism. (b) UV-Vis optical absorption spectra of pure GPD probe, GPD probe incubated with protease (after washing by centrifuge), and GPD probe incubated with protease MMP-2 and inhibitor (after washing by centrifuge). (c) Fluorescence emission spectra of pure GPD probe, GPD probe incubated with protease (without washing by centrifuge), and GPD probe incubated with protease MMP-2 and inhibitor (without washing by centrifuge). (d) Zeta potential changes for the GNCs, PEGylated GNCs (GNCs-PEG-NH_2), peptide substrate-conjugated GNCs (GNCs-PEG-peptide), GPD probe (GNC-PEG-peptide-Dye680) and GPD probe incubated with protease (after washing by centrifuge). (e) Multispectral PAI at representative wavelengths of pure GPD probe, GPD probe incubated with protease (after washing by centrifuge), GPD probe incubated with protease and inhibitor (after washing by centrifuge), GNC, and Dye680 in tubes.

4.12.5 Detection of protease activity in live cells

The enzymatic cleavage of the GPD probe was further tested in typical live cell culture conditions. Two cell lines were selected, U-87 MG for high MMP-2 expression and MS1 for low MMP-2 expression [135]. Both cells were incubated in similar conditions with 0.8 μM Dye680 equivalent of GPD probe for 3 hr in the absence or presence of 10 μM MMP inhibitor. **Figure 14.(a)** shows a significant increase in the intracellular fluorescence signal when U-87 MG cells were incubated with the GPD probe and a much lower fluorescence signal in the presence of protease inhibitor. In contrast, no such apparent fluorescence signal difference was observed in MS1 cells, as shown in **Figure 14.(b)**. The results indicated that specific cleavage of the GPD probe was induced by MMP-2 in live cells, as confirmed by the previous results in solution phase.

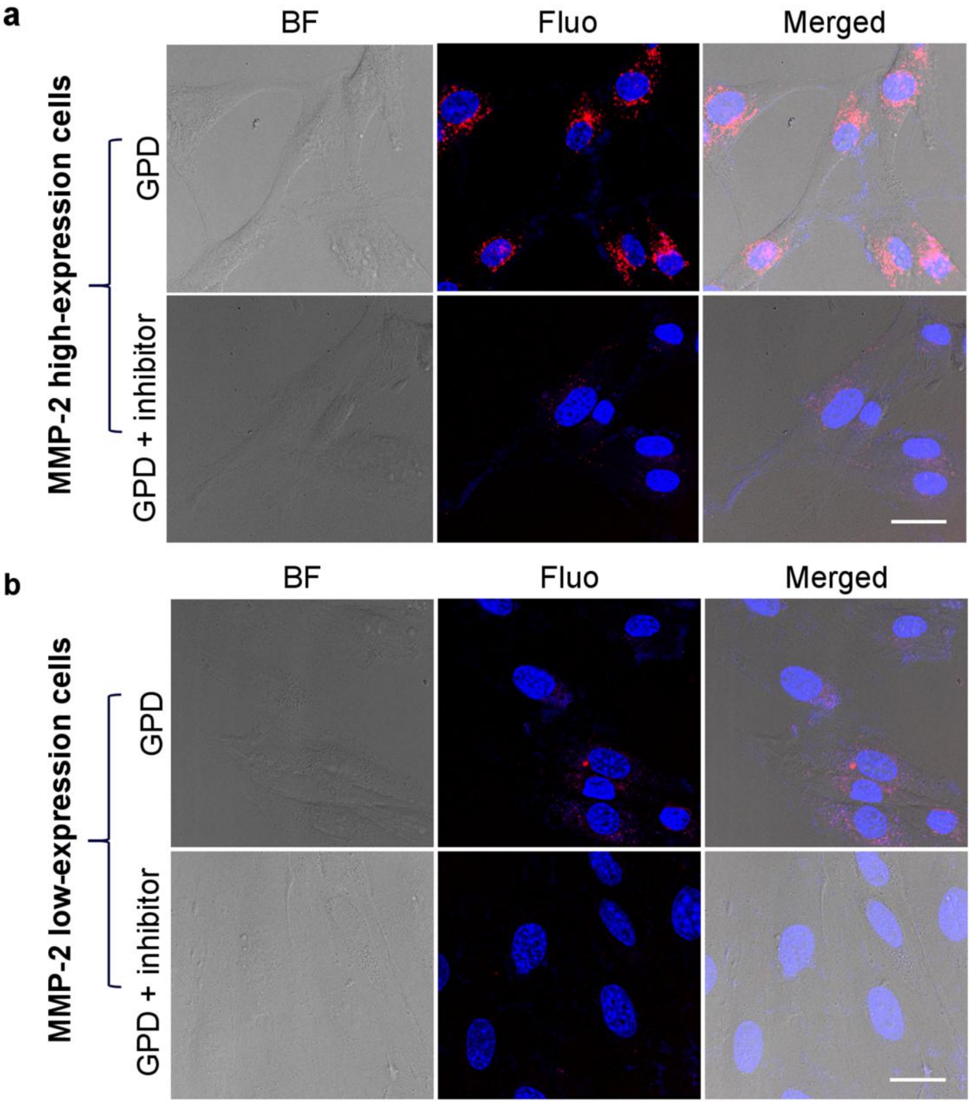

Figure 4.14. Detection of protease activity in live cells by confocal fluorescence microscopy. (a) Cell line with high expression of protease MMP-2 (U-87 MG); and (b) cell line with low expression of protease MMP-2 (MS1); both types of cells were incubated with GPD probe in the presence and absence of protease inhibitor. The fluorescence signals were from the fluorescent dye Alexa Fluor 680. Ex/Em = 683 nm/690-740 nm. Scale bar = 25 μm. (BF represents bright field imaging; Fluo

represents fluorescence imaging; Merged represents fluorescence imaging coregistered with bright field imaging)

4.12.6 *In vivo* PAI of protease activity

A human glioblastoma U-87 MG subcutaneous xenograft tumor model was established on nude mice, which has been extensively documented to show high levels of protease MMP-2 expression [138].

First, animal experiments were performed with intratumoral administration of the following four groups of contrast agents: 1) Dye680, 2) GNCs, 3) GPD probe and 4) protease inhibitor in prior and the GPD probe. The four groups of tumors were imaged by multispectral PAI at two representative wavelengths at different time points. As shown in **Figure 15.(a)**, immediately after injection, tumors treated with pure Dye680 exhibited a very strong PA signal at 680 nm, which rapidly diminished in the next 2 hr. In contrast, tumors treated with pure GNCs exhibited a high PA signal at 770 nm, which remained at a nearly constant amplitude level for 24 hr. In tumors treated with pure GPD probe, as shown in **Figure 15.(b)**, strong PA signals at both 680 nm and 770 nm appeared immediately after injection. Notably, the PA signal at 680 nm showed no obvious changes in the first 2 hr but dramatically decreased at later time points, while the PA signal at 770 nm showed no obvious decrease within 24 hr. To confirm that the decrease in the PA signal at 680 nm excitation in the tumors treated with the pure GPD probe was induced by protease MMP-2, an MMP inhibitor was injected into another group of tumors 30 min prior to the injection of the GPD probe. As expected, no obvious changes in the PA signals at either 680 nm or

770 nm were observed within 24 hr post injection. The PA amplitude changes of the tumors in group 1) and group 2) are given in **Figure 15.(c1)**. Finally, the ratios of the incremental changes in PA amplitude at 680 nm and 770 nm in group 3) and group 4) are shown in **Figure 15.(c2)**. In summary, the intratumoral administration experiment confirmed the specific enzymatic cleavage of the GPD probe and the different retention times of GNCs and Dye680 molecules inside tumors *in vivo*. Significantly, the direct intratumoral injection helped to localize the activation sites of the GPD probe solely within the tumor and provide insight into the protease activity *in vivo*.

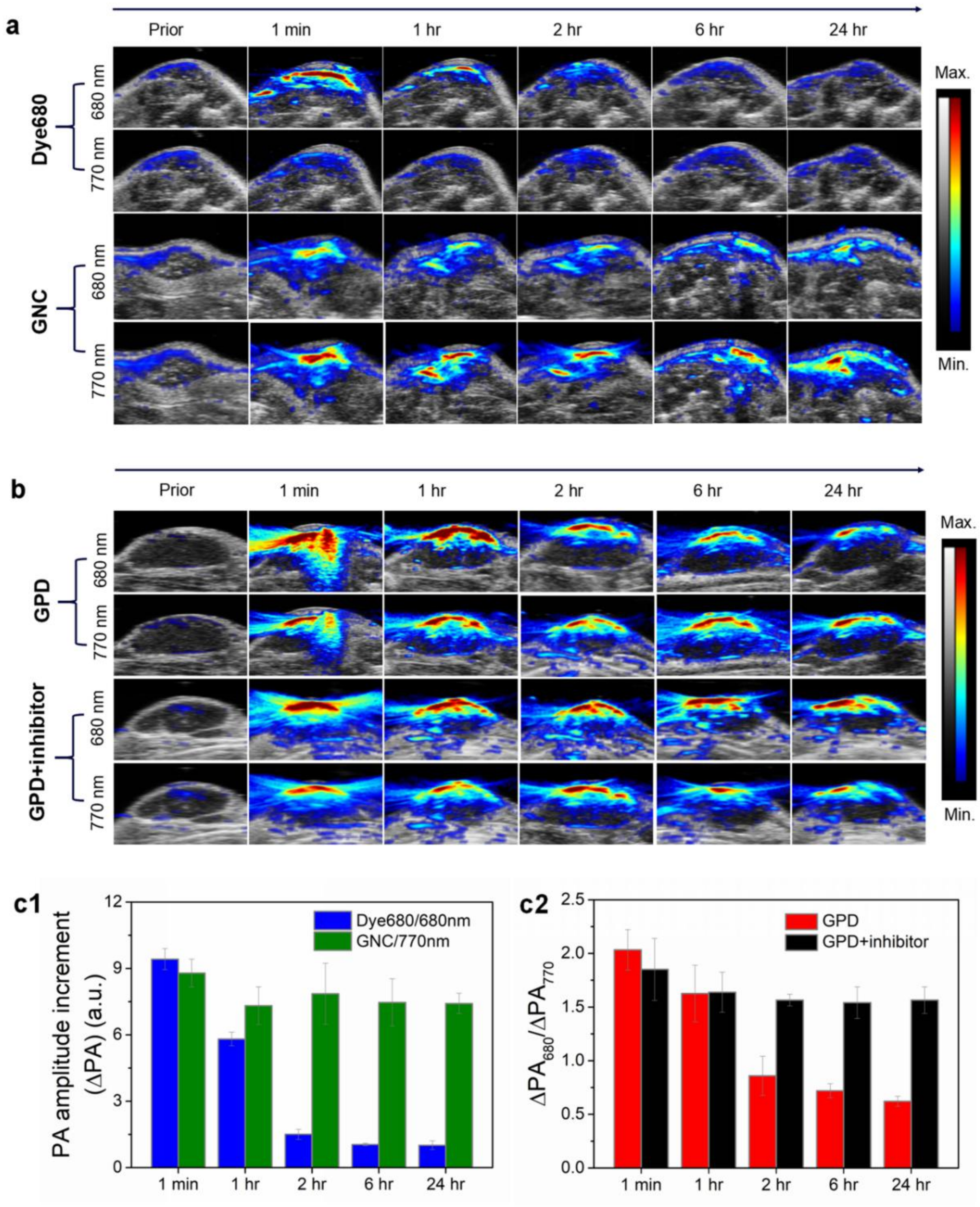

Figure 4.15. Intratumoral administration of the GPD probe by multispectral PAI at two representative wavelengths. (a) PAI of tumors after intratumoral injections of pure Dye680 and pure GNCs. (b) PAI of tumors after intratumoral injections of GPD probe in the presence and absence of MMPs inhibitor. (c1) PA amplitude increase (a.u) inside tumor after intratumoral injection of pure Dye680 at 680 nm and pure GNCs at 770 nm; (c2) Ratios of PA amplitude increase at 680 nm and 770 nm after

intratumoral injection of the GPD probe in the absence and presence of MMP inhibitor. $\Delta PA_{680}/\Delta PA_{770} = (PA_{680\,postinjection} - PA_{680\,preinjection})/(PA_{770\,postinjection} - PA_{770\,preinjection})$. Error bars are based on the standard deviations of 3-4 mice per group.

Moreover, a group of animal experiments were conducted *via* tail vein injection of the GPD probe. Since multispectral PAI at two representative wavelengths can not differentiate the signal compositions of PA signal (e.g., uncleaved GPD probe, cleaved GPD probe, HbO_2 and Hb), multispectral PAI at multiple wavelengths was applied to unmix the PA signal compositions. In contrast to the intratumoral administration experiment, no obvious multispectral PA signals from the GPD probe were observed in the tumor region immediately after the intravascular injection of the GPD probe. A clear multispectral PA signal (green) from the uncleaved GPD probe appeared ~30 min post injection, as shown in **Figure 16.(a)**. Afterward, the PA signal from the uncleaved GPD probe exhibited an initial increase and a later decrease, while that from the cleaved GPD probe increased steadily. The early increase in the PA signal from the uncleaved GPD probe suggested its continuous accumulation in the tumor. As higher levels of the GPD probe accumulated and more GPD was cleaved by the protease MMP-2, higher levels of cleaved GPD probe was retained at the cleavage site inside the tumor. On the other hand, because the released Dye680 molecules were cleared away from the tumor much more quickly, as confirmed by the intratumoral administration experiment, no multispectral PA signal could be detected from Dye680. Finally, the multispectral PAI at the two representative wavelengths was processed and quantified and is shown in **Figure 16.(b)** and **Figure 16.(c)**, confirming that the findings regarding the specific enzymatic cleavage and unique retention process of the GPD probe inside the tumor were similar to those of the previous intratumoral administration experiment.

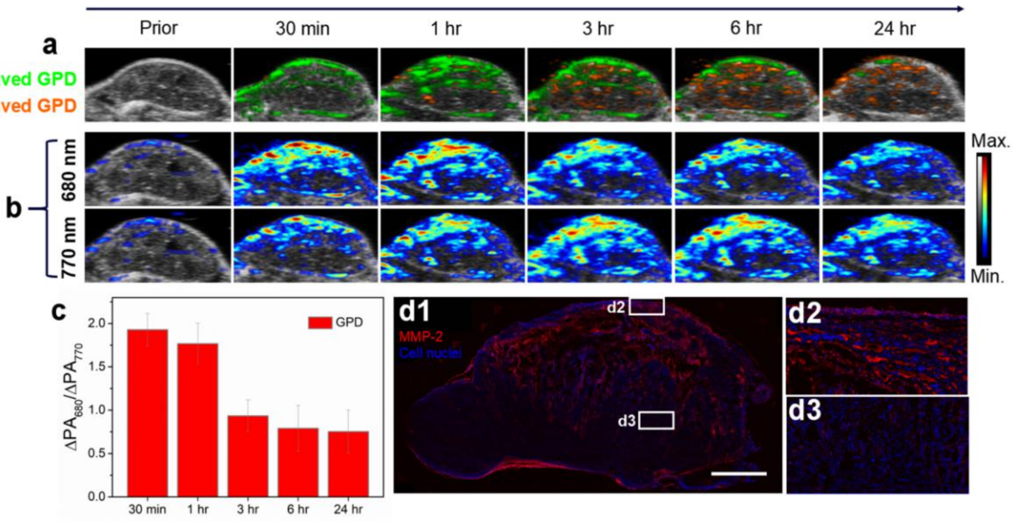

Figure 4.16. Intravascular administration of the GPD probe monitored by multispectral PAI. (a) Multispectral PAI of tumor after intravascular injection of GPD probe to estimate the PA signal composites: uncleaved GPD probe in green; cleaved GPD probe in gold; ultrasound imaging in B/W. (b) Multispectral PAI of tumor at two representative wavelengths (680 nm and 770 nm) after intravascular injection of GPD probe. (c) Ratio of PA amplitude increase inside tumor at 680 nm and 770 nm after intravascular injection of the GPD probe. $\Delta PA_{680}/\Delta PA_{770} = (PA_{680\,postinjection} - PA_{680\,preinjection})/(PA_{770\,postinjection} - PA_{770\,preinjection})$. Error bars are based on the standard deviations of 3-4 mice. (d1) *Ex vivo* immunohistochemistry (IHC) analysis (epi-fluorescence imaging) of a cryosection slice from a U-87 MG xenograft tumor specimen, the overall image; (d2) a detailed view of a region with relatively high expression level of MMP-2; (d3) a detailed view of a region with

relatively low expression level of MMP-2. MMP-2 staining (red), cell nucleus staining (blue). Scale bar = 2 mm.

Our *in vivo* results confirmed previous findings reported in the literature that activatable probes have such a "cleavage and retention" mechanism inside tumors, making them a promising approach for the *in vivo* imaging of protease activity in the TME [139, 140]. Upon cleavage, larger nanoparticles would remain in the tumor tissue much longer period than small nanoparticles, which would be quickly cleared after intravascular administration. In addition, our *in vivo* results demonstrated the ability of the synergy of the multispectral PAI and the GNC-based activatable probe to visualize and estimate the distribution of the protease activity *in vivo*. For tail vein injection experiment, the multispectral PAI was useful as a non-invasive visualization tool to estimate the probe accumulation and protease activity cleavage sites inside the tumor. The intratumoral experiment not only confined the probe to the tumor region to eliminate possible non-specific cleavage elsewhere but also prolonged its retention, allowing more interaction time for the enzymatic cleavage of the GPD probe to occur. Furthermore, to validate that the PA contrast change in the tumor region was principally due to existing protease MMP-2, tumor tissues were excised and subjected to immunohistochemistry (IHC) analysis after the *in vivo* experiment. The IHC results revealed elevated MMP-2 expression in some regions inside the tumor, as shown in **Figure 16.(d1)** and **Figure 16.(d2),** and relatively low expression level of MMP-2, as shown in **Figure 16.(d3)**, which were roughly co-localized with the results visualized and estimated by the multispectral PAI and the GNC-based activatable probe. This molecular PAI strategy exhibited markedly superior imaging contrast owing to its unique PA contrast generation mechanism. More future work is still necessary to explore the precise interpretation of the cleavage process involving the GPD probe and protease *in vivo.*

4.13 Discussion and conclusions

In this chapter, we systematically discussed the application of GNC-based cleavable nanoprobe to image dynamic proteolytic activity *in vivo* by spectroscopic photoacoustic imaging, potentially to discover the spatio-temporal alterations of the tumor proteolytic activity on a xenograft tumor model *in vivo*. Here, we firstly designed, synthesized GNC-based protease activatable PAI probe (GNC800-peptide-Alexa680). And, the unique feature of the novel nanoprobe including particle size, morphology, surface charge, optical absorption spectra, photoacoustic spectra were systematically tested. Then, the activatable ability of the nanoprobe was tested in solution-environment, cell-environment and subcutaneous tumor model (both intratumoral & intravascular administration). Finally, the protease activity was quantitatively assessed and visualized by molecular PAI *in vivo*. The results provide valuable evidences for further development and application of such novel class of GNC-based photoacoustic probe for evaluation of protease activity *in vivo.*

The basic assumption of this activatable PA probe strategy is that the retention period of gold nanocages (GNCs) with 30-50 nm in live tumor tissue is much longer than small fluorescent dye molecules, which could be cleared out from the tumor tissue quickly. In order to validate the probe design, MMP-2 high expression tumor models were first administered *via* intratumoral injection of pure Dye680 and pure GNCs, and followed by PAI assessment. Right after injection, tumor with injected

Dye680 did exhibit enhanced PA contrast at 680 nm. While, it rapidly decreased in a few hours. In contrast, pure GNCs treated tumors kept a relevantly constant PA contrast at 770 nm for a much longer period of time. After that, tumor models were validated by using activatable GPD probe in the presence and absence of MMPs inhibitor *via* intratumoral administration. After injection of GPD probe without MMPs inhibitor, strong PA contrast enhancement at both 680 nm and 770 nm did show up in the tumor region. The PA contrast change at 680 nm was not obvious in the first 2 hours; while, it decreased quickly since 2 hours post injection of GPD probe because the protease cleavage of the GPD probe within tumor tissue along with the clearance process of released Dye680 molecules both contributed to the PA signal changes *in vivo*. In contrast, after inhibited by MMPs inhibitor, within the tumor tissue, there was no significant change of PA signals at both 680 nm and 770 nm within 24 hours post intratumoral injection of GPD probe. It confirmed that the GPD protease activatable PA probe could be cleaved within tumor tissue by MMP-2 specifically.

The protease MMP-2 in the work is a well studied member in the matrix metalloproteinase (MMPs) family. In preliminary work, MMP-2 was demonstrated to be highly expressed in U-87 MG tumors. In recent study, Gambhir and colleague used photoacoustic probe for dual-wavelength PAI and ratiometric quantification. And it was used to assess the enzyme activity in follicular thyroid carcinoma. Since non-specific cleavage was possible to occur in vasculature rather than the MMP cleavage in tumor tissue for probes. And the non-specific cleavage, such as in blood plasma, might also lead to reduced signal specificity. The intratumoral administration of tumor with GPD probe gave insight into the behaviour of Dye680 cleaved from the GPD probe. The intratumoral administration procedure could minimize any possible non-specific cleavage.

At present, the photoacoustic imaging and molecular photoacoustic imaging are still in the phase of research and pre-clinical trials. Potential clinical translation fields include those are currently being explored by ultrasound imaging but still have some limitations (e.g., breast cancer and thyroid cancer). There are some challenging issues to be fully explored before the molecular photoacoustic imaging could be translated into clinical applications. The first limitation is the imaging depth of penetration because the PAI is also limited by the penetration depth of light into biological tissues. The penetration depth of PAI at around 5-7 cm would limit the its application to regional focal regions instead of whole body scanning. While, it is quite possible to combine PA instruments with endoscopic ultrasound and conventional optical endoscope so as to look into the diseases within endoscopic lumen. At present, there are still no approved PAI system for clinic use yet. The other limitation for molecular PAI is the contrast agents. PAI contrast agents with low toxicity are desired for further translation into clinic. However, most of the PAI contrast agents are still being investigated in animal models for validation and research purpose. In the future, PAI contrast agents with low biological side-effect and high imaging performance are to be explored [141].

CHAPTER 5 CONCLUSIONS AND FUTURE WORK

From the perspective of research, the theranostic values of acoustic and photoacoustic molecular imaging for oncology is quite promising. On one hand, molecualr ultrasound with targeted microbubbles is suitable for assessing the progression of tumor by visualization of those pro-angiogenic biomarkers which are expressed on the surface of endothelial cells (vasculature wall) because the current mainstream micron-size microbubbles for molecular ultrasound imaging can not go beyond the vessel wall. On the other hand, it is quite possible to develop new types of ultrasound contrast agents for extravascular biomarkers. Feasible solutions may include designing acoustic contrast agent with changeable sizes. In physical nature, photoacoustic imaging, which is based on “light-in & acoustic out” contrast mechanism, is inherently more competent in providing functional level information due to its inherent ability to acquire optical absorption characteristics from endogenous biological chromophores of interest. Furthermore, when aided by exogenous contrast agents which are mostly in nanometer size, the ability of photoacoustic imaging could be extended to molecular level conveniently. With the development of nanoprobe, the application scope of molecualr photoacoustic imaging could be either intravascular or extravascular. Note-worthily, the technique of spectroscopic photoacoustic imaging is developing towards unmixing different chromophores in actual biological environment. This technology combined with paired novel contrast agent is quite promising because the contrast-to-background ratio and contrast-to-noise ratio could be improved a lot. As a result, the imaging ability of the molecular photoacoustic imaging could be further exploited towards deeper penetration, lower dosage, higher image contrast which would be accompanied by more biomedical applications in the future. In our work, the activatable smart probe idea was employed to visualize the proteolytic activity *in vivo* instead of using simple targeting strategy to assess the expression amount of protease *in vivo*. In most cases, the functions of protease in tumor microenvironment are not a simple "expression level" question, but it is highly associated with other regulators in the complicated tumor microenvironment. Although the marriage of photoacoustic imaging and activatable contrast agent is only in the phase of start-up, we still believe that this would be one valuable strategy for visualization of the dynamic activity in tumor microenvironment. In our thesis, we only have limited time to take MMP-2 as one example of the proteolytic activity to validate the strategy of molecualr photoacoustic imaging with novel activatable contrast agent *in vivo*.

From the perspective of clinical translation, acoustic and photoacoustic molecular imaging have shown much potential for application in oncology area, not matter as diagnosis-driven solution or therapeutics-driven solution, no doubtly, both of them could be developed for pre-clinical translation. At present, certain types of targeted microbubbles for several specific biomarkers on certain cancer types have already been moved to the phase of clinical test on human beings already. And its scope in clinical practice is yet to be fully determined. One unique advantage for acoustic and photoacoustic imaging is that the two imaging modalities are born to be able to be combined in one dual-mode modality since the acoustic receiver of the two tools could share with each other technically. This advantage would greatly help to minimize the size of the imaging modality, which is quite valuable some applications, such as endoscopic practice and portable modality. The inherent dual-modal uniqueness of acoustic and photoacoustic molecular imaging would be further enlarged by developing paired contrast agent, such as dual-contrast in one system. The ideal realization of multi-modality imaging with multi-contrast agent is quite promising regarding clinical practice in the future. One day, the idea of "theranostics" would possibly improve the practices of clinical applications.

FIGURE REFERENCES

Figure 1.1. The most common cancer types in the world. (Adapted from [1])

Figure 1.2. Six hallmarks of cancer. (Adapted from [3])

Figure 2.1. The typical development of a molecular imaging strategy. (Adapted from [26])

Figure 2.2. Comprehensive preclinical and clinical molecular imaging modalities. (Adapted from [26])

Figure 3.1. Molecular ultrasound imaging for neovasculature assessment.

Figure 3.2. Two types of MBs were prepared: 1) CD105-targeted MBs as MBs-biotin-avadin-biotin-anti-CD105-FITC; 2) control non-targeted MBs as MBs-biotin-avadin-biotin-IgG. The 2nd antibody-fluorescent dye (FITC) was used to confirm the affinity of the primary antibody on the shell of MBs. Immunoglobulin G antibodies (IgG) was used as the control antibodies for non-targeted MBs.

Figure 3.3. Procedures of preparation of non-targeted MBs.

Figure 3.4. (a) Parallel flow chamber test set up; (b) flowing MBs targeting to endothelial cells. The cells were coated on the bottom of petri dish, while the MBs would flow through the chamber as the red arrow shows. Two types of cell lines (MS1, 4T1) were used as positive an negative CD105 expressing cell lines. CD105-targeted MBs and non-targeted MBs would be used to test the attachment specificity

to the positive and negative cell lines in the absence and presence of blocking antibodies.

Figure 3.5. Experiment design of *in vivo* experiment. Subcutaneous glioblastoma tumor xenograft was established for assessment of CD105 expression levels by molecular ultrasound imaging. Non-targeted MBs were injected and measured as the control, and CD105-targeted MBs were injected with 40 mins interval after the injection of non-targeted MBs. The imaging signal from CD105-targeted MBs would be calculated by averaging pre-destruction and post-destruction imaging signals and subtracting the post-destruction signal average from the pre-destruction signal average.

Figure 3.6. Principal of quantitative assessment of molecular ultrasound signals. (a) Burst and replenishment technique for quantitative assessment of the attached MBs on vessel wall. (b) Differential Targeted Enhancement (dTE) would be used to indicate the molecular signal which is contributed by attached MBs. Non-targeted MBs were used as a reference for CD105-targeted MBs.

Figure 3.7. *In vitro* characterization of CD105-targeted MBs (MBs-biotin-avadin-biotin-anti-CD105-FITC). (a) dark field microscope image; (b) fluorescence microscope imaging; (c) size distribution of MBs, mean diameter in 2-3 μm; (d) photograph of prepared MBs kept in vials.

Figure 3.8. Parallel flow chamber test results. (a) Dark field microscope images of parallel flow chamber test. Two types of cell lines were used: endothelial cell MS1 with CD105 positive expression, and 4T1 cells with CD105 negative expression. CD105-targeted MBs and non-targeted MBs were used as control, while anti-CD105 monoclonal antibody was used as blocking control in CD105 positive expressing cells.

Red arrow indicates the location of attached MBs. The round small spots under bright-field microscopy were MBs that were in contact with the membrane of cells without free floating movement. (b) Quantitative attachment results of parallel flow chamber test. Attachment number of MBs per cell. Attachment of control MBs to MS1 cells was significantly (P = .025) lower in comparison with CD105-targeted MBs; MS1 cells (CD105 positive) with blocking treatment would result in a significant (P = .015) reduction in the attachment number of CD105-targeted MBs, which could confirm the attachment specificity of the CD105-targeted MBs to the specific biomarker in the parallel flow chamber tests.

Figure 3.9. *In vivo* molecular ultrasound animal tumor model experiment set-up.

Figure 3.10. Destruction and replenishment curve of injected MBs in tumor area in subcutaneous tumor model. After the high energy burst, the MBs were destroyed and quickly replenished to the tumor area via the vasculature. The gap between the curve before and after the burst could represent the contribution from targeted MBs on the endothelial wall of blood vessels which was due to the binding to CD105.

Figure 3.11. *In vivo* assessment of CD105 expression levels in subcutaneous glioblastoma tumor xenograft in small, medium and large size. (a) Dual-mode imaging (B mode & contrast mode) of tumors with CD105-targeted MBs, scale bar = 1 mm; (b) *ex vivo* immunohistochemistry (IHC) test (CD105 and CD31) of tumor tissues. CD105 was confirmed to be expressed on endothelial cells. (c) Differential Targeted Enhancement (dTE) measured in small, medium and large glioblastoma tumor groups by using CD105-targeted MB and non-targeted MBs. (d) quantification of the expression levels of CD105 & CD31 in tumor tissues by *ex vivo* immunohistochemistry (IHC) in small, medium and large glioblastoma tumor groups.

Statistical results indicated that the expression levels of endoglin (CD105) in small and medium size tumors were significantly higher ($P < .032$) in comparison with CD31. And, in large size tumors, expression level of endoglin (CD105) was significantly lower ($P < .023$) than CD31.

Figure 4.1. Design of activatable GNC-based nanoprobe for molecular photoacoustic imaging of enzyme *in vivo.*

Figure 4.2. Chemical structure of the MMP-2 enzymatic peptide substrate(NH_2-GKG*PL**GV**R*GC-NH_2) (> 95% purity, Bankpeptide Biological Technology, Hefei, China), which possesses a cleavage site between Gly and Val, as indicated by bold italics.^{40}

Figure 4.3. The linear relationship between the optical absorption amplitude and the concentration of GNCs at the absorption peak wavelength (λ_{ab} = 800 nm).

Figure 4.4. The experimental setup for multispectral PAI of nanoparticles in PE tubes using a Vevo2100 LAZR System.

Figure 4.5. PA images at multiple wavelengths are used to unmix specific chromophore composites by relying on distinct PA spectral signatures.

Figure 4.6. *In vivo* multispectral PAI was conducted on a xenograft tumor model using a Vevo2100 LAZR System. (a) *In vivo* PA imaging experiment setup; (b) PA imaging cross section plane of the subcutaneous tumor on nude mouse; (c) freshly excised tumor specimen.

Figure 4.7. Schematic design of the activatable GPD probe . Before activation, the GPD probe was expected to produce a strong PA signal with contributions from the

GNCs with an LSPR absorption peak at ~800 nm and from the fluorescent dye Alexa Fluor 680 with an absorption peak at ~680 nm, conjugated by a specific peptide substrate (cleavable by MMP-2). The as-prepared GPD probe showed two characteristic PA spectrum peaks at 680 nm and 770 nm, which were close to the optical absorption spectrum peaks. The PA signal changes at 680 nm and 770 nm in multispectral PAI were selected to represent the chromophore composite changes within the GPD probe. In addition, the fluorescence quenching effect between the GNCs and the Dye680 molecules was used to test the synthesis of the GPD probe.

Figure 4.8. Dynamic light scattering size distribution of GNCs.

Figure 4.9. Dynamic light scattering size distribution of GPD probe.

Figure 4.10. Cell cytotoxicity of GPD probe to U-87 MG cells (n = 5, $^*p < 0.05$). No significant cytotoxicity to U-87 MG cells after incubation with the GPD probe for 24 hr at 37°C.

Figure 4.11. Preparation and characterization of the as-prepared GPD probe. (a1) TEM image of GPD probe (scale bar = 50 nm) and (a2) high-resolution TEM image (scale bar = 10 nm). Size distribution of the GPD probe: (b1) outer diameter and (b2) inner diameter of GPD probe. (c) UV-Vis absorption spectra of GPD probe, GNCs and Dye680. (d) Fluorescence emission spectra of GPD probe and Dye680 (λ_{ex} 710 nm) (at the same concentration as the Dye680 molecules attached to the GPD probe). (e1) PA spectral signatures of GPD probe, GNCs and Dye680; (e2) the linear relationship between the PA amplitude and the concentration of the GPD probe at the two representative wavelengths of multispectral PAI.

Figure 4.12. The validation of the multispectral PAI technique in solution. (a) multispectral PA imaging (3D volumetric scanning) was tested to differentiate PA chromophore composites in PE tubes (e.g., fresh chicken blood, GPD probe, GNC, Dye680 and DI water). (b) Real photos of PE tubes containing different pure PA chromophores (e.g., fresh chicken blood, GPD probe, GNC, Dye680 and DI water).

Figure 4.13. Detection of protease activity in solution. (a) Proposed probe activation mechanism. (b) UV-Vis optical absorption spectra of pure GPD probe, GPD probe incubated with protease (after washing by centrifuge), and GPD probe incubated with protease MMP-2 and inhibitor (after washing by centrifuge). (c) Fluorescence emission spectra of pure GPD probe, GPD probe incubated with protease (without washing by centrifuge), and GPD probe incubated with protease MMP-2 and inhibitor (without washing by centrifuge). (d) Zeta potential changes for the GNCs, PEGylated GNCs (GNCs-PEG-NH_2), peptide substrate-conjugated GNCs (GNCs-PEG-peptide), GPD probe (GNC-PEG-peptide-Dye680) and GPD probe incubated with protease (after washing by centrifuge). (e) Multispectral PAI at representative wavelengths of pure GPD probe, GPD probe incubated with protease (after washing by centrifuge), GPD probe incubated with protease and inhibitor (after washing by centrifuge), GNC, and Dye680 in tubes.

Figure 4.14. Detection of protease activity in live cells by confocal fluorescence microscopy. (a) Cell line with high expression of protease MMP-2 (U-87 MG); and (b) cell line with low expression of protease MMP-2 (MS1); both types of cells were incubated with GPD probe in the presence and absence of protease inhibitor. The fluorescence signals were from the fluorescent dye Alexa Fluor 680. Ex/Em = 683 nm/690-740 nm. Scale bar = 25 m. (BF represents bright field imaging; Fluo

represents fluorescence imaging; Merged represents fluorescence imaging coregistered with bright field imaging)

Figure 4.15. Intratumoral administration of the GPD probe by multispectral PAI at two representative wavelengths. (a) PAI of tumors after intratumoral injections of pure Dye680 and pure GNCs. (b) PAI of tumors after intratumoral injections of GPD probe in the presence and absence of MMPs inhibitor. (c1) PA amplitude increase (a.u) inside tumor after intratumoral injection of pure Dye680 at 680 nm and pure GNCs at 770 nm; (c2) Ratios of PA amplitude increase at 680 nm and 770 nm after intratumoral injection of the GPD probe in the absence and presence of MMP inhibitor. $\Delta PA_{680}/\Delta PA_{770} = (PA_{680\,postinjecton} - PA_{680\,preinjection})/(PA_{770\,postinjecton} - PA_{770\,preinjection})$. Error bars are based on the standard deviations of 3-4 mice per group.

Figure 4.16. Intravascular administration of the GPD probe monitored by multispectral PAI. (a) Multispectral PAI of tumor after intravascular injection of GPD probe to estimate the PA signal composites: uncleaved GPD probe in green; cleaved GPD probe in gold; ultrasound imaging in B/W. (b) Multispectral PAI of tumor at two representative wavelengths (680 nm and 770 nm) after intravascular injection of GPD probe. (c) Ratio of PA amplitude increase inside tumor at 680 nm and 770 nm after intravascular injection of the GPD probe. $\Delta PA_{680}/\Delta PA_{770} = (PA_{680\,postinjecton} - PA_{680\,preinjection})/(PA_{770\,postinjecton} - PA_{770\,preinjection})$. Error bars are based on the standard deviations of 3-4 mice. (d1) *Ex vivo* immunohistochemistry (IHC) analysis (epi-fluorescence imaging) of a cryosection slice from a U-87 MG xenograft tumor specimen, the overall image; (d2) a detailed view of a region with relatively high expression level of MMP-2; (d3) a detailed view of a region with

relatively low expression level of MMP-2. MMP-2 staining (red), cell nucleus staining (blue). Scale bar = 2 mm.

REFERENCES

1. R. L. Siegel, K. D. Miller, and A. Jemal, "Cancer statistics, 2016," *CA. Cancer J. Clin.,* vol. 66, no. 1, pp. 7-30, 2016.
2. P. Albertsen, "Predicting survival for men with clinically localized prostate cancer," *Cancer,* vol. 112, no. 1, pp. 1-3, 2008.
3. D. Hanahan, and R. A. Weinberg, "Hallmarks of cancer: the next generation," *Cell,* vol. 144, no. 5, pp. 646-674, 2011.
4. D. F. Quail, and J. A. Joyce, "Microenvironmental regulation of tumor progression and metastasis," *Nat. Med.,* vol. 19, no. 11, pp. 1423-1437, 2013.
5. D. Hanahan, and R. A. Weinberg, "The hallmarks of cancer," *Cell,* vol. 100, no. 1, pp. 57-70, 2000.
6. M. A. Lemmon, and J. Schlessinger, "Cell signaling by receptor tyrosine kinases," *Cell,* vol. 141, no. 7, pp. 1117-1134, 2010.
7. D. L. Burkhart, and J. Sage, "Cellular mechanisms of tumour suppression by the retinoblastoma gene," *Nat. Rev. Cancer,* vol. 8, no. 9, pp. 671, 2008.
8. J. Adams, and S. Cory, "The Bcl-2 apoptotic switch in cancer development and therapy," *Oncogene,* vol. 26, no. 9, pp. 1324, 2007.
9. M. R. Junttila, and G. I. Evan, "p53—a Jack of all trades but master of none," *Nat. Rev. Cancer,* vol. 9, no. 11, pp. 821, 2009.
10. M. A. Blasco, "Telomeres and human disease: ageing, cancer and beyond," *Nat. Rev. Genet.,* vol. 6, no. 8, pp. 611, 2005.

11. J. E. Talmadge, and I. J. Fidler, “AACR centennial series: the biology of cancer metastasis: historical perspective,” *Cancer Res.,* vol. 70, no. 14, pp. 5649-5669, 2010.
12. U. Cavallaro, and G. Christofori, “Cell adhesion and signalling by cadherins and Ig-CAMs in cancer,” *Nat. Rev. Cancer,* vol. 4, no. 2, pp. 118, 2004.
13. G. Berx, and F. Van Roy, “Involvement of members of the cadherin superfamily in cancer,” *Cold Spring Harb. Perspect. Biol.,* vol. 1, no. 6, pp. a003129, 2009.
14. D. Hanahan, and J. Folkman, “Patterns and emerging mechanisms of the angiogenic switch during tumorigenesis,” *Cell,* vol. 86, no. 3, pp. 353-364, 1996.
15. V. Baeriswyl, and G. Christofori, "The angiogenic switch in carcinogenesis." pp. 329-337.
16. G. Bergers, and L. E. Benjamin, “Angiogenesis: tumorigenesis and the angiogenic switch,” *Nat. Rev. Cancer,* vol. 3, no. 6, pp. 401, 2003.
17. Z. Ahmed, and R. Bicknell, "Angiogenic signalling pathways," *Angiogenesis Protocols*, pp. 3-24: Springer, 2009.
18. P. Carmeliet, and R. K. Jain, “Angiogenesis in cancer and other diseases,” *Nature,* vol. 407, no. 6801, pp. 249, 2000.
19. T. Tammela, and K. Alitalo, “Lymphangiogenesis: Molecular mechanisms and future promise,” *Cell,* vol. 140, no. 4, pp. 460-476, 2010.
20. M. Mazzone, D. Dettori, R. L. de Oliveira, S. Loges, T. Schmidt, B. Jonckx, Y.-M. Tian, A. A. Lanahan, P. Pollard, and C. R. de Almodovar, “Heterozygous deficiency of PHD2 restores tumor oxygenation and inhibits metastasis via endothelial normalization,” *Cell,* vol. 136, no. 5, pp. 839-851, 2009.
21. R. W. Cho, X. Wang, M. Diehn, K. Shedden, G. Y. Chen, G. Sherlock, A. Gurney, J. Lewicki, and M. F. Clarke, “Isolation and molecular characterization

of cancer stem cells in MMTV-Wnt-1 murine breast tumors," *Stem Cells,* vol. 26, no. 2, pp. 364-371, 2008.

22. A. Singh, and J. Settleman, "EMT, cancer stem cells and drug resistance: an emerging axis of evil in the war on cancer," *Oncogene,* vol. 29, no. 34, pp. 4741, 2010.
23. M. F. Kircher, and J. K. Willmann, "Molecular body imaging: MR imaging, CT, and US. part I. principles," *Radiology,* vol. 263, no. 3, pp. 633-643, 2012.
24. S. J. Kennel, I. A. Davis, J. Branning, H. Pan, G. W. Kabalka, and M. J. Paulus, "High resolution computed tomography and MRI for monitoring lung tumor growth in mice undergoing radioimmunotherapy: correlation with histology," *Med. Phys.,* vol. 27, no. 5, pp. 1101-1107, 2000.
25. Z. Zhou, and Z.-R. Lu, "Molecular imaging of the tumor microenvironment," *Adv. Drug Delivery Rev.*, 2016.
26. M. L. James, and S. S. Gambhir, "A molecular imaging primer: modalities, imaging agents, and applications," *Physiol. Rev.,* vol. 92, no. 2, pp. 897-965, 2012.
27. J. J. Keyes, N. Orlandea, W. J. Heetderks, P. F. Leonard, and W. Rogers, "The Humongotron--a scintillation-camera transaxial tomograph," *Journal of nuclear medicine: official publication, Society of Nuclear Medicine,* vol. 18, no. 4, pp. 381-387, 1977.
28. J. Gaa, E. Rummeny, and M. Seemann, "Whole-body imaging with PET/MRI," *EUROPEAN JOURNAL OF MEDICAL RESEARCH.,* vol. 9, no. 6, pp. 309-312, 2004.
29. S. R. Arridge, "Optical tomography in medical imaging," *Inverse problems,* vol. 15, no. 2, pp. R41, 1999.

30. N. Deshpande, A. Needles, and J. K. Willmann, “Molecular ultrasound imaging: current status and future directions,” *Clin. Radiol.,* vol. 65, no. 7, pp. 567-581, 2010.
31. V. Amirbekian, M. J. Lipinski, K. C. Briley-Saebo, S. Amirbekian, J. G. S. Aguinaldo, D. B. Weinreb, E. Vucic, J. C. Frias, F. Hyafil, and V. Mani, “Detecting and assessing macrophages in vivo to evaluate atherosclerosis noninvasively using molecular MRI,” *Proceedings of the National Academy of Sciences,* vol. 104, no. 3, pp. 961-966, 2007.
32. M. F. Kircher, A. De La Zerda, J. V. Jokerst, C. L. Zavaleta, P. J. Kempen, E. Mittra, K. Pitter, R. Huang, C. Campos, and F. Habte, “A brain tumor molecular imaging strategy using a new triple-modality MRI-photoacoustic-Raman nanoparticle,” *Nat. Med.,* vol. 18, no. 5, pp. 829, 2012.
33. B. Cox, J. G. Laufer, S. R. Arridge, and P. C. Beard, “Quantitative spectroscopic photoacoustic imaging: a review,” *J. Biomed. Opt.,* vol. 17, no. 6, pp. 0612021-06120222, 2012.
34. L. V. Wang, “Multiscale photoacoustic microscopy and computed tomography,” *Nat. Photonics,* vol. 3, no. 9, pp. 503-509, 2009.
35. J. K. Willmann, N. Van Bruggen, L. M. Dinkelborg, and S. S. Gambhir, “Molecular imaging in drug development,” *Nat. Rev. Drug Discovery,* vol. 7, no. 7, pp. 591, 2008.
36. T. Flohr, K. Stierstorfer, H. Bruder, J. Simon, and S. Schaller, "New technical developments in multislice CT." pp. 839-845.
37. H. Hu, “Multi-slice helical CT: Scan and reconstruction,” *Med. Phys.,* vol. 26, no. 1, pp. 5-18, 1999.

38. R. Popovtzer, A. Agrawal, N. A. Kotov, A. Popovtzer, J. Balter, T. E. Carey, and R. Kopelman, "Targeted gold nanoparticles enable molecular CT imaging of cancer," *Nano Lett.,* vol. 8, no. 12, pp. 4593-4596, 2008.
39. D. Kim, Y. Y. Jeong, and S. Jon, "A drug-loaded aptamer− gold nanoparticle bioconjugate for combined CT imaging and therapy of prostate cancer," *ACS Nano,* vol. 4, no. 7, pp. 3689-3696, 2010.
40. J. Li, A. Chaudhary, S. J. Chmura, C. Pelizzari, T. Rajh, C. Wietholt, M. Kurtoglu, and B. Aydogan, "A novel functional CT contrast agent for molecular imaging of cancer," *Phys. Med. Biol.,* vol. 55, no. 15, pp. 4389, 2010.
41. H. Schlemmer, "BASIC PRINCIPLES OF MRI," *Radiother. Oncol.,* vol. 92, pp. S6, 2009.
42. R. Guzman, N. Uchida, T. M. Bliss, D. He, K. K. Christopherson, D. Stellwagen, A. Capela, J. Greve, R. C. Malenka, and M. E. Moseley, "Long-term monitoring of transplanted human neural stem cells in developmental and pathological contexts with MRI," *Proceedings of the National Academy of Sciences,* vol. 104, no. 24, pp. 10211-10216, 2007.
43. R. Hodgson, P. O'connor, and R. Moots, "MRI of rheumatoid arthritis—image quantitation for the assessment of disease activity, progression and response to therapy," *Rheumatology,* vol. 47, no. 1, pp. 13-21, 2007.
44. S. J. Kennel, I. A. Davis, J. Branning, H. Pan, G. W. Kabalka, and M. J. Paulus, "High resolution computed tomography and MRI for monitoring lung tumor growth in mice undergoing radioimmunotherapy: correlation with histology," *Med. Phys.,* vol. 27, no. 5, pp. 1101-1107, 2000.
45. A. Kumar, R. Kumar, V. Seenu, S. D. Gupta, M. Chawla, A. Malhotra, and S. N. Mehta, "The role of 18F-FDG PET/CT in evaluation of early response to

neoadjuvant chemotherapy in patients with locally advanced breast cancer," *Eur. Radiol.,* vol. 19, no. 6, pp. 1347-1357, 2009.

46. S. R. Meikle, P. Kench, M. Kassiou, and R. B. Banati, "Small animal SPECT and its place in the matrix of molecular imaging technologies," *Phys. Med. Biol.,* vol. 50, no. 22, pp. R45, 2005.
47. C. Z. Behm, and J. R. Lindner, "Cellular and molecular imaging with targeted contrast ultrasound," *Ultrasound quarterly,* vol. 22, no. 1, pp. 67-72, 2006.
48. F. Kiessling, S. Fokong, P. Koczera, W. Lederle, and T. Lammers, "Ultrasound microbubbles for molecular diagnosis, therapy, and theranostics," *J. Nucl. Med.,* vol. 53, no. 3, pp. 345-348, 2012.
49. M. A. Pysz, K. Foygel, J. Rosenberg, S. S. Gambhir, M. Schneider, and J. K. Willmann, "Antiangiogenic cancer therapy: monitoring with molecular US and a clinically translatable contrast agent (BR55)," *Radiology,* vol. 256, no. 2, pp. 519-527, 2010.
50. E. Fonsatti, H. J. Nicolay, M. Altomonte, A. Covre, and M. Maio, "Targeting cancer vasculature via endoglin/CD105: a novel antibody-based diagnostic and therapeutic strategy in solid tumours," *Cardiovasc. Res.,* vol. 86, no. 1, pp. 12-19, 2009.
51. E. Fonsatti, L. Sigalotti, P. Arslan, M. Altomonte, and M. Maio, "Emerging role of endoglin (CD105) as a marker of angiogenesis with clinical potential in human malignancies," *Curr. Cancer Drug Targets,* vol. 3, no. 6, pp. 427-432, 2003.
52. Y. Zhang, Y. Yang, H. Hong, and W. Cai, "Multimodality molecular imaging of CD105 (Endoglin) expression," *Int. J. Clin. Exp. Med.,* vol. 4, no. 1, pp. 32, 2011.
53. T. Myochin, K. Hanaoka, T. Komatsu, T. Terai, and T. Nagano, "Design strategy for a near-infrared fluorescence probe for matrix metalloproteinase utilizing

highly cell permeable boron dipyrromethene," *J. Am. Chem. Soc.,* vol. 134, no. 33, pp. 13730-13737, 2012.

54. D. Gyawali, S. Zhou, R. T. Tran, Y. Zhang, C. Liu, X. Bai, and J. Yang, "Fluorescence imaging enabled biodegradable photostable polymeric micelles," *Advanced healthcare materials,* vol. 3, no. 2, pp. 182-186, 2014.
55. D. Gyawali, J. P. Kim, and J. Yang, "Highly photostable nanogels for fluorescence-based theranostics," *Bioactive Materials*, 2017.
56. H. Yao, Y. Zhang, F. Xiao, Z. Xia, and J. Rao, "Quantum dot/bioluminescence resonance energy transfer based highly sensitive detection of proteases," *Angewandte Chemie International Edition,* vol. 46, no. 23, pp. 4346-4349, 2007.
57. A. G. Bell, "ART. XXXIV.--On the Production and Reproduction of Sound by Light," *American Journal of Science (1880-1910),* vol. 20, no. 118, pp. 305, 1880.
58. L. Nie, and X. Chen, "Structural and functional photoacoustic molecular tomography aided by emerging contrast agents," *Chem. Soc. Rev.,* vol. 43, no. 20, pp. 7132-7170, 2014.
59. C. Kim, C. Favazza, and L. V. Wang, "In vivo photoacoustic tomography of chemicals: high-resolution functional and molecular optical imaging at new depths," *Chem. Rev.,* vol. 110, no. 5, pp. 2756-2782, 2010.
60. B. Cox, J. G. Laufer, S. R. Arridge, and P. C. Beard, "Quantitative spectroscopic photoacoustic imaging: a review," *J. Biomed. Opt.,* vol. 17, no. 6, pp. 0612021-06120222, 2012.
61. J. Weber, P. C. Beard, and S. E. Bohndiek, "Contrast agents for molecular photoacoustic imaging," 2016.
62. R. Alford, M. , P. L. , and H. , "Molecular probes for the in vivo imaging of cancer," *Mol. .,* vol. 5, no. 11, pp. 1279-1291, 2009.

63. S. I. , and J. Van , “Imaging hallmarks of cancer in living mice,” *Nat. Rev. Cancer,* vol. 14, no. 6, pp. 406, 2014.
64. G. E. Weller, M. K. Wong, R. A. Modzelewski, E. Lu, A. L. Klibanov, W. R. Wagner, and F. S. Villanueva, “Ultrasonic imaging of tumor angiogenesis using contrast microbubbles targeted via the tumor-binding peptide arginine-arginine-leucine,” *Cancer Res.,* vol. 65, no. 2, pp. 533-539, 2005.
65. X. Sun, G. Niu, N. Chan, B. Shen, and X. Chen, “Tumor hypoxia imaging,” *Mol. Imaging Biol.,* vol. 13, no. 3, pp. 399-410, 2011.
66. R. Alford, M. Ogawa, P. L. Choyke, and H. Kobayashi, “Molecular probes for the in vivo imaging of cancer,” *Mol. Biosyst.,* vol. 5, no. 11, pp. 1279-1291, 2009.
67. J. Liu, W. Wang, D. T. Dicker, and W. S. El-Deiry, “Bioluminescent imaging of TRAIL-induced apoptosis through detection of caspase activation following cleavage of DEVD-aminoluciferin,” *Cancer Biol. Ther.,* vol. 4, no. 8, pp. 885-892, 2005.
68. A. Boire, L. Covic, A. Agarwal, S. Jacques, S. Sherifi, and A. Kuliopulos, “PAR1 is a matrix metalloprotease-1 receptor that promotes invasion and tumorigenesis of breast cancer cells,” *Cell,* vol. 120, no. 3, pp. 303-313, 2005.
69. Z. Ahmed, and R. Bicknell, "Angiogenic signalling pathways," *Angiogenesis Protocols*, pp. 3-24: Springer, 2009.
70. S. Das, and P. A. Marsden, “Angiogenesis in glioblastoma,” *N. Engl. J. Med.,* vol. 369, no. 16, pp. 1561-1563, 2013.
71. P. Carmeliet, and R. K. Jain, “Angiogenesis in cancer and other diseases,” *Nature,* vol. 407, no. 6801, pp. 249, 2000.
72. V. Baeriswyl, and G. Christofori, "The angiogenic switch in carcinogenesis." pp. 329-337.

73. S. E. Duff, C. Li, J. M. Garland, and S. Kumar, “CD105 is important for angiogenesis: evidence and potential applications,” *The FASEB Journal,* vol. 17, no. 9, pp. 984-992, 2003.
74. E. Fonsatti, H. J. Nicolay, M. Altomonte, A. Covre, and M. Maio, “Targeting cancer vasculature via endoglin/CD105: a novel antibody-based diagnostic and therapeutic strategy in solid tumours,” *Cardiovasc. Res.,* vol. 86, no. 1, pp. 12-19, 2009.
75. E. Fonsatti, L. Sigalotti, P. Arslan, M. Altomonte, and M. Maio, “Emerging role of endoglin (CD105) as a marker of angiogenesis with clinical potential in human malignancies,” *Curr. Cancer Drug Targets,* vol. 3, no. 6, pp. 427-432, 2003.
76. Y. Zhang, Y. Yang, H. Hong, and W. Cai, “Multimodality molecular imaging of CD105 (Endoglin) expression,” *Int. J. Clin. Exp. Med.,* vol. 4, no. 1, pp. 32, 2011.
77. M. Paauwe, P. Ten Dijke, and L. J. Hawinkels, “Endoglin for tumor imaging and targeted cancer therapy,” *Expert Opin. Ther. Targets,* vol. 17, no. 4, pp. 421-435, 2013.
78. L. S. Rosen, M. S. Gordon, F. Robert, and D. E. Matei, “Endoglin for targeted cancer treatment,” *Curr. Oncol. Rep.,* vol. 16, no. 2, pp. 365, 2014.
79. Y. Zhang, Y. Yang, H. Hong, and W. Cai, “Multimodality molecular imaging of CD105 (Endoglin) expression,” *Int. J. Clin. Exp. Med.,* vol. 4, no. 1, pp. 32, 2011.
80. S. Bredow, M. Lewin, B. Hofmann, E. Marecos, and R. Weissleder, “Imaging of tumour neovasculature by targeting the TGF-β binding receptor endoglin,” *Eur. J. Cancer,* vol. 36, no. 5, pp. 675-681, 2000.
81. D. Zhang, X.-Y. Feng, T. D. Henning, L. Wen, W.-Y. Lu, H. Pan, X. Wu, and L.-G. Zou, “MR imaging of tumor angiogenesis using sterically stabilized Gd-DTPA liposomes targeted to CD105,” *Eur. J. Radiol.,* vol. 70, no. 1, pp. 180-189, 2009.

82. N. Deshpande, A. Needles, and J. K. Willmann, "Molecular ultrasound imaging: current status and future directions," *Clin. Radiol.,* vol. 65, no. 7, pp. 567-581, 2010.
83. K. Ferrara, R. Pollard, and M. Borden, "Ultrasound microbubble contrast agents: fundamentals and application to gene and drug delivery," *Annu. Rev. Biomed. Eng.,* vol. 9, 2007.
84. G. Korpanty, J. G. Carbon, P. A. Grayburn, J. B. Fleming, and R. A. Brekken, "Monitoring response to anticancer therapy by targeting microbubbles to tumor vasculature," *Clin. Cancer Res.,* vol. 13, no. 1, pp. 323-330, 2007.
85. I. Tardy, S. Pochon, M. Theraulaz, P. Emmel, L. Passantino, F. Tranquart, and M. Schneider, "Ultrasound molecular imaging of VEGFR2 in a rat prostate tumor model using BR55," *Invest. Radiol.,* vol. 45, no. 10, pp. 573-578, 2010.
86. C. Z. Behm, and J. R. Lindner, "Cellular and molecular imaging with targeted contrast ultrasound," *Ultrasound quarterly,* vol. 22, no. 1, pp. 67-72, 2006.
87. F. Yan, X. Li, Q. Jin, J. Chen, R. Shandas, J. Wu, L. Li, T. Ling, W. Yang, and Y. Chen, "Ultrasonic imaging of endothelial CD81 expression using CD81-targeted contrast agents in in vitro and in vivo studies," *Ultrasound Med. Biol.,* vol. 38, no. 4, pp. 670-680, 2012.
88. H. Leong-Poi, J. Christiansen, A. L. Klibanov, S. Kaul, and J. R. Lindner, "Noninvasive assessment of angiogenesis by ultrasound and microbubbles targeted to α v-integrins," *Circulation,* vol. 107, no. 3, pp. 455-460, 2003.
89. M. Schneider, A. Broillet, I. Tardy, S. Pochon, P. Bussat, T. Bettinger, A. Helbert, M. Costa, and F. Tranquart, "Use of Intravital Microscopy to Study the Microvascular Behavior of Microbubble-Based Ultrasound Contrast Agents," *Microcirculation,* vol. 19, no. 3, pp. 245-259, 2012.

90. N. Deshpande, M. A. Pysz, and J. K. Willmann, “Molecular ultrasound assessment of tumor angiogenesis,” *Angiogenesis,* vol. 13, no. 2, pp. 175-188, 2010.
91. A. M. Takalkar, A. L. Klibanov, J. J. Rychak, J. R. Lindner, and K. Ley, “Binding and detachment dynamics of microbubbles targeted to P-selectin under controlled shear flow,” *J. Control. Release,* vol. 96, no. 3, pp. 473-482, 2004.
92. E. C. Unger, T. A. Fritz, T. Matsunaga, V. Ramaswami, D. Yellowhair, and G. Wu, "Method of preparing gas and gaseous precursor-filled microspheres," Google Patents, 1996.
93. A. Della Martina, E. Allemann, T. Bettinger, P. Bussat, A. Lassus, S. Pochon, and M. Schneider, “Grafting of abciximab to a microbubble-based ultrasound contrast agent for targeting to platelets expressing GP IIb/IIIa–Characterization and in vitro testing,” *Eur. J. Pharm. Biopharm.,* vol. 68, no. 3, pp. 555-564, 2008.
94. M. R. Böhmer, R. Schroeders, J. A. Steenbakkers, S. H. de Winter, P. A. Duineveld, J. Lub, W. P. Nijssen, J. A. Pikkemaat, and H. R. Stapert, “Preparation of monodisperse polymer particles and capsules by ink-jet printing,” *Colloids and Surfaces A: Physicochemical and Engineering Aspects,* vol. 289, no. 1-3, pp. 96-104, 2006.
95. P. Narayan, and M. A. Wheatley, “Preparation and characterization of hollow microcapsules for use as ultrasound contrast agents,” *Polym. Eng. Sci.,* vol. 39, no. 11, pp. 2242-2255, 1999.
96. G. E. Weller, F. S. Villanueva, E. M. Tom, and W. R. Wagner, “Targeted ultrasound contrast agents: In vitro assessment of endothelial dysfunction and multi-targeting to ICAM-1 and sialyl Lewisx,” *Biotechnol. Bioeng.,* vol. 92, no. 6, pp. 780-788, 2005.

97. F. Yan, X. Li, Q. Jin, J. Chen, R. Shandas, J. Wu, L. Li, T. Ling, W. Yang, and Y. Chen, "Ultrasonic imaging of endothelial CD81 expression using CD81-targeted contrast agents in in vitro and in vivo studies," *Ultrasound Med. Biol.,* vol. 38, no. 4, pp. 670-680, 2012.

98. A. M. Takalkar, A. L. Klibanov, J. J. Rychak, J. R. Lindner, and K. Ley, "Binding and detachment dynamics of microbubbles targeted to P-selectin under controlled shear flow," *J. Control. Release,* vol. 96, no. 3, pp. 473-482, 2004.

99. J. C. Hutter, H. Luu, P. M. Mehlhaff, A. L. Killam, and H. C. Dittrich, "Physiologically based pharmacokinetic model for fluorocarbon elimination after the administration of an octafluoropropane-albumin microsphere sonographic contrast agent," *J. Ultrasound Med.,* vol. 18, no. 1, pp. 1-11, 1999.

100. J. Å. Jakobsen, R. Oyen, H. S. Thomsen, S. K. Morcos, and M. o. C. M. S. C. o. E. S. o. U. Radiology, "Safety of ultrasound contrast agents," *Eur. Radiol.,* vol. 15, no. 5, pp. 941-945, 2005.

101. F. Piscaglia, and L. Bolondi, "The safety of Sonovue® in abdominal applications: Retrospective analysis of 23188 investigations," *Ultrasound Med. Biol.,* vol. 32, no. 9, pp. 1369-1375, 2006.

102. M. L. Main, A. C. Ryan, T. E. Davis, M. P. Albano, L. L. Kusnetzky, and M. Hibberd, "Acute mortality in hospitalized patients undergoing echocardiography with and without an ultrasound contrast agent (multicenter registry results in 4,300,966 consecutive patients)," *Am. J. Cardiol.,* vol. 102, no. 12, pp. 1742-1746, 2008.

103. J. J. Rychak, A. L. Klibanov, K. F. Ley, and J. A. Hossack, "Enhanced targeting of ultrasound contrast agents using acoustic radiation force," *Ultrasound Med. Biol.,* vol. 33, no. 7, pp. 1132-1139, 2007.

104.B. A. Kaufmann, J. M. Sanders, C. Davis, A. Xie, P. Aldred, I. J. Sarembock, and J. R. Lindner, “Molecular imaging of inflammation in atherosclerosis with targeted ultrasound detection of vascular cell adhesion molecule-1,” *Circulation,* vol. 116, no. 3, pp. 276-284, 2007.

105.D. B. Ellegala, H. Leong-Poi, J. E. Carpenter, A. L. Klibanov, S. Kaul, M. E. Shaffrey, J. Sklenar, and J. R. Lindner, “Imaging tumor angiogenesis with contrast ultrasound and microbubbles targeted to αvβ3,” *Circulation,* vol. 108, no. 3, pp. 336-341, 2003.

106.W. H. Wright Jr, T. P. McCreery, E. A. Krupinski, P. J. Lund, S. H. Smyth, M. R. Baker, R. L. Hulett, and E. C. Unger, “Evaluation of new thrombus-specific ultrasound contrast agent,” *Acad. Radiol.,* vol. 5, pp. S240-S242, 1998.

107.B. A. Kaufmann, C. Lewis, A. Xie, A. Mirza-Mohd, and J. R. Lindner, “Detection of recent myocardial ischaemia by molecular imaging of P-selectin with targeted contrast echocardiography,” *Eur. Heart J.,* vol. 28, no. 16, pp. 2011-2017, 2007.

108.D. Hanahan, and R. A. Weinberg, “Hallmarks of cancer: the next generation,” *Cell,* vol. 144, no. 5, pp. 646-674, 2011.

109.D. F. Quail, and J. A. Joyce, “Microenvironmental regulation of tumor progression and metastasis,” *Nat. Med.,* vol. 19, no. 11, pp. 1423-1437, 2013.

110.R. Lebel, and M. Lepage, “A comprehensive review on controls in molecular imaging: lessons from MMP-2 imaging,” *Contrast Media Mol. Imaging,* vol. 9, no. 3, pp. 187-210, 2014.

111.K. Kessenbrock, V. Plaks, and Z. Werb, “Matrix metalloproteinases: regulators of the tumor microenvironment,” *Cell,* vol. 141, no. 1, pp. 52-67, 2010.

112. A. Razgulin, N. Ma, and J. Rao, “Strategies for in vivo imaging of enzyme activity: an overview and recent advances,” *Chem. Soc. Rev.,* vol. 40, no. 7, pp. 4186-4216, 2011.

113. S. Ding, R. E. Blue, D. R. Morgan, and P. K. Lund, “Comparison of multiple enzyme activatable near infrared fluorescent molecular probes for detection and quantification of inflammation in murine colitis models,” *Inflamm. Bowel Dis.,* vol. 20, no. 2, pp. 363, 2014.

114. H.-J. Yang, Y. Kong, Y. Cheng, H. Janagama, H. Hassounah, H. Xie, J. Rao, and J. D. Cirillo, “Real-time Imaging of Mycobacterium tuberculosis, Using a Novel Near-Infrared Fluorescent Substrate,” *J. Infect. Dis.,* vol. 215, no. 3, pp. 405-414, 2017.

115. K. Gu, Y. Xu, H. Li, Z. Guo, S. Zhu, S. Zhu, P. Shi, T. D. James, H. Tian, and W.-H. Zhu, “Real-time tracking and in vivo visualization of β-galactosidase activity in colorectal tumor with a ratiometric near-infrared fluorescent probe,” *J. Am. Chem. Soc,* vol. 138, no. 16, pp. 5334-5340, 2016.

116. Y.-P. Kim, W. L. Daniel, Z. Xia, H. Xie, C. A. Mirkin, and J. Rao, “Bioluminescent nanosensors for protease detection based upon gold nanoparticle–luciferase conjugates,” *Chem. Commun.,* vol. 46, no. 1, pp. 76-78, 2010.

117. T. Zeng, T. Zhang, W. Wei, Z. Li, D. Wu, L. Wang, J. Guo, X. He, and N. Ma, “Compact, programmable, and stable biofunctionalized upconversion nanoparticles prepared through peptide-mediated phase transfer for high-sensitive protease sensing and in vivo apoptosis imaging,” *ACS Appl. Mater. Interfaces,* vol. 7, no. 22, pp. 11849-11856, 2015.

118. J. Gallo, N. Kamaly, I. Lavdas, E. Stevens, Q. D. Nguyen, M. Wylezinska-Arridge, E. O. Aboagye, and N. J. Long, "CXCR4-Targeted and MMP-Responsive Iron Oxide Nanoparticles for Enhanced Magnetic Resonance Imaging," *Angewandte Chemie International Edition,* vol. 53, no. 36, pp. 9550-9554, 2014.
119. C. Ansari, G. A. Tikhomirov, S. H. Hong, R. A. Falconer, P. M. Loadman, J. H. Gill, R. Castaneda, F. K. Hazard, L. Tong, and O. D. Lenkov, "Development of Novel Tumor-Targeted Theranostic Nanoparticles Activated by Membrane-Type Matrix Metalloproteinases for Combined Cancer Magnetic Resonance Imaging and Therapy," *Small,* vol. 10, no. 3, pp. 566-575, 2014.
120. Y. Yuan, S. Ge, H. Sun, X. Dong, H. Zhao, L. An, J. Zhang, J. Wang, B. Hu, and G. Liang, "Intracellular self-assembly and disassembly of 19F nanoparticles confer respective "Off" and "On" 19F NMR/MRI signals for Legumain activity detection in zebrafish," *ACS Nano,* vol. 9, no. 5, pp. 5117-5124, 2015.
121. C.-H. Chuang, K.-H. Chuang, H.-E. Wang, S. R. Roffler, J.-t. Shiea, S.-C. Tzou, T.-C. Cheng, C.-H. Kao, S.-Y. Wu, and W.-L. Tseng, "In vivo positron emission tomography imaging of protease activity by generation of a hydrophobic product from a noninhibitory protease substrate," *Clin. Cancer Res.,* vol. 18, no. 1, pp. 238-247, 2012.
122. N. Kondo, T. Temma, J. Deguchi, K. Sano, M. Ono, and H. Saji, "Development of PEGylated peptide probes conjugated with 18 F-labeled BODIPY for PET/optical imaging of MT1-MMP activity," *J. Control. Release,* vol. 220, pp. 476-483, 2015.
123. S. M. van Duijnhoven, M. S. Robillard, S. Hermann, M. T. Kuhlmann, M. Schäfers, K. Nicola√, and H. Grüll, "Imaging of MMP activit√ in postischemic

cardiac remodeling using radiolabeled MMP-2/9 activatable peptide probes," *Mol. Pharm.,* vol. 11, no. 5, pp. 1415-1423, 2014.

124. L. V. Wang, and S. Hu, "Photoacoustic tomography: in vivo imaging from organelles to organs," *Science,* vol. 335, no. 6075, pp. 1458-1462, 2012.

125. A. Taruttis, and V. Ntziachristos, "Advances in real-time multispectral optoacoustic imaging and its applications," *Nat. Photonics,* vol. 9, no. 4, pp. 219-227, 2015.

126. L. Nie, and X. Chen, "Structural and functional photoacoustic molecular tomography aided by emerging contrast agents," *Chem. Soc. Rev.,* vol. 43, no. 20, pp. 7132-7170, 2014.

127. W. Li, P. K. Brown, L. V. Wang, and Y. Xia, "Gold nanocages as contrast agents for photoacoustic imaging," *Contrast Media Mol. Imaging,* vol. 6, no. 5, pp. 370-377, 2011.

128. X. Yang, S. E. Skrabalak, Z.-Y. Li, Y. Xia, and L. V. Wang, "Photoacoustic tomography of a rat cerebral cortex in vivo with au nanocages as an optical contrast agent," *Nano Lett.,* vol. 7, no. 12, pp. 3798-3802, 2007.

129. K. H. Song, C. Kim, C. M. Cobley, Y. Xia, and L. V. Wang, "Near-infrared gold nanocages as a new class of tracers for photoacoustic sentinel lymph node mapping on a rat model," *Nano Lett.,* vol. 9, no. 1, pp. 183-188, 2008.

130. C. Kim, E. C. Cho, J. Chen, K. H. Song, L. Au, C. Favazza, Q. Zhang, C. M. Cobley, F. Gao, and Y. Xia, "In vivo molecular photoacoustic tomography of melanomas targeted by bioconjugated gold nanocages," *ACS Nano,* vol. 4, no. 8, pp. 4559-4564, 2010.

131.R. Roy, J. Yang, and M. A. Moses, “Matrix metalloproteinases as novel biomarker s and potential therapeutic targets in human cancer,” *J. Clin. Oncol.,* vol. 27, no. 31, pp. 5287-5297, 2009.

132.M. Yu, and J. Zheng, “Clearance pathways and tumor targeting of imaging nanoparticles,” *ACS Nano,* vol. 9, no. 7, pp. 6655-6674, 2015.

133.E. Herzog, A. Taruttis, N. Beziere, A. A. Lutich, D. Razansky, and V. Ntziachristos, “Optical imaging of cancer heterogeneity with multispectral optoacoustic tomography,” *Radiology,* vol. 263, no. 2, pp. 461-468, 2012.

134.E. C. Cho, C. Kim, F. Zhou, C. M. Cobley, K. H. Song, J. Chen, Z.-Y. Li, L. V. Wang, and Y. Xia, “Measuring the optical absorption cross sections of Au− Ag nanocages and au nanorods by photoacoustic imaging,” *J. Phys. Chem. C,* vol. 113, no. 21, pp. 9023-9028, 2009.

135.G. Taraboletti, S. D'Ascenzo, P. Borsotti, R. Giavazzi, A. Pavan, and V. Dolo, “Shedding of the matrix metalloproteinases MMP-2, MMP-9, and MT1-MMP as membrane vesicle-associated components by endothelial cells,” *Am. J. Pathol.,* vol. 160, no. 2, pp. 673-680, 2002.

136.A. Taruttis, and V. Ntziachristos, “Advances in real-time multispectral optoacoustic imaging and its applications,” *Nat. Photonics,* vol. 9, no. 4, pp. 219-227, 2015.

137.X. Xia, M. Yang, L. K. Oetjen, Y. Zhang, Q. Li, J. Chen, and Y. Xia, “An enzyme-sensitive probe for photoacoustic imaging and fluorescence detection of protease activity,” *Nanoscale,* vol. 3, no. 3, pp. 950-953, 2011.

138.Y. Chau, R. F. Padera, N. M. Dang, and R. Langer, “Antitumor efficacy of a novel polymer–peptide–drug conjugate in human tumor xenograft models,” *Int. J. Cancer,* vol. 118, no. 6, pp. 1519-1526, 2006.

139. J. Levi, S.-R. Kothapalli, S. Bohndiek, J.-K. Yoon, A. Dragulescu-Andrasi, C. Nielsen, A. Tisma, S. Bodapati, G. Gowrishankar, and X. Yan, “Molecular photoacoustic imaging of follicular thyroid carcinoma,” *Clin. Cancer Res.,* vol. 19, no. 6, pp. 1494-1502, 2013.
140. A. Dragulescu-Andrasi, S.-R. Kothapalli, G. A. Tikhomirov, J. Rao, and S. S. Gambhir, “Activatable oligomerizable imaging agents for photoacoustic imaging of furin-like activity in living subjects,” *J. Am. Chem. Soc.,* vol. 135, no. 30, pp. 11015-11022, 2013.
141. K. E. Wilson, T. Y. Wang, and J. K. Willmann, “Acoustic and photoacoustic molecular imaging of cancer,” *J. Nucl. Med.,* vol. 54, no. 11, pp. 1851-1854, 2013.